

**Allee Effects in Cancer Stem Cell Driven Solid Tumors**

by

Alexandra Shyntar

A thesis submitted in partial fulfillment of the requirements for the degree of

Master of Science

in

Applied Mathematics

Department of Mathematical and Statistical Sciences

University of Alberta

© Alexandra Shyntar, 2023

# Abstract

In this thesis, we perform a systematic study of the Allee effect in cancer stem cell (CSC) models with an application to non-small cell lung cancer (NSCLC). Previously, it was shown that an Allee effect exists in mathematical tumor growth models incorporating cancer stem cell (CSC) dynamics. Here, we extend CSC models to study the Allee effect further. Through the analysis of the models using geometric singular perturbation theory, as well as linear stability analysis, we show the existence of the Allee region, which captures the densities at which natural tumor remission occurs. We find that the Allee region can be enlarged by several mechanisms, such as increasing the death rates of the cancer cells. However, decreasing the self-renewal capabilities of CSCs is much more effective at enlarging the region. This signifies that targeted therapy along with conventional cytotoxic therapies can be more effective at treating the tumor rather than conventional therapy alone. Finally, we reduce the CSC model and fit it to the gross tumor volume data of NSCLC patients, by using Latin Hypercube Sampling to sample a parameter space. The data is obtained from patients who received intensity-modulated radiotherapy alongside chemotherapy. We find that the Allee effect and the distinction between the heterogeneous cell types in the tumor are not needed to explain the data. Although the patients have varying responses to treatment and varying parameters, we nevertheless find a ratio that may indicate how well patients will respond to the treatment.

# Preface

In this thesis, I continue the study of how tumor growth dynamics can be explained using mathematical modelling. The work presented here is interdisciplinary, where I draw from mathematics, biological sciences, as well as medical sciences to propose plausible mathematical models for cancer growth.

Cancer stem cells (CSCs) have been identified to being able to repopulate the tumor post treatment [4, 43]. As CSCs have the ability to self-renew and are generally resistant to treatment, CSCs are the leading cause of treatment failure [17, 37, 60, 69]. The tumor also has other cell types, which lack stemness and are unable to sustain the tumor [1, 68]. These cells will be referred to as tumor cells (TCs) for simplicity. In rare occasions after diagnosis, a tumor can spontaneously decay without a clear cause [39]. This phenomenon is called spontaneous tumor remission, and a possible explanation as to why it occurs is the Allee effect [39]. The Allee effect typically arises in ecology, and is observed when a species requires a substantial population to survive within an environment, as cooperation is necessary [13]. Here, I show when an Allee effect is present in tumors, by modelling tumor growth mathematically and accounting for CSC and TC dynamics as well as feedback mechanisms. The presence of the Allee effect can give rise to an Allee region, which captures the tumor densities that experience spontaneous decay. By building onto our understanding of why an Allee effect can occur in a tumor, further insight on spontaneous tumor remission could be gained, which may lead to innovative and more effective treatments for cancer. Further, I propose a simple mathematical model to explain the gross tumor volume from the non-small cell lung cancer (NSCLC) data. I observe that accounting for an Allee effect or having a distinction between CSCs and TCs is not necessary to explain the data. However, including a damaged compartment is necessary to accurately model the long term tumor volume. The model fits to patient data well, and there is significant variability in the resulting model parameters between patients. I find a criterion based on model

parameters that may indicate patient outcomes. By gaining the ability to accurately model tumor growth, patient treatment response can be predicted, leading to optimized treatments and improved patient outcomes.

This thesis is related to a book chapter I co-authored with Dr. Thomas Hillen called “Modelling of cancer stem cell driven solid tumors” published in *Problems in Mathematical Biophysics* — a volume in memory of Alberto Gandolfi [32]. This book chapter contains a review of existing research focused on modelling tumor growth with cancer stem cell dynamics. None of the results contained in this thesis have been included in that publication.

This thesis also references a paper I published with Dr. Thomas Hillen and others in the *Bulletin of Mathematical Biology* called “The tumor invasion paradox in cancer stem cell-driven solid tumors” [62]. The paper is referenced to provide the background of what was previously done with a cancer stem cell model incorporating spatial dynamics. None of the content in this thesis was published in that paper.

The patient data for gross tumor volume of non-small cell cancer (NSCLC) used here was provided by the Center for Radiation Research in Oncology in Dresden, Germany. The data was pseudonymized and has received the ethics approval number BO-EK-86022022, which was granted by the Ethics Committee of the Technische Universität Dresden, Germany.

Alexandra Shyntar  
Edmonton, June 2023

## Acknowledgments

I would like to thank Dr. Thomas Hillen for being my supervisor and guiding me through the Master's program. I would also like to thank Dr. Jay Newby, Dr. Gerda de Vries, and Dr. John Bowman for being part of my defense committee. In addition, I thank Dr. Yalcin Kuzay and Dr. Esther Troost for providing the NSCLC data as well as Dr. Andreas Deutsch and Dr. Haralampos Hatzikirou for helpful discussions. I am grateful for the funding and scholarships that I have received, specifically the Canada Graduate Scholarship – Master's (CGS-M - NSERC), Walter H John's Graduate Fellowship, and Dr. Josephine M. Mitchell Recruitment Scholarship from the University of Alberta.

# Contents

<b>1</b>	<b>Introduction</b>	<b>1</b>
1.1	Cancer Stem Cell Models . . . . .	2
1.2	Allee Effects in Cancer Models . . . . .	5
1.3	Lung Cancer and Treatments . . . . .	6
1.4	Previous Modelling Incorporating Cancer Stem Cell Dynamics . . . . .	7
1.4.1	Existence of the Tumor Growth Paradox . . . . .	7
1.4.2	Existence of the Tumor Invasion Paradox . . . . .	9
1.4.3	Inclusion of Feedback Mechanisms . . . . .	10
1.4.4	Other Results from Modelling Cancer Stem Cells . . . . .	13
1.5	Geometric Singular Perturbation Theory . . . . .	14
1.5.1	Example 1 . . . . .	17
1.5.2	Example 2: Tumor Growth Paradox . . . . .	20
1.6	Outline . . . . .	22
<b>2</b>	<b>Cancer Stem Cell Model with an Allee Effect</b>	<b>24</b>
2.1	Fast System . . . . .	26
2.2	Slow System . . . . .	35
2.2.1	Dynamics on Branch I . . . . .	36
2.2.2	Dynamics on Branch III . . . . .	40
2.2.3	Dynamics on Branch II . . . . .	42
2.2.4	Summary of Dynamics on $M$ . . . . .	43

2.2.5	Behaviour at Non Hyperbolic Points . . . . .	46
2.3	Allee Region . . . . .	47
<b>3</b>	<b>Biologically Relevant Cancer Stem Cell Model with an Allee Effect</b>	<b>50</b>
3.1	Fast System . . . . .	53
3.2	Slow System . . . . .	56
3.2.1	Remarks . . . . .	57
3.3	Cancer Stem Cell Model with Allee Effect and Treatment . . . . .	58
3.3.1	Fractionated Treatment . . . . .	61
<b>4</b>	<b>Feedback Mechanisms and the Allee Effect</b>	<b>64</b>
4.1	Introduction . . . . .	64
4.2	Cancer Stem Cell Model Incorporating Feedback Mechanisms . . . . .	65
4.3	Linear Stability Analysis . . . . .	67
4.4	Existence of an Allee Region . . . . .	70
4.5	Numerical Examples . . . . .	72
<b>5</b>	<b>Model Fitting to Lung Cancer Data</b>	<b>79</b>
5.1	Modelling of Non-Small Cell Lung Cancer . . . . .	79
5.2	Patient Data . . . . .	80
5.3	Model Derivation . . . . .	81
5.4	Model Fitting . . . . .	85
5.5	Results . . . . .	89
5.6	Conclusion . . . . .	99
<b>6</b>	<b>Discussion</b>	<b>102</b>

# List of Tables

5.1	Table of AICc values . . . . .	96
5.2	Table of $R^2$ values . . . . .	97
5.3	Table of $\rho$ ratios . . . . .	99

# List of Figures

1.1	Illustration of three possible CSC models. . . . .	3
1.2	Illustration of strong and weak effects . . . . .	6
1.3	Phase portraits for example (1.13) . . . . .	18
1.4	Illustration of the Tumor Growth Paradox . . . . .	21
2.1	Phase portraits of (2.2) . . . . .	33
2.2	Example manifolds . . . . .	37
2.3	Phase portraits of (2.1) under strong Allee effect with three branch $M$ . . . . .	44
2.4	Phase portraits of (2.1) under weak Allee effect with three branch $M$ . . . . .	44
2.5	Phase portraits of (2.1) under strong Allee effect, other cases of $M$ . . . . .	45
2.6	Phase portraits of (2.1) under weak Allee effect, other cases of $M$ . . . . .	45
2.7	Illustration of what occurs at the non hyperbolic points . . . . .	47
2.8	Illustration of an Allee region . . . . .	48
3.1	Phase portraits of (3.11) . . . . .	56
3.2	Phase space simulations of (3.20) . . . . .	60
3.3	Examples of fractionated treatments . . . . .	63
4.1	Illustration of the cases in Theorem 4.4.2 . . . . .	71
4.2	Probability functions $p(n)$ . . . . .	72
4.3	Phase portraits of system (4.4) . . . . .	74
4.4	Summary of parameter trends . . . . .	76
5.1	Illustration of the Latin Hypercube Sampling method . . . . .	86

5.2	Model 1 (5.8) fits for intensity-modulated radiotherapy treatment type I	90
5.3	Model 2 (5.9) fits for intensity-modulated radiotherapy treatment type I.	91
5.4	Model 1 (5.8) fits for intensity-modulated radiotherapy treatment type II.	92
5.5	Model 2 (5.9) fits for intensity-modulated radiotherapy treatment type II.	93
5.6	Poor fits from Model 1 (5.8) . . . . .	94
5.7	Poor fits from Model 2 (5.9) . . . . .	94
5.8	Box plots of the parameter ranges obtained from the data fits . . . . .	98

# Chapter 1

## Introduction

Cancer is a broad name given to related types of diseases, many without cure to this day [36, 59]. These diseases arise from uncontrollable cell division, often resulting in a tumor [27, 67]. Such a tumor is heterogeneous, consisting of different cell types, which can grow large and/or spread to other areas of the body [67, 72]. To get an idea as to how complicated cancer is, Hanahan and Weinberg published *The Hallmarks of Cancer* [28] and later *Hallmarks of Cancer: The Next Generation* [29] and *Hallmarks of Cancer: new dimensions* [27] outlining in total 14 key differences between regular and cancerous tissues. Some of these differences include the unlimited ability to replicate, resistance to cell death, avoidance of growth suppressors, the ability to invade nearby and distant tissues, and avoidance of being destroyed by the immune system. It has been shown that cancer stem cells (CSCs) are key players responsible for the different behaviour in cancerous tissue in comparison to regular tissue [17, 32]. This means that CSCs are involved in many of the hallmarks. Another aspect of cancer that is poorly understood is spontaneous remission [54]. This is a rare phenomenon where a tumor decays naturally, with an unknown cause [54, 39]. In many cases, spontaneous remission has been reported to occur after an acute infection [54]. As the immune system activates to combat the infection, it can also target a tumor [54]. A potential explanation of spontaneous remission is the presence of an Allee effect [39]. Here, we

will propose mathematical models incorporating CSC dynamics applicable to general solid tumors and study the tumor dynamics when an Allee effect is present.

## 1.1 Cancer Stem Cell Models

Cancer stem cells (CSCs) were first discovered in leukemia (a type of blood cancer) and later in other cancers [4, 43]. These cells were shown to have the ability to reinitiate the cancer if isolated [4, 43]. Now, CSCs are generally characterized as having unlimited ability to replicate, prolonged life span, and having resistance to cancer treatments [17, 37, 60]. An early paper titled *Successful therapy must eradicate cancer stem cells* [16], outlined through mathematical modelling the role of CSCs in cancer recurrence. In particular, they showed that in order to have a successful treatment, all CSCs must be eliminated. As tumors have different cell types, such as transient amplifying cells and differentiated cells, in addition to CSCs [68], we refer to the cells lacking stemness as tumor cells (TCs), as is typically done when modelling tumor dynamics [19, 31]. TCs have a shorter lifespan than CSCs and are also more common than CSCs in a tumor [68, 72].

Due to the significance of CSCs in cancer, mathematical models incorporating the CSC dynamics have been proposed [31, 38]. Due to varying assumptions on how CSCs divide, three main models arose in literature [32]. A schematic of them is shown in Figure 1.1. Here, we outline the mathematical models arising from each diagram and show that they are mathematically equivalent. We do this because the models we examine later build upon these base models.

The Complete model in Figure 1.1 (left) takes into account all possible offspring that a CSC can yield. A CSC can divide symmetrically into two CSCs. We denote the fraction of symmetric CSC divisions by  $a_1$ . A CSC can also divide asymmetrically to yield a CSC and a tumor cell (TC) where  $a_2$  is the fraction of asymmetric divisions. Finally, a CSC can divide to yield two TCs (which we call a symmetric commitment event) and  $a_3$  represents the fraction of symmetric commitment events. Further,  $a_1 +$

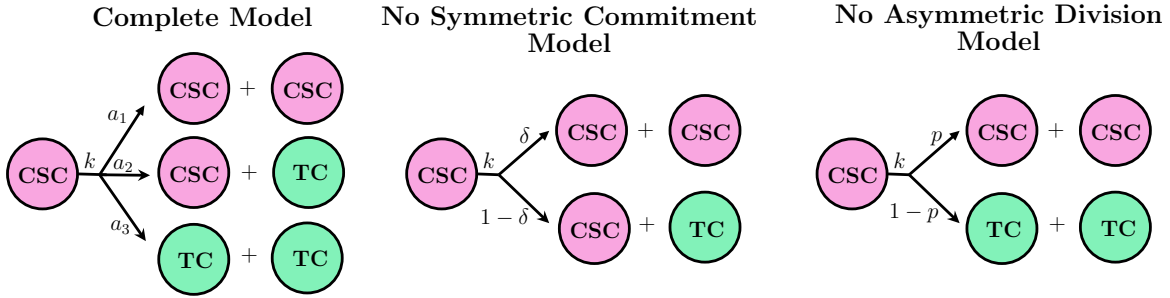


Figure 1.1: Illustration of three possible CSC models. In each model,  $k$  represents the mitosis rate. In the Complete Model,  $a_1$  is the fraction of symmetric divisions into two CSCs,  $a_2$  is the fraction of asymmetric divisions, and  $a_3$  is the fraction of symmetric commitment events. The parameter  $\delta$  in the No Symmetric Commitment Model is the fraction of pure CSC offspring and the parameter  $p$  in the No Asymmetric Division Model is the probability of obtaining pure CSC offspring.

$a_2 + a_3 = 1$  since these fractions can also be interpreted as probabilities, and the total probability of different outcomes is one. A mathematical model can be derived from the first diagram in Figure 1.1, by writing the down the changes in the CSC and TC populations. Note that if the fraction value is multiplied by  $k$ , the mitosis rate, then the product will yield the rate of a particular division. If we let  $u(t)$  represent the CSC population and  $v(t)$  represent the TC population, we obtain

$$\begin{aligned} \dot{u} &= ka_1u - ka_3u, \\ \dot{v} &= ka_2u + 2ka_3u, \end{aligned} \tag{1.1}$$

where  $ka_1$  is the rate of symmetric division into two CSCs,  $ka_2$  is the asymmetric division rate, and  $ka_3$  is the symmetric commitment rate. The first term of the first equation in (1.1) is obtained by noting that the net gain from symmetric division into two CSCs is one CSC cell, since one CSC replaces the mother cell. In symmetric commitment events one CSC is used up since no CSCs are produced, which gives the second term in the first equation. One TC is produced from asymmetric division giving the first term of the second equation. Note that in asymmetric division the net change in CSC is zero since one CSC replaces the mother cell. Finally, the second term in the second equation is obtained by noting that two TCs are produced in a symmetric

commitment event. Model (1.1) can be rewritten in terms of two parameters by using the relationship  $a_1 + a_2 + a_3 = 1$  to eliminate  $a_1$ , yielding

$$\begin{aligned}\dot{u} &= k(1 - a_2 - 2a_3)u, \\ \dot{v} &= k(a_2 + 2a_3)u.\end{aligned}\tag{1.2}$$

By following the same derivation that was used for the complete model, we can write down the mathematical model for the No Symmetric Commitment Model in Figure 1.1 (middle) as follows

$$\begin{aligned}\dot{u} &= \delta ku, \\ \dot{v} &= (1 - \delta)ku,\end{aligned}\tag{1.3}$$

where  $\delta$  is the fraction of pure CSC offspring (assuming  $\delta > 0$ ), and  $\delta k$  defines the rate of symmetric division into two CSCs and  $(1 - \delta)k$  is the rate of asymmetric division. Model (1.3) was used in [31] since their underlying assumption was that CSCs self-renew during cell division. In general,  $\delta$  can be negative which means that CSCs prioritize creating differentiated cells (TCs) rather than self-renewal. Hence, the CSC population declines in that case.

We can also derive the No Asymmetric Division Model from Figure 1.1 (right) which is given by

$$\begin{aligned}\dot{u} &= 2pku - ku, \\ \dot{v} &= 2(1 - p)ku,\end{aligned}\tag{1.4}$$

where  $p$  is the self-renewal probability. Two CSCs are produced with rate  $pk$  when symmetric division occurs giving the first term in the first equation of (1.4). Since a mother CSC is lost during a mitosis event, this gives the second term in the first equation. The term in the second equation of (1.4) is obtained by noting that two TCs are produced with probability  $1 - p$ . Model (1.4) is used when asymmetric division is neglected. Some examples of when model (1.4) was used can be found in [45, 21, 38, 70].

We now show that the three models outlined above are mathematically equivalent.

**Lemma 1.1.1.** *The dynamics of models (1.2), (1.3), (1.4) are equivalent.*

*Proof.* If  $\delta = 2p - 1$ , then (1.3) gives (1.4) and if  $p = (\delta + 1)/2$ , (1.4) gives (1.3). Hence, (1.3) and (1.4) are equivalent. If  $a_2$  and  $a_3$  are known then setting

$$\delta = 1 - a_2 - 2a_3 \tag{1.5}$$

in model (1.3) yields model (1.2). If  $\delta$  is known, then by using the relationship in (1.5) we can recover model (1.2) and there are infinitely many ways to choose  $a_2$  and  $a_3$  to satisfy (1.5). So models (1.2) and (1.3) have equivalent dynamics.  $\square$

## 1.2 Allee Effects in Cancer Models

An Allee effect is a phenomenon that arises when a small population fails to establish itself in an environment whereas a larger population can establish itself [13]. Sometimes organisms need to cooperate to survive a harsh environment. When there are few organisms, the drawback from a lack of cooperation can outweigh the benefits of nutrients and space that a smaller population would have, and thus the small population fails to sustain itself in an environment [13]. Following this idea from ecology, an Allee effect is hypothesized to also be present in tumors [39]. Further, an Allee effect was shown to exist in a CSC model incorporating feedback mechanisms from self-renewal activators and differentiation promoters in [38].

In our modelling, we will first consider two possibilities for an Allee effect: a strong Allee effect and a weak Allee effect [13]. The strong Allee effect occurs when there exists some Allee threshold, which dictates when a population is unable to establish itself in an environment. The Allee effect can be typically modelled by the following ODE

$$\dot{N} = N(1 - N)(N - A) \tag{1.6}$$

where  $N$  is the density of organisms and  $0 < A < 1$  is the Allee threshold [13]. We see that (1.6) has 3 equilibria, where  $N_1^* = 0$  and  $N_2^* = 1$  are stable whereas  $N_3^* = A$  is unstable. These dynamics show that if the population density starts off below  $A$

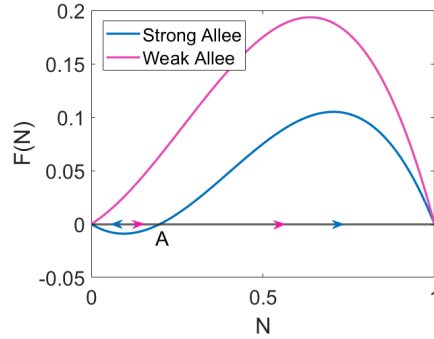


Figure 1.2: Illustration of strong and weak effects where  $F(N)$  is given by the right hand side of (1.6). For the strong Allee effect  $A = 0.2$ , and for weak Allee effect  $A = -0.2$ . Here we see the dynamics of the strong Allee effect where the blue arrows show the flow of the trajectories. For the weak Allee, the trajectories flow to the right converging to 1 and the population cannot die out.

the population dies out, whereas the population density starting above  $A$  grows to the carrying capacity of 1, as shown in Figure 1.2.

A weak Allee effect on the other hand is characterized by slower density growth of small populations and no Allee threshold, meaning that the organisms cannot die out [13]. This can be modelled by setting  $A \leq 0$  in (1.6), which yields that  $N_1^* = 0$  is unstable and  $N_2^* = 0$  is stable. The other equilibrium, if present, is biologically irrelevant. An example of the weak Allee effect is shown in Figure 1.2.

In Chapters 2 and 3, we study the implications of strong and weak Allee effects on tumor growth dynamics. In Chapter 4, we use a different approach to study the Allee effect, by incorporating feedback mechanisms like was done in [38].

### 1.3 Lung Cancer and Treatments

After studying the Allee effects in cancer stem cell models in general, we study whether an Allee based model is appropriate to explain a set of gross tumor volume data in lung cancer. About 85% of lung cancer cases are categorized as non-small cell lung cancer (NSCLC), which is a heterogeneous disease with low survival rate [8]. Due to the low survival rate, extensive research has been performed as to which treatments

give a longer survival time [8, 51]. In the early stages of NSCLC, it is possible to surgically remove the tumor [8], however this is not an option in the later stages. Typical non surgical treatments include chemotherapy, which involves giving a patient a specified dose of anti cancer drugs, and intensity-modulated radiotherapy, which involves giving a specified radiation dose to the patient [23]. Here, we refer to chemotherapy and radiotherapy treatments as cytotoxic, as they are focused on killing cancer cells. After a cytotoxic treatment, it takes times to see shrinkage in the treated tumor, which is referred to as the latency time effect [49, 66]. It has been concluded that concurrent chemoradiotherapy treatments are superior at prolonging the survival period in comparison to treatments comprising of solely chemotherapy or radiotherapy and even sequential chemoradiotherapy treatments [23, 51].

In Chapter 5, we will derive a model for the gross tumor volume of NSCLC. The data that we work with is from a study conducted in 2021 by OncoRay - National Center for Radiation Research in Oncology in Dresden, Germany where the effect intensity-modulated radiotherapy treatments on non-small cell lung cancer (NSCLC). Our model will account for radiotherapy and chemotherapy treatments. We find that our simple model is able to explain the data well, where accounting for the Allee effect is not necessary.

## 1.4 Previous Modelling Incorporating Cancer Stem Cell Dynamics

### 1.4.1 Existence of the Tumor Growth Paradox

CSCs have been linked to a number of surprising phenomena in a tumor. One such process is the so called *tumor growth paradox*. The tumor growth paradox is a phenomenon when a tumor with a higher cell death rate grows larger than a tumor with a lower death rate [31]. Enderling et al. [19] tested an agent based model that simulated CSCs and TCs on a lattice grid. The biological assumptions of their model are that

CSCs are immortal, TCs can spontaneously die, and that CSCs and TCs compete for space. From their simulations, it was found that with an increased cell death rate, the tumor initially decreases but then grows back faster than it would have without the increased death rate. The accelerated growth occurs because as TCs die, the CSCs become liberated and can proliferate within the available space. The tumor then gets repopulated and grows faster, illustrating the tumor growth paradox (see section 1.5.2 for more details). This liberation of CSCs serves as an explanation as to why there can be tumor relapse post treatment.

Following the work of Enderling et al. [19], Hillen et al. [31] propose a mathematical model with the same biological assumptions, in order to prove the tumor growth paradox mathematically. Here, we outline the derivation of the Hillen et al. [31] model and outline how to prove the tumor growth paradox in Section 1.5.2. The specific assumptions of the Hillen et al. [31] model are the following

- A1. TCs can only produce TCs and have a proliferation limit.
- A2. TCs are mortal hence have a positive death rate given by  $a$ .
- A3. CSCs are immortal on the observed timescale.
- A4. CSCs and TCs compete for space, and if there is no space available there is no growth.

To derive the Hillen et al. [31] model we start with the no symmetric commitment model (1.3) and add the outlined assumptions above. Mathematically accounting for assumptions A1 and A2 is straightforward, where A1 requires a term that counts the contributions from TCs to the TC population and A2 requires a death term, both of which need to be added to (1.3). In order to incorporate assumption A4 a competition function  $F(n)$  where  $n = u + v$  is introduced with the following assumptions:

- F1.  $F(n)$  is Lipschitz continuous, where  $F(0) = 1$  and for  $n \geq K$ ,  $F(n) = 0$  where  $K$  is some maximum density that  $n$  can reach.

F2.  $F(n)$  is nonincreasing: if  $n_1 < n_2$  then  $F(n_1) \geq F(n_2)$

Essentially, the competition function limits growth due to space limitations. Another interpretation of  $F(n)$  is that it models a negative feedback. As space becomes limited, cancer cells release proliferation inhibitors slowing down tumor growths. It follows that  $F(n)$  is incorporated into the model by having it multiply the growth rates. With these modifications, model (1.3) becomes

$$\begin{aligned} \dot{u} &= \delta k F(n) u, \\ \dot{v} &= (1 - \delta) k F(n) u + k_2 F(n) v - av, \end{aligned} \tag{1.7}$$

where the second term in the second equation accounts for the net contribution of TCs to the TC population, with  $k_2$  being the mitosis rate of TCs, and the last term of the second equation being the death term with death rate  $a$ . Notice that (1.7) satisfies assumption A3 since there is no CSC death. For simplicity, the densities are normalized so that  $K = 1$  and the mitosis rates  $k$  and  $k_2$  are set to 1. These simplifications do not affect the generality of the results. To analyze (1.7), geometric singular perturbation theory is required [30, 31], which we outline in Section 1.5 and make use of in Section 1.5.2 to show the tumor growth paradox.

### 1.4.2 Existence of the Tumor Invasion Paradox

The Hillen et al. [31] model (1.7) derived above is actually a reduced version of the full birth-jump model also proposed in [31]. In a birth-jump process, population spread and growth are interdependent, unlike in reaction-diffusion models where spread and growth are assumed to be independent [32]. The birth-jump model in [31] arose by mathematically formulating the search for space by a daughter cell from the computational model of Enderling et al. [19]. It has been shown that the birth-jump model proposed in [15] has a unique global solution [44], and that the spatially homogeneous version of the model also has a unique global solution [5].

What makes the birth-jump model in [31] difficult to analyze is the integral operator.

This integral operator has been expanded where the leading order terms are kept, yielding a reaction-diffusion model. The resulting reaction-diffusion models have been analyzed [20, 62]. In [62], the resulting reaction-diffusion model is simply an extension of (1.7) with respective diffusion terms for CSCs and TCs. By using geometric singular perturbation theory and travelling wave analysis, we prove in Shyntar et al. [62] that a *tumor invasion paradox* exists. The tumor invasion paradox is a phenomenon when a tumor with a higher death rate spreads more than a tumor with a lower death rate [62]. The existence of the tumor invasion paradox has been verified numerically and through an agent based model proposed by Enderling et al. [19] in [62]. The main implication is that during a long term cytotoxic treatment, the elevated death rate can liberate CSCs, and cause the tumor to spread faster [62]. We found in Shyntar et al. [62] that invasion paradox is not as significant in fractionated treatments that have a short treatment time.

### 1.4.3 Inclusion of Feedback Mechanisms

Models incorporating feedback mechanisms and CSC dynamics have been proposed to model tumor growth and spread. Youssefpour et al. [70] proposed a mathematical model applicable to solid avascular tumors, which incorporates CSC and TC, as well as transient amplifying cells. Transient amplifying cells are cells that have not fully differentiated. The Youssefpour et al. [70] model also accounts for spatial dependence, mechanical forces, nutrient and oxygen uptake, growth promoter and inhibitor factors, as well as signalling factors produced by the cancer cells, which stimulate various feedback mechanisms. Specifically, they incorporated a positive feedback mechanism from self-renewal activators that stimulate the self renewal of CSCs and the negative feedback mechanism caused by differentiation promoters which cause CSCs to differentiate. We note that the spatially homogeneous version of the Youssefpour et al. [70] model is a more involved version of the No Asymmetric Division Model (1.4). To incorporate the feedback mechanisms they propose an explicit probability function for  $p$  in

(1.4). Recall that  $p$  is the probability of symmetric divisions into two CSCs. The proposed function for  $p$  incorporates self-renewal activator and differentiation promoter concentrations. To analyze their model, Youssefpour et al. [70] performed 2D and 3D simulations. They find that CSCs tend to be spread uniformly in a tumor and that more invasive tumors tend to form finger-like structures where CSCs tend to self renew more at the boundary of the tumor. Further, if CSCs are not sensitive to negative feedback from the differentiation promoters, the tumor grows quickly, forming invasive finger-like structures. As sensitivity increases to the differentiation promoters, the tumor retains its sphere-like shape and grows slower in general and the concentration of differentiation promoters within a given cluster was found to be uniform. Youssefpour et al. [70] also test two treatments, a cytotoxic treatment like radiotherapy and a targeted therapy treatment, which increases the amount of differentiation promoters. The idea with a targeted therapy treatment is to increase the amount of differentiated cells since differentiated cells tend to be more sensitive to cytotoxic treatments. They find that applying only radiotherapy or only differentiation therapy is insufficient at eliminating the tumor. Radiotherapy also tended to make the tumor more aggressive post treatment, but differentiation therapy does not seem to have an effect on invasiveness. However, a combined treatment which incorporates both radiotherapy and targeted therapy was effective at eradicating the tumor.

Rodriguez-Brenes et al. [58] studied feedback mechanisms by taking the No Asymmetric Division Model (1.4) and extending it to include the negative feedback from only TCs. That is, they assume that as TCs increase, the rate of cell division and the probability of symmetric division into two CSCs decrease. Hence, they incorporate a proliferation feedback and a differentiation feedback from TCs. Rodriguez-Brenes et al. [58] find that the negative feedback on proliferation slows down the growth of the tumor, and if both feedbacks upon proliferation and differentiation are lost, the tumor grows exponentially. Essentially, this shows that the feedback mechanism is required in order to regulate tumor growth, and in order to cause the tumor to decay,  $p$  in (1.4) must become less than 0.5 so that the CSC population begins to die out.

Following the work of Youssefpour et al. [70], Konstorum et al. [38] took the spatially homogeneous model of Youssefpour et al. [70] and examined it mathematically. As mentioned before, the spatially homogeneous model is a more involved version of the No Asymmetric Division Model (1.4) which incorporates feedback mechanisms. They assume that the amount of differentiation promoters is proportional to the amount of CSCs and that the amount of self-renewal inhibitors is assumed to be constant. By analyzing the reduced model mathematically, Konstorum et al. [38] prove that the model can exhibit an Allee region, which is a region capturing the tumor densities that experience spontaneous decay. The Allee region increases as the inhibition of self-renewal promoters increases and decreases as the strength of the self-renewal-activators increases. They find that cytotoxic treatments may increase the Allee region. Moreover, a combination treatment comprised of targeted therapy and a cytotoxic treatment can significantly increase the Allee region, thus significantly improving the chances that the tumor will fully decay post treatment. This shows that full eradication of the tumor during treatment may not be required in order to cause the tumor to fully decay. Rather, it is enough to push it to a size below a certain threshold, and the tumor can decay naturally. Interestingly, the Konstorum et al. [38] model can also explain the two cases of spontaneous tumor remission. The first case is when a tumor decays after an unrelated infection. This is explained in the model by lowering the CSC population (due to an elevated immune response) which helps push the tumor into the Allee region. Further, the Allee region arising in the model has non linear trajectories, showing that if a tumor falls within it, there may be a period of growth before natural decay, explaining the second case of tumor remission where the tumor appeared to decay without any significant change in health or medication. In this thesis, we extend the Konstorum et al. [38] model to incorporate TC dynamics, as well as competition between TCs and CSCs and show that the Allee region may be present as well.

#### 1.4.4 Other Results from Modelling Cancer Stem Cells

Using the Hillen et al. model (1.7), Bachman et al. [1] incorporated feedback mechanisms by following a similar approach as in [70]. To incorporate the feedback mechanisms, they use the fact that the models in Figure 1.1 are mathematically equivalent, in order to derive a version of the Hillen et al. model (1.7) that depends on  $p$  (probability of symmetric division into two CSCs). The function to model  $p$  is the same one used by Youssefpour et al. [70], where Bachman et al. [1] make an additional assumption, which is that the concentration of self-renewal activators is constant. The purpose of their work was to test whether the findings in [70] persist with biologically realistic parameters for head and neck cancer, brain cancer, as well as breast cancer. Like in [70], they focus on a radiotherapy treatment as well as a targeted therapy treatment focused on increasing the amount of differentiation promoters. Therapy effects on growth rates are ignored for simplicity, as was also done in [70]. To assess treatment success, the tumor control probability (TCP) is calculated based on the number of CSCs that remain, as CSCs are able to reinitiate the tumor and a tumor comprised of TCs dies out. Hence, the less CSCs remain the greater the TCP. Bachman et al. [1] were able to confirm the findings of [70], which is that the combined treatment significantly improves TCP for these particular cancers. Further, differentiation therapy can decrease the amount of radiation required in order to achieve an acceptable TCP.

Dedifferentiation of TCs is also possible, where TCs revert to expressing stem like behaviour [63]. A protein called survivin has been linked to promote dedifferentiation, which could lead to radio-resistance in cancer [14]. Iwasa et al. [35] tested the role of a survivin inhibitor YM155 on mice afflicted with NSCLC. In [35], they found that a combined radiotherapy treatment with YM155, is superior to a radiotherapy treatment alone. Rhodes et al. [56] proposed a mathematical model incorporating CSC dynamics to explain the data in [35]. In [56], they propose a mathematical model that builds upon the Hillen et al. [31] model. Their extended model incorporates survivin dynamics by assuming that survivin is released when cells die and that CSCs release more survivin

then TCs. They find that their proposed model fits the mice data from [35] well with and without treatment. Further, they confirm that a combined treatment comprised of both radiotherapy and YM155, is better at delaying the progression of a tumor rather than a treatment of only radiotherapy. Moreover, they find that the optimal radiotherapy regimen depends on the tumor based on its sensitivity to radiation or its density composition. Including survivin dynamics into our proposed models, is outside the scope of this thesis.

## 1.5 Geometric Singular Perturbation Theory

In our analysis of the models, we will employ geometric singular perturbation theory [30]. This theory is especially useful when there is a separation of time scales, that is the rate of change with respect to time of one variable is much lower than the rate of change of another variable. In this section, we outline the theory and apply it two examples. More details can be found in [30].

Our models will naturally have the form

$$\begin{aligned}\dot{x} &= \varepsilon \tilde{f}(x, y, \varepsilon), \\ \dot{y} &= \tilde{g}(x, y, \varepsilon),\end{aligned}\tag{1.8}$$

where we use the dot to indicate  $\frac{d}{dt}$ . System (1.8) is called a fast system, which is typically analyzed by taking  $\varepsilon \rightarrow 0$  and studying the resulting reduced system. A formal perturbation expansion will be shown in the example which yields the same simplification. By taking the limit, we obtain the fast reduced system

$$\begin{aligned}\dot{x} &= 0, \\ \dot{y} &= \tilde{g}(x, y, 0).\end{aligned}\tag{1.9}$$

We see that the flow of the trajectories in (1.9) are simple, where  $x(t)$  is constant.  $y(t)$  can either converge or repel from the nullcline determined from the second equation of

(1.9). Formally, this nullcline is expressed as a manifold

$$M := \{(x, y) : \tilde{g}(x, y, 0) = 0\}. \quad (1.10)$$

Parts of  $M$  can be normally hyperbolic and attracting or normally hyperbolic and repelling.  $M$  is also called the slow manifold, since it contains the long term dynamics of system (1.8).

**Definition 1.5.1.** (*Normally Hyperbolic Manifold*) In (1.8), a slow manifold  $M$  is *normally hyperbolic* if the eigenvalues  $\lambda$  of the Jacobian  $\left. \frac{\partial \tilde{g}}{\partial y}(x, y, 0) \right|_M$  are uniformly bounded away from the imaginary axis, that is  $\text{Re}(\lambda) \neq 0$ .

**Definition 1.5.2.** (*Attracting and Repelling Normally Hyperbolic Manifolds*) In (1.8), if a slow manifold  $M$  is normally hyperbolic, it is also *attracting* if

$$\left. \frac{\partial \tilde{g}}{\partial y}(x, y, 0) \right|_M < 0$$

or *repelling* if

$$\left. \frac{\partial \tilde{g}}{\partial y}(x, y, 0) \right|_M > 0.$$

Notice that Definition 1.5.1 implies that for an arbitrary slow manifold, there are cases when not all eigenvalues of the Jacobian specified in the definition are uniformly bounded away from the imaginary axis. In those cases, we get non hyperbolic points.

**Definition 1.5.3.** (*Non Hyperbolic Points*) In (1.8), the points on the slow manifold  $M$  at which the eigenvalues  $\lambda$  of the Jacobian  $\left. \frac{\partial \tilde{g}}{\partial y}(x, y, 0) \right|_M$  satisfy  $\text{Re}(\lambda) = 0$  are called *non hyperbolic points*.

System (1.9) can be solved to obtain the so called inner solution  $(x(t), y(t))$ , which will be used as a part of the full solution of (1.8). To obtain the rest of the solution, the fast system (1.8) can be rescaled using  $\tau = \varepsilon t$  where  $\tau$  corresponds to time on a slow time scale, and  $t$  corresponds to time on a fast time scale. Using this scaling, we

obtain the slow system

$$\begin{aligned}x' &= \tilde{f}(x, y, \varepsilon), \\ \varepsilon y' &= \tilde{g}(x, y, \varepsilon),\end{aligned}\tag{1.11}$$

where we use  $'$  to indicate  $\frac{d}{d\tau}$ . Notice that (1.11) and (1.9) are fully equivalent when  $\varepsilon \neq 0$ . To analyze (1.11) a perturbation expansion is performed, which is equivalent to taking  $\varepsilon \rightarrow 0$  giving the slow reduced system

$$\begin{aligned}x' &= \tilde{f}(x, y, 0), \\ 0 &= \tilde{g}(x, y, 0).\end{aligned}\tag{1.12}$$

Notice that the last equation of (1.12) is precisely the nullcline used to obtain  $M$ . System (1.12) can be analyzed using stability analysis, since it is a one dimensional ODE were  $y$  can be determined from the second equation. The so called outer solution  $(x(\tau), y(\tau))$  can be obtained by solving (1.12), giving the other part of the full solution. The solutions are then “glued together” using the matching conditions

$$\lim_{t \rightarrow \infty} x(t) = \lim_{\tau \rightarrow 0} x(\tau),$$

$$\lim_{t \rightarrow \infty} y(t) = \lim_{\tau \rightarrow 0} y(\tau).$$

In practice, obtaining explicit inner and outer solutions is difficult. Hence, the focus is on understanding the dynamics of the fast and slow system which can be sufficient in understanding how the full solution behaves. Note that the above was performed for the case when  $\varepsilon = 0$  only, since  $M$  is defined when  $\varepsilon = 0$ . To show that the dynamics from the fast and slow reduced systems persist when  $\varepsilon \neq 0$  and  $\varepsilon$  is small, Fenichel theory is used [30].

**Theorem 1.5.1.** (*Fenichel Theorem 1, Hek [30]*) *Suppose  $M$  is compact and normally hyperbolic. Then for  $\varepsilon > 0$  with  $\varepsilon$  small enough there exists a manifold  $M_\varepsilon$  that is*

1.  $O(\varepsilon)$  close to  $M$ ,

2. diffeomorphic to  $M$ ,

3. locally invariant for the problem (1.8).

**Theorem 1.5.2.** (Fenichel Theorem 2, Hek [30]) Given the assumptions in Theorem 1.5.1, there exist stable and unstable manifolds associated with  $M_\varepsilon$ :  $W^s(M_\varepsilon)$  and  $W^u(M_\varepsilon)$  that are  $\varepsilon$ -close to  $W^s(M)$  and  $W^u(M)$ .

The Fenichel theorems state that  $M$  and its dynamics persist even when  $\varepsilon \neq 0$ , given that  $\varepsilon$  is sufficiently small, since the original problem (1.8) has  $M_\varepsilon$  that is  $O(\varepsilon)$  close to  $M$  and  $M_\varepsilon$  retains all essential characteristics of  $M$ .

### 1.5.1 Example 1

Now we give a concrete example. We choose

$$\begin{aligned}\dot{x} &= \varepsilon x(0.5 - y)(1 - x), \\ \dot{y} &= x - y.\end{aligned}\tag{1.13}$$

To analyze this formally, we perform a perturbation expansion, where

$$x(t) = x_0(t) + \varepsilon x_1(t) + \varepsilon^2 x_2(t) + h.o.t.,$$

$$y(t) = y_0(t) + \varepsilon y_1(t) + \varepsilon^2 y_2(t) + h.o.t.$$

where *h.o.t.* stands for “higher order terms”. Substituting these into (1.13), and keeping the leading order terms which are the ones containing  $\varepsilon^0 = 1$  yields

$$\begin{aligned}\dot{x}_0(t) &= 0, \\ \dot{y}_0(t) &= x_0(t) - y_0(t).\end{aligned}\tag{1.14}$$

Notice that obtaining the simplified system (1.14) is equivalent to taking  $\varepsilon \rightarrow 0$  in (1.13) and dropping the subscript. The expansion above shows why it is enough to simply take the limit, as is often done in the literature [30].

By plotting a phase portrait of system (1.14) as seen in Figure 1.3 (a), it can be seen that the flow is trivial, where all flows either flow up or down, settling onto the nullcline arising in the second equation of (1.14). Hence, the nullcline is also a slow manifold defined by

$$\tilde{M} = \{(x_0, y_0) : 0 = x_0 - y_0\}. \quad (1.15)$$

This manifold is normally hyperbolic and attracting because

$$\frac{\partial \tilde{g}}{\partial y}(x, y, 0) \Big|_M = \frac{\partial}{\partial y_0}(x_0 - y_0) \Big|_{\tilde{M}} = -1 < 0.$$

Notice that there are no non hyperbolic points. We can also solve (1.14) to obtain the inner solution which is  $x_0(t) = \bar{x}$  and  $y_0(t) = \bar{x} + (\bar{y} - \bar{x})e^{-t}$  where  $x_0(0) = \bar{x}$  and  $y_0(0) = \bar{y}$ . Note, that  $\lim_{t \rightarrow \infty} x_0(t) = \bar{x} = \lim_{t \rightarrow \infty} y_0(t)$ , which is good to know when we later compare to the outer solution. With this, we are finished analyzing the fast reduced system, and now study the slow system.

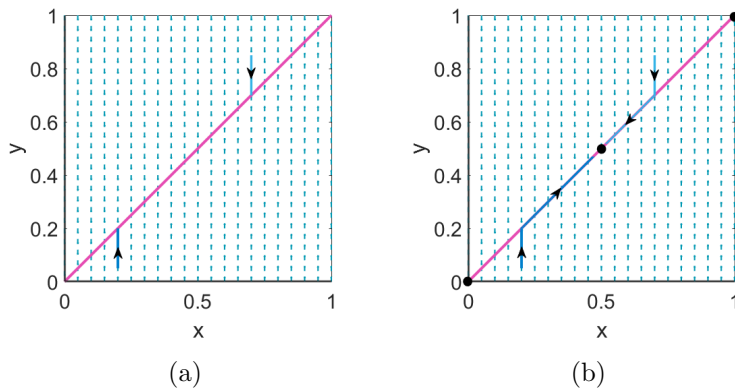


Figure 1.3: Phase portraits for example (1.13). For each image, the manifold  $\tilde{M}$  is given in pink, some trajectories are shown in blue, the equilibria are in black. In (a), a phase portrait of the fast system (1.14) is shown. In (b), a full phase portrait incorporating the fast and slow systems is shown, where the dynamics of the slow system are on the slow manifold.

Rescaling (1.13) using  $\tau = \varepsilon t$  gives

$$\begin{aligned}x' &= x(0.5 - y)(1 - x), \\ \varepsilon y' &= x - y.\end{aligned}\tag{1.16}$$

Performing an expansion in  $\varepsilon$  for  $x(\tau)$  and  $y(\tau)$  as we did previously and keeping the leading order terms  $\varepsilon^0$  yields the slow reduced system

$$\begin{aligned}x_0'(\tau) &= x_0(\tau)(0.5 - y_0(\tau))(1 - x_0(\tau)), \\ 0 &= x_0(\tau) - y_0(\tau).\end{aligned}\tag{1.17}$$

Again, obtaining system (1.17) is equivalent to letting  $\varepsilon \rightarrow 0$  in (1.16) and dropping the subscripts. We see that the first equation of (1.17) is a one dimensional ODE where  $y_0(\tau) = x_0(\tau)$ . This ODE can be analyzed using standard techniques to find that there are three steady states which are  $(x_1^*, y_1^*) = (0, 0)$ ,  $(x_2^*, y_2^*) = (0.5, 0.5)$ ,  $(x_3^*, y_3^*) = (1, 1)$  where  $(x_1^*, y_1^*)$  is unstable,  $(x_2^*, y_2^*)$  is stable and  $(x_3^*, y_3^*)$  is unstable on  $\tilde{M}$ . The stabilities of the equilibria outline the dynamics on the slow manifold  $\tilde{M}$ , which are summarized in (b) of Figure 1.3. System (1.17) can also be solved explicitly to give the outer solution where  $\lim_{\tau \rightarrow 0} x_0(\tau) = \bar{x} = \lim_{\tau \rightarrow 0} y_0(\tau)$ , since  $x_0(0) = \bar{x}$  and  $y_0(\tau) = x_0(\tau)$ . With this, we can “glue together” the inner and outer solutions by using the matching conditions. We have already calculated the limits, showing that the inner and outer solutions meet at  $(x_0, y_0) = (\bar{x}, \bar{x})$ . This is also seen in Figure 1.3, where the inner solution from the fast system and the outer solution which begins on the slow manifold meet on  $\tilde{M}$ , hence they meet at the coordinates  $(\bar{x}, \bar{x})$ . In practice, explicitly calculating the limits is challenging, but it is nice to illustrate how both solutions are put together for this example. Using Fenichel theory, we conclude that these solutions persist when  $\varepsilon \neq 0$  and  $\varepsilon$  is small.

## 1.5.2 Example 2: Tumor Growth Paradox

We now outline how the tumor growth paradox in (1.7) can be proved. First, we define the tumor growth paradox mathematically.

**Definition 1.5.4.** (*Tumor Growth Paradox*) [31] Let  $n_a(t)$  for times  $t \geq 0$  denote a tumor population with a spontaneous death rate  $a$  for TCs. The population exhibits a *tumor growth paradox* if there exist death rates  $a_1 < a_2$  and times  $t_1, t_2$  and  $T_0 > 0$  such that

$$n_{a_1}(t_1) = n_{a_2}(t_2) \quad \text{and} \quad n_{a_1}(t_1 + T) < n_{a_2}(t_2 + T) \quad \text{for} \quad (0 < T < T_0).$$

Next, we use geometric singular perturbation theory where the slow reduced system of (1.7) is given by

$$\begin{aligned} u' &= F(n)u, \\ 0 &= F(n)u + F(n)v - av, \end{aligned} \tag{1.18}$$

which captures the essential dynamics of (1.7). The trajectories of (1.18) converge to the slow manifold  $M_s$  given by

$$M_s = \{(u, v) : F(n)n - av, n = u + v\}. \tag{1.19}$$

Once the trajectories have converged to  $M_s$ , the trajectories flow to the global attractor  $(u^*, v^*) = (1, 0)$  on  $M_s$  which is proved in [31]. Using the properties of  $M_s$ , the tumor growth paradox can be proved analytically, where detailed calculations are done in [31]. Here, we show the tumor growth paradox numerically. In Figure 1.4, we see the illustration of the tumor growth paradox. In (a), the manifold with the lowest death rate is in green, and is almost diagonal whereas the manifold with the highest death rate is in blue and connects to the origin. In (b) the respective trajectories are shown. The trajectory in green solves (1.7) with  $a = 0.1$  where it starts at the initial condition  $u(0) = v(0) = 0.1$ . We see that the green trajectory, quickly converges to the manifold

and starts growing along it, towards the steady state  $(u^*, v^*) = (1, 0)$ . Now, the blue trajectory solves (1.7) with  $a = 1.1$  with the initial condition  $u(0) = v(0) = 0.1$ . We also see that the blue trajectory quickly converges to its respective manifold and grows along it, towards the steady state  $(u^*, v^*) = (1, 0)$ . At the final stop time of  $t = 900$ , the blue trajectory has grown to larger total density than the green trajectory with a lower growth rate, showcasing the tumor growth paradox.

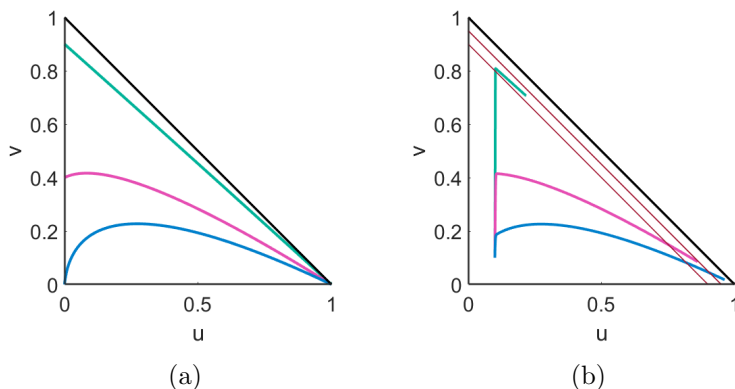


Figure 1.4: For each figure the diagonal black line corresponds to  $n = u + v = 1$ ,  $\delta = 0.01$ ,  $k, k_2, K = 1$ , and the final simulation time is  $t = 900$ . In (a) an illustration of 3 different manifolds is shown. The manifold in green has  $a = 0.1$ , the manifold in pink has  $a = 0.6$ , and the manifold in blue has  $a = 1.1$ . In (b) the corresponding solutions to (1.7). Each solution started at the same initial condition  $u(0) = v(0) = 0.1$ . The green trajectory is the solution of (1.7) with  $a = 0.1$ , the pink trajectory is the solution of (1.7) with  $a = 0.6$ , and the blue trajectory is the solution of (1.7) with  $a = 1.1$ . The brown lines are guide lines indicating when  $n = 0.9$  and when  $n = 0.95$ .

Above we outlined the main dynamics of (1.7), which are well understood, given the assumptions F1 and F2 [31]. A natural question that arises is what occurs if  $F(n)$  is extended to account for sizes at which tumor experiences poor growth or decay because the tumor population is unfit to sustain itself in an environment. This is one of the questions we answer in the following Chapters 2 and 3, by studying extending (1.7) to incorporate the Allee effect.

## 1.6 Outline

Here we summarize the structure of the thesis. In Chapter 2, we study the natural extension of (1.7), which has an Allee effect. We show that the arising model is a well defined dynamical system. The fast and slow systems are studied in detail in order to understand the full dynamics of this original model. We find that for certain parameter values the slow manifold  $M$  has non hyperbolic points. These non hyperbolic points separate attractive and repulsive regions of  $M$ , which show how the Allee effect impacts the dynamics. We also find that in the model there exists an Allee region, which captures the tumor densities that experience spontaneous decay. This regions size depends on the parameters such as the Allee threshold and the death rate of TCs. In particular, the Allee region can increase as those parameters increase. An issue with the proposed model in Chapter 2, is that it is not biologically realistic since some solutions may become negative. We address this issue in Chapter 3, where we make a modification to the system from Chapter 2 to avoid negative solutions. The analysis from Chapter 2 carries over almost unchanged and we find that in the modified model there also exists an Allee region. Next, we examine how cytotoxic treatments influence the Allee region. We find that even though the treatment can increase the Allee region, its maximum size is limited by the Allee threshold. In Chapter 4, we use a different approach to study the Allee effect in cancer stem cell models. In particular, we follow the approach as in [38] and start with the model (1.4) that is based on the CSC self renewal probability  $p$ . To this model we add TC dynamics, competition between CSCs and TCs, and a positive feedback mechanism which stimulates self-renewal of CSCs. We show that the Allee region can also exist in this case, given that the parameters satisfy the required criteria. We find that that increasing the death rate can increase the Allee region but decreasing self-renewal probability is much more effective at increasing the Allee region. In Chapter 5, we reduce the cancer stem cell models and fit them to NSCLC data. We find that accounting for the Allee effect and the distinction between CSCs and TCs are not required to explain the data. However, accounting for the latency time effect, by

including a damaged cell compartment explains the tumor shrinkage that occurs post treatment well. Further, we find that the treatment outcome can be indicated by a ratio comprised of growth rate, clearance rate, and chemotherapy kill rate parameters. We conclude the thesis with a discussion chapter, where we summarize the key results and propose possible future work.

## Chapter 2

# Cancer Stem Cell Model with an Allee Effect

To begin our study of the Allee effect in cancer stem cell driven solid tumors, we start modifying (1.7). By setting the mitosis rates  $k = k_2 = 1$  for simplicity, we obtain

$$\begin{aligned}\dot{u} &= \delta F(n)u, \\ \dot{v} &= (1 - \delta)F(n)u + F(n)v - av,\end{aligned}\tag{2.1}$$

where  $u$  is the CSC density,  $v$  is the TC density,  $\delta$  is the fraction of symmetric divisions,  $a$  is the TC death rate, and  $n = u + v$ . We let  $F(n) = (1 - n)(n - A)$  where now  $F(n)$  represents the cell fitness to reproduce in an environment. So if  $F(n) > 0$ , then cells are in a favourable environment and have space to reproduce but if  $F(n) < 0$  then cells are in an unfavourable environment and thus die. Here,  $A$  is the Allee constant. Since our densities are normalized, we only consider the cases when  $|A| < 1$ . When  $0 < A < 1$ , this corresponds to a case when there is a strong Allee effect, that is  $A$  forms a “density threshold.” In this case, when the total density  $n$  is greater than  $A$ , the density grows due to being in a favourable environment, but if density is less than  $A$ , the density decays. Now, in the case when  $-1 < A \leq 0$ , there is a weak Allee effect, meaning that smaller densities grow slower than expected.

We emphasize that the model (2.1) is not biologically relevant, since there are trajectories that become negative if they begin in the biologically relevant domain  $D = \{(u, v) : u \in [0, 1], v \in [0, 1]\}$ . We address this issue in Chapter 3 and for now focus on understanding how solutions of (2.1) behave. By doing this first, we can more easily understand the behaviour of the modified system (2.1) which we introduce later.

We begin by first recalling the definition of a dynamical system.

**Definition 2.0.1.** (*Dynamical System*, Perko [53]). Let  $X$  be an open subset of  $\mathbb{R}^n$ . Then a *dynamical system* on  $X$  is a  $C^1$ -map defined by

$$\varphi : \mathbb{R} \times X \rightarrow X$$

where if  $\varphi_t(x) = \varphi(t, x)$  then  $\varphi_t$  satisfies the following

1.  $\varphi_0(x) = x$  for all  $x \in X$
2.  $\varphi_t(\varphi_s(x)) = \varphi_{t+s}(x)$  for all  $t, s \in \mathbb{R}$  and  $x \in X$

In our proof that (2.1) is a dynamical system we make use of the Picard–Lindelöf theorem, which states the conditions required for the existence and uniqueness of solutions to an ODE system.

**Theorem 2.0.1.** (*Picard–Lindelöf*, Teschl [65]). Suppose  $f \in C(U, \mathbb{R}^n)$ , where  $U$  is an open subset of  $\mathbb{R}^{n+1}$ , and  $(t_0, x_0) \in U$ . If  $f$  is locally Lipschitz continuous in the second argument, uniformly with respect to the first, then there exists a unique local solution  $\bar{x}(t) \in C^1(I)$  of the initial value problem

$$\dot{x} = f(t, x), \quad x(t_0) = x_0,$$

where  $I$  is some interval around  $t_0$ .

**Lemma 2.0.2.** Together with an initial condition  $(u(0), v(0)) = (\bar{u}, \bar{v})$ ,  $\bar{u}, \bar{v} \in \mathbb{R}$ , (2.1) forms a dynamical system in  $\mathbb{R}^2$ .

*Proof.* Let  $x = (\bar{u}, \bar{v})$  be the initial condition and

$$\mathbf{G}(u, v) = \begin{pmatrix} \delta F(n)u \\ (1 - \delta)F(n)u + F(n)v - av \end{pmatrix},$$

that is  $\mathbf{G}(u, v)$  denotes the right hand side of (2.1). Because  $\mathbf{G}(u, v)$  is differentiable at every point, it follows from the Mean Value Theorem that  $\mathbf{G}(u, v)$  is locally Lipschitz continuous. Hence, by the Picard–Lindelöf Theorem 2.0.1 there exists a unique solution  $\varphi(t, x) = (u(t), v(t))$  solving (2.1).

Now, item 1 from Definition 2.0.1 follows immediately due to (2.1) having an initial condition. To show item 2 from Definition 2.0.1, fix  $s$ , and let  $\hat{\varphi}(t, x) = \varphi(t, \varphi(s, x_0))$  and  $\tilde{\varphi}(t, x) = \varphi(t + s, x_0)$  where  $s$  and  $x_0 \in X$  are arbitrary. Then,  $\hat{\varphi}(t, x)$  and  $\tilde{\varphi}(t, x)$  also solve (2.1). Hence,

$$\frac{d}{dt}(\hat{\varphi}(t, x)) = \mathbf{G}(\hat{\varphi}(t, x)),$$

$$\frac{d}{dt}(\tilde{\varphi}(t, x))_t = \mathbf{G}(\tilde{\varphi}(t, x)),$$

with initial conditions  $\hat{\varphi}(0, x) = \hat{\varphi}_0(x) = \varphi(s, x_0)$  (by item 1) and  $\tilde{\varphi}(0, x) = \varphi(s, x_0)$ . Since the initial conditions are the same, it follows that  $\hat{\varphi}(t, x) = \tilde{\varphi}(t, x)$  by uniqueness of solutions.  $\square$

Now that we have established that (2.1) defines a dynamical system in  $\mathbb{R}^2$ , our goal in this chapter is to study and describe its full dynamics.

## 2.1 Fast System

The system (2.1) is naturally in the fast system form since  $\delta$  is small [19, 31]. So, we can simplify the system by letting  $\delta \rightarrow 0$ . This yields

$$\begin{aligned} \dot{u} &= 0, \\ \dot{v} &= F(n)u + F(n)v - av. \end{aligned} \tag{2.2}$$

The nullcline in the second equation of (2.2) forms a manifold

$$M := \{(u, v) \in \mathbb{R}^2 : 0 = f(u, v), n = u + v\}. \quad (2.3)$$

where

$$f(u, v) = F(n)n - av, \quad (2.4)$$

and

$$F(n) = (1 - n)(n - A). \quad (2.5)$$

We will now show that  $M$  in (2.3) has normally hyperbolic regions and also non hyperbolic points. By differentiating  $f(u, v)$  given in (2.4), we find that

$$\begin{aligned} \left. \frac{\partial f}{\partial v} \right|_M &= F'(u + v)(u + v) + F(u + v) - a, \\ &= -3(u + v)^2 + 2(1 + A)(u + v) - A - a. \end{aligned} \quad (2.6)$$

Now if we set (2.6) to zero and solve for  $u + v$ , this will give the points at which the manifold is not hyperbolic. Hence, we find that

$$u + v = \frac{(1 + A) \pm \sqrt{(1 + A)^2 - 3(A + a)}}{3}. \quad (2.7)$$

We note that when  $(1 + A)^2 - 3(A + a) < 0$  there are no non hyperbolic points. Therefore, condition (2.7) determines when non hyperbolic points exist, which is summarized below.

**Lemma 2.1.1.** *(Sufficient conditions for the existence of non hyperbolic points)*

Let

$$d = (1 + A)^2 - 3(A + a). \quad (2.8)$$

Model (2.1) contains

- i) two non hyperbolic points if  $d > 0$ ,*
- ii) one non hyperbolic point if  $d = 0$ ,*

iii) no non hyperbolic points if  $d < 0$ .

If  $d < 0$ , then  $M$  is normally hyperbolic. Hence, for the following calculations, we assume that the condition  $d \geq 0$  holds. We rearrange (2.7) to obtain

$$u = k_{\pm} - v, \quad (2.9)$$

where

$$k_{\pm} = \frac{(1 + A) \pm \sqrt{d}}{3} \quad (2.10)$$

with  $d$  defined by (2.8). Next,  $v$  values of the non hyperbolic points can be found by substituting (2.9) into  $f(u, v) = 0$  (where  $f(u, v)$  is defined by in (2.4)) which is then solved for  $v$  giving

$$v_{\pm} = \frac{-k_{\pm}^3 + k_{\pm}^2(1 + A) - Ak_{\pm}}{a}. \quad (2.11)$$

In summary,  $k_{\pm}$  has at most two possible values, hence we obtain at most two non hyperbolic points which we denote by  $(u_{nh}, v_{nh})$ . Note that it is possible to obtain the coordinates of the non hyperbolic points if  $k_{\pm}$  values are known by using equations (2.9) and (2.11). To be specific, we represent the non hyperbolic point determined from the value of  $k_+$  and  $k_-$  by  $(u_{nh+}, v_{nh+})$  and  $(u_{nh-}, v_{nh-})$ , respectively. Notice that if  $k_+ = k_-$ , then  $(u_{nh+}, v_{nh+}) = (u_{nh-}, v_{nh-})$  and there are no non hyperbolic points if  $k_{\pm}$  are complex. We also define a set  $N$  that contains the non hyperbolic points, that is

$$N = \{(u_{nh+}, v_{nh+}), (u_{nh-}, v_{nh-})\}. \quad (2.12)$$

Having found the explicit formulas for the coordinates of the non hyperbolic points, we use this knowledge to prove that there exist two attractive branches and one repelling branch on  $M$  (2.3).

**Lemma 2.1.2.** *Let  $d$  be defined by (2.8) and  $k_{\pm}$  defined by (2.10) then*

- i) If  $d \geq 0$  then  $M$  in (2.3) is normally hyperbolic and attracting when  $u + v > k_+$  or  $u + v < k_-$ .*

ii) If  $d > 0$  then  $M$  in (2.3) is normally hyperbolic and repelling when  $k_- < u + v < k_+$ .

iii) If  $d < 0$  and  $0 < A < 1$  then  $M$  in (2.3) is normally hyperbolic and attracting everywhere.

*Proof.* If (2.9) is substituted into (2.6), we obtain the following

$$-3k_{\pm}^2 + 2(1 + A)k_{\pm} - A - a = 0, \quad (2.13)$$

since the  $\frac{\partial f}{\partial v} = 0$  at the non hyperbolic points. To show item i), we start with  $u + v > k_+$  case. Let  $c > 0$ ,  $c \in \mathbb{R}$  and set  $u + v = k_+ + c > k_+$  so that

$$u = k_+ + c - v. \quad (2.14)$$

Substituting (2.14) back into the (2.6) gives

$$\frac{\partial f}{\partial v} = -3k_+^2 - 6k_+c - 3c^2 + 2(1 + A)k_+ + 2(1 + A)c - A - a.$$

Using (2.13), we can simplify the above equation by removing 3 terms and obtain

$$\frac{\partial f}{\partial v} = c(-6k_+ - 3c + 2(1 + A)).$$

Since

$$\begin{aligned} 6k_+ &= 2(1 + A) + 2\sqrt{d}, \\ &> 2(1 + A), \end{aligned}$$

we see that  $\frac{\partial f}{\partial v} < 0$  for all  $c$ , showing that when  $u + v > k_+$ ,  $M$  in (2.3) is attracting.

Similarly for the  $u + v < k_-$  case, we let  $u + v = k_- - c < k_-$  where  $c < 0$ ,  $c \in \mathbb{R}$  and substitute

$$u = k_- - c - v \quad (2.15)$$

into (2.6) to get

$$\frac{\partial f}{\partial v} = -3k_-^2 + 6k_-c - 3c^2 + 2(1+A)k_- - 2(1+A)c - A - a.$$

Using (2.13) we remove the three terms and obtain

$$\frac{\partial f}{\partial v} = c(6k_- - 3c - 2(1+a)).$$

In this case

$$\begin{aligned} 6k_- &= 2(1+a) - 2\sqrt{d}, \\ &< 2(1+a), \end{aligned} \tag{2.16}$$

which means that  $\frac{\partial f}{\partial v} < 0$  for all  $c$ , showing that when  $u + v < k_-$ ,  $M$  in (2.3) is also attracting.

In order to show item *ii*), we take  $u + v = k_+ - c$  where

$$0 < c < k_+ - k_- = \frac{2\sqrt{d}}{3}. \tag{2.17}$$

This makes it so  $k_- < u + v < k_+$  (since  $k_- < k_+$ ) and hence

$$u = k_+ - c - v. \tag{2.18}$$

Then substituting (2.18) into (2.6) gives

$$\frac{\partial f}{\partial v} = -3k_+^2 + 6k_+c - 3c^2 + 2(1+A)k_+ - 2(1+A)c - A - a.$$

Using (2.13), we again cancel the 3 terms and obtain

$$\frac{\partial f}{\partial v} = c(6k_+ - 3c - 2(1+A)).$$

Substituting in (2.10) (the value of  $k_+$ ) into the above equation gives

$$\begin{aligned}\frac{\partial f}{\partial v} &= c(2(1+A) + 2\sqrt{d} - 3c - 2(1+A)), \\ &= c(2\sqrt{d} - 3c).\end{aligned}$$

Since

$$3c < 2\sqrt{d},$$

which follows from (2.17),  $\frac{\partial f}{\partial v} > 0$  for all  $c > 0$  showing that when  $k_- < u + v < k_+$ ,  $M$  in (2.3) is repelling.

To show item *iii*), note that  $M$  is normally hyperbolic when  $d < 0$ . Further, because there are no non hyperbolic points,  $\frac{\partial f}{\partial v}$  in (2.6) is either only positive or only negative as it cannot cross the axis, meaning it cannot switch signs. Hence, it is enough to evaluate  $\frac{\partial f}{\partial v}\Big|_{(0,0)}$  where  $(0,0) \in M$  to determine the sign of  $\frac{\partial f}{\partial v}$ . We see that  $\frac{\partial f}{\partial v}\Big|_{(0,0)} = -A - a$  hence  $\frac{\partial f}{\partial v} < 0$  if  $0 < A < 1$  meaning that  $M$  is attracting in this case.  $\square$

For Lemma 2.1.2, we have only shown item *iii*) for the strong Allee effect case, since by assumption  $0 < A < 1$ . The weak Allee effect case  $-1 < A \leq 0$  is shown below. Note that item *i*) and *ii*) in Lemma 2.1.2 still hold when  $|A| < 1$ .

**Corollary 2.1.2.1.** *Let  $d$  be defined by (2.8). Assume  $-1 < A \leq 0$  and  $d < 0$ . Then  $M$  in (2.3) is normally hyperbolic and attracting everywhere.*

*Proof.* From Lemma 2.1.2 it is sufficient to show that  $\frac{\partial f}{\partial v}\Big|_{(0,0)} = -A - a < 0$ . If  $A = 0$ , this follows immediately.

If  $A < 0$ , it is enough to show that  $-A < a$ . Rearranging (2.8) gives that

$$(A^2 - A + 1)/3 < a.$$

From here, since

$$0 < (A + 1)^2 \tag{2.19}$$

for  $|A| < 1$ , it follows that

$$-A < (A^2 - A + 1)/3$$

by rearranging (2.19). □

Note that the Implicit Function Theorem states that if

$$\frac{\partial f}{\partial v} \Big|_{(u_0, v_0)} \neq 0$$

then  $v = v(u)$  in a neighbourhood of  $(u_0, v_0)$ . Hence, the neighbourhoods of the non hyperbolic points is exactly where  $v$  is not a graph of  $u$ . This means that when non hyperbolic points exist,  $M$  in (2.3) will need to be studied in sections. Further, we can only apply Fenichel's theorems to the normally hyperbolic regions of  $M$ , and the non hyperbolic points need to be studied separately, which we do later in this chapter.

Lemma 2.1.2 shows that  $M$  given by (2.3) can be divided into 3 sections, I and III being the attracting/stable branches and II being the repelling/unstable branch granted  $d > 0$ . The branches are separated by the non hyperbolic points as illustrated in Figure 2.1 (a) where  $M$  is the pink curve and the open white circles are the non hyperbolic points. If  $d = 0$ , then only item *i*) of Lemma 2.1.2 holds and consequently there are two attracting branches I and III, and branch II degenerates to a single non hyperbolic point. This is seen in Figure 2.1 (b). Finally, if  $d < 0$ , then  $M$  has one branch that is normally hyperbolic and attracting as seen in Figure 2.1 (c). These branches can be mathematically formulated as

$$M := \begin{cases} \text{I : } 0 := F(n)(u + v) - av, u + v > k_+ \\ \text{II : } 0 := F(n)(u + v) - av, k_- < u + v < k_+ \quad \cup \quad N \\ \text{III : } 0 := F(n)(u + v) - av, u + v < k_- \end{cases} \quad (2.20)$$

where  $N$  is again the set of non hyperbolic points defined by (2.12). In (2.20) I, III correspond to the attractive branches and II corresponds to the repelling branch. Note

that in this formulation, it follows from Implicit Function Theorem that each branch is a graph of  $u$ , since no branch contains a non hyperbolic point.

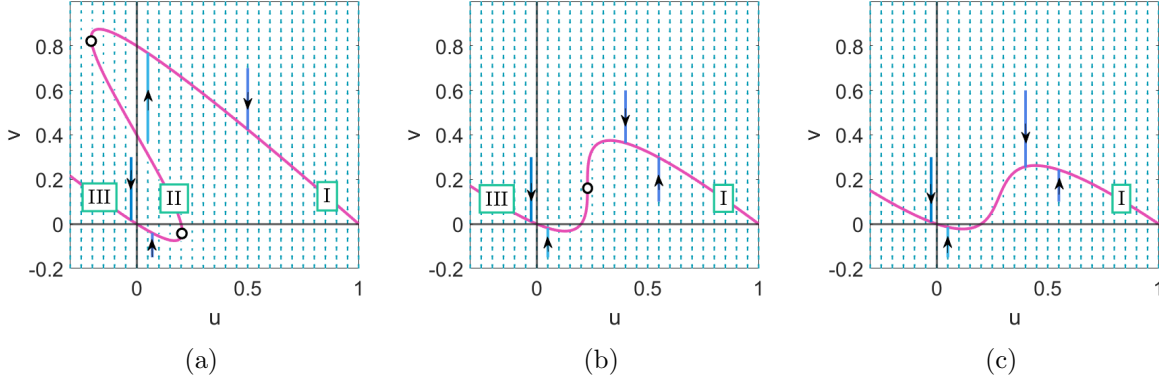


Figure 2.1: Phase portraits of (2.2). In each figure, the curve in pink is the manifold  $M$  defined in (2.20) which comprised of branches separated by a non hyperbolic point(s) (open white circle(s)). The lines in blue are the flows of the solutions which either flow up or down. In (a),  $a = 0.12$  and  $A = 0.2$  yielding three branches. In (b),  $a = 0.28$  and  $A = 0.2$  yielding two attractive branches. In (c),  $a = 0.4$  and  $A = 0.2$  yielding one attractive branch. The parameters were chosen like this to purely illustrate the possible cases.

In addition to summarizing the possible cases of  $M$  in (2.20), Figure 2.1 also shows the dynamics of the reduced fast system (2.2). The lines in blue illustrate the trajectories of the solutions. Examining (a) in Figure 2.1 closer, we see that if the initial condition is not on  $M$  then the trajectories converge to either the stable branch I or III. If trajectories are near the unstable branch II, they repel from it, and converge to one of the stable branches. Similar behaviour can be seen in (b) and (c) which lack the repelling branch. In this case the trajectories simply converge to the nearby stable branch. Note that if the initial condition of the trajectory is exactly on  $M$ , it stays at that point for all time. Hence, we see that the dynamics are trivial for (2.2), and we need to look at the slow system to obtain the dynamics on  $M$ , which we do in the following section.

To finish this section, we show that  $M$  in (2.20) is well defined.

**Lemma 2.1.3.**  *$M$  in (2.20) is well defined where the non hyperbolic points connect continuously to the branches.*

*Proof.* Denote the non hyperbolic points by  $(u_{nh}, v_{nh})$ . We first compute  $\frac{\partial f(u,v)}{\partial u}$  where  $f(u, v)$  is defined in (2.4), and  $F(n) = (1 - n)(n - A)$ ,  $n = u + v$ . So,

$$\begin{aligned}\frac{\partial f(u, v)}{\partial u} &= -(n - A)n + (1 - n)n + (1 - n)(n - A) \\ &= -3n^2 + 2(1 + A)n - A.\end{aligned}\tag{2.21}$$

Using (2.21) we verify that  $u = u(v)$  in a neighbourhood of a non hyperbolic point. Indeed,

$$\left. \frac{\partial f(u, v)}{\partial u} \right|_{(u_{nh}, v_{nh})} = a \neq 0$$

since (2.6) is zero at the non hyperbolic points  $(u_{nh}, v_{nh})$ . So by the Implicit Function Theorem,  $u$  can be expressed as a function of  $v$  ( $u = u(v)$ ). Now, we can differentiate  $f(u(v), v) = 0$  implicitly by  $v$  and solve for  $u'(v)$  to obtain

$$u'(v) = -1 + \frac{a}{-n(n - A) + n(1 - n) + (1 - n)(n - A)},\tag{2.22}$$

where  $n = u(v) + v$ . If we substitute the non hyperbolic points  $(u_{nh}, v_{nh})$  into (2.22), we get  $u'(v_{nh}) = 0$ . Hence, the derivative exists at the non hyperbolic points meaning that the graph  $u(v)$  is continuous and differentiable at the non hyperbolic points. Going one step further, we can calculate the second derivative

$$u''(v) = \frac{-2a(u'(v) + 1)(-(n - A) - n + (1 - n))}{(-n(n - A) + n(1 - n) + (1 - n)(n - A))^2}.$$

If we substitute in a non hyperbolic point  $(u_{nh}, v_{nh})$ , we obtain

$$u''(v_{nh}) = \frac{-2a(-((u_{nh} + v_{nh}) - A) - (u_{nh} + v_{nh}) + (1 - (u_{nh} + v_{nh})))}{a^2}.\tag{2.23}$$

where  $u'(v_{nh}) = 0$ . Since the second derivative exists, the first derivative  $u'(v)$  is continuous at the non hyperbolic points. Hence,  $M$  is well defined smooth manifold.  $\square$

## 2.2 Slow System

In this section, we study the slow system of (2.1) to obtain the remaining dynamics. The slow system is obtained by rescaling time with  $\tau = \delta t$  where  $t$  corresponds to the fast time scale and  $\tau$  corresponds to the slow time scale. This yields

$$\begin{aligned}\delta u' &= \delta F(n)u, \\ \delta v' &= (1 - \delta)F(n)u + F(n)v - av.\end{aligned}\tag{2.24}$$

Then, taking  $\delta \rightarrow 0$  gives the following slow reduced system

$$\begin{aligned}u' &= F(n)u, \\ 0 &= F(n)u + F(n)v - av.\end{aligned}\tag{2.25}$$

The first equation in (2.25) defines the dynamics on the normally hyperbolic regions of the nullcline given by the second equation. The nullcline of the second equation is precisely the manifold  $M$  which was previously defined by (2.3). We define

$$g(u, v) = F(n)u.\tag{2.26}$$

where  $F(n) = (1 - n)(n - A)$ . Using (2.26), we will now study the dynamics on each branch. For the following three subsections we consider the case when three branches exist, that is  $d > 0$ . We calculate the equilibria on each branch and describe their stabilities on  $M$ . Note that when we talk about the stability of an equilibrium, we are assuming that it is not a non hyperbolic point. In the case when the equilibrium coincides with a non hyperbolic point, we have to study the stability numerically since no branch is a graph in a neighbourhood of an equilibrium, as was shown before.

### 2.2.1 Dynamics on Branch I

We first study the dynamics on the attracting branch I when  $d > 0$ . The equilibria are obtained by setting the first equation of (2.25) to zero and calculating the critical points. If  $|A| < 1$ , the equilibrium  $(u_1^*, v_1^*) = (1, 0)$  is always present on branch I. If, in addition,

$$(1 + A)^2 - 4(A + a) > 0, \quad (2.27)$$

then  $(u_2^*, v_2^*) = (0, v_+)$  exists on branch I, where

$$v_+ = \frac{1 + A + \sqrt{(1 + A)^2 - 4(A + a)}}{2}, \quad (2.28)$$

which was obtained by solving

$$0 = (1 - v)(v - A) - \alpha. \quad (2.29)$$

Essentially,  $(u_2^*, v_2^*) = (0, v_+)$  is present on branch I when  $v_+$  is a real number and not a non hyperbolic point.

We illustrate some examples in Figure 2.2 where the pink and blue curves are example manifolds  $M$  which are defined by (2.20). In Figure 2.2, the equilibria are denoted by black circles and the non hyperbolic points are denoted by open circles. The non hyperbolic point  $(u_{nh+}, v_{nh+})$  connects branch II and I for each example manifold, and the dashed line is a helper line showing a segment of  $u + v = k^+$  where the value of  $k_+$  can be determined from the intersection of the dashed line and the u-axis. Similarly, the non hyperbolic point  $(u_{nh-}, v_{nh-})$  connects branch II and III with its respective  $k_-$  value labeled. In Figure 2.2 (a),  $A > 0$  and we see that the equilibrium  $(u_1^*, v_1^*) = (1, 0)$  is always present on branch I but the presence of  $(u_2^*, v_2^*) = (0, v_+)$  depends on the parameters. In Figure 2.2 (b),  $A < 0$  and in both examples,  $(u_1^*, v_1^*)$  and  $(u_2^*, v_2^*)$  are present. It is also possible to have only one equilibrium  $(u_1^*, v_1^*)$  on branch I by making (2.27) not hold, which correlates to shifting  $k_+$ , as shown by the example manifolds in

(a).

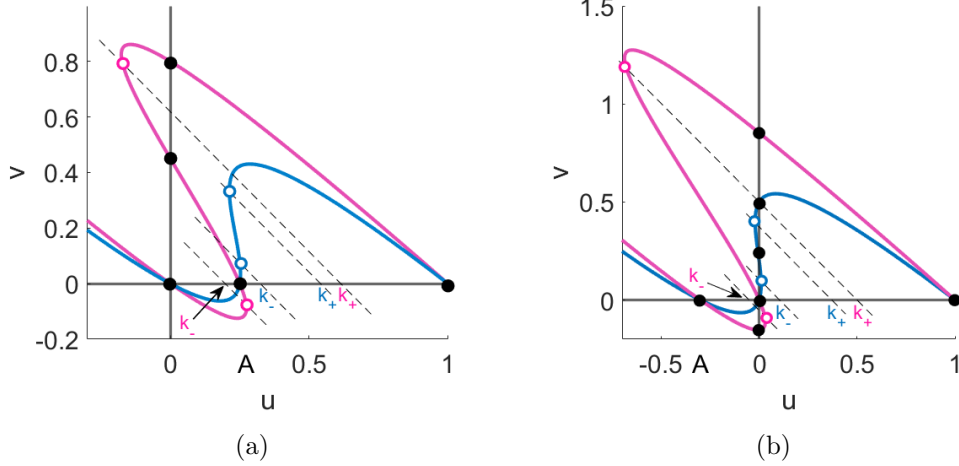


Figure 2.2: For each figure, the pink and blue curves are example manifolds  $M$  defined by (2.20), the equilibria are denoted by black circles and the corresponding non hyperbolic points in each manifold are denoted by open circles. The dashed lines are helper lines showing segments of  $u + v = k_+$  and  $u + v = k_-$  lines. The  $k_+$  and  $k_-$  labels on the  $u$ -axis show where the respective  $k_+$  and  $k_-$  would fall. In (a),  $A > 0$  and fixed for both manifolds In (b),  $A < 0$  and fixed for both manifolds.

To determine the stability of these equilibria on branch I, we can use  $g(u, v)$  defined in (2.26). If  $g(u, v(u))$ , then we can use linear stability analysis to classify the stability of equilibria on  $M$ . This can be done since  $M$  is locally invariant by Fenichel theory and  $M$  is a smooth manifold. The implicit derivative of  $g(u, v(u))$  is given by

$$\frac{\partial g(u, v(u))}{\partial u} = (-2(u + v(u))(1 + v'(u)) + (1 + A)(1 + v'(u)))u + F(n). \quad (2.30)$$

where  $F = (1 - n)(n - A)$ . As noted before, each branch is a graph of  $u$  meaning that  $f(u, v) = f(u, v(u))$  where  $f(u, v)$  is defined in (2.4). Hence, we can use (2.30) to determine the stability of equilibria on each branch. Before we do that, we prove some useful inequalities.

**Lemma 2.2.1.** *Suppose that  $d \geq 0$ ,  $|A| < 1$ , and  $a > 0$ .*

*i) On branch I,  $1 + v'(u) > 0$  at  $(u, v) = (1, 0)$ .*

ii) On branch III, given a fixed  $A$ , if  $0 < A < k_-$  or  $A < 0$  then  $1 + v'(u) > 0$  at  $(u, v) = (A, 0)$ .

iii) On branch II, given a fixed  $A$ , if  $A > k_- > 0$  then  $1 + v'(u) < 0$  at  $(u, v) = (A, 0)$ .

*Proof.* We show the inequality in item i) by using implicit differentiation. First, we differentiate  $f(u, v(u)) = 0$  defined in (2.4) with respect to  $u$  to obtain

$$\begin{aligned} 0 &= (-1 - v'(u))(u + v(u) - A)(u + v) + (1 - u - v(u))(1 + v'(u))(u + v(u)) \\ &\quad + (1 - u - v(u))(u + v(u) - A)(1 + v'(u)) - av'(u). \end{aligned} \quad (2.31)$$

Plugging in  $(u, v(u)) = (1, 0)$  into (2.31), we obtain

$$0 = (-1 - v'(u))(1 - a) - av'(u).$$

Solving the above equation for  $v'(u)$  gives

$$v'(u) = \frac{1 - A}{-1 + A - a} = -1 + \frac{a}{1 - A + a} \quad (2.32)$$

where  $a/(1 - A + a) > 0$ . Hence,  $1 + v'(u) > 0$  at  $(u, v) = (1, 0)$ .

To show item ii), we solve (2.31) for  $v'(u)$  and substitute in  $(u, v) = (A, 0)$  which gives

$$v'(u) = \frac{A^2 - A}{-A^2 + A - a} = -1 + \frac{a}{A^2 - A + a}. \quad (2.33)$$

If  $A > 0$ , then

$$A < k_- = \frac{(1 + A) - \sqrt{(1 + A)^2 - 3(A + a)}}{3}$$

which can be rewritten as

$$\sqrt{(1 + A)^2 - 3(A + a)} < 1 - 2A.$$

Squaring both sides and simplifying yields the condition

$$0 < A^2 - A + a. \quad (2.34)$$

So,  $v'(u) + 1 > 0$  at  $(u, v) = (A, 0)$  when  $0 < A < k_-$ . When  $A < 0$ , it follows immediately from (2.33) that  $1 + v'(u) > 0$  at  $(u, v) = (A, 0)$ . It also follows that  $1 + v'(u) < 0$  when  $A > k_- > 0$  at  $(u, v) = (A, 0)$  since the inequality flips in (2.34) which shows item *iii*).

□

**Lemma 2.2.2.** (*Equilibria Stability on Branch I*) Suppose that  $(u_1^*, v_1^*) = (1, 0)$  and  $(u_2^*, v_2^*) = (0, v_+)$  where  $v_+$  is defined in (2.28) are not non hyperbolic points. The equilibrium  $(u_1^*, v_1^*) = (1, 0)$  always exists on branch I, and is stable on  $M$ . The equilibrium  $(u_2^*, v_2^*) = (0, v_+)$  is unstable on branch I, if it exists.

*Proof.* Substituting in the equilibrium point  $(u_1^*, v_1^*) = (1, 0)$  into (2.30) we obtain

$$\begin{aligned} \left. \frac{\partial g}{\partial u} \right|_{(1,0)} &= -2(1 + v'(u)) + (1 + A)(1 + v'(u)) \\ &= (1 + v'(u))(-1 + A) \\ &< 0 \end{aligned}$$

since  $|A| < 1$  and  $1 + v'(u) > 0$  at  $(1, 0)$  by item *i*) in Lemma 2.2.1. This shows that  $(u_1^*, v_1^*) = (1, 0)$  is stable on  $M$ .

Now we substitute  $(u_2^*, v_2^*) = (0, v_+)$  into (2.30) and find that

$$\left. \frac{\partial g}{\partial u} \right|_{(0,v_+)} = a > 0$$

which was obtained by substituting in (2.29) into (2.30). This means that  $(u_2^*, v_2^*)$  is unstable on  $M$  given that it is not a non hyperbolic point.

□

## 2.2.2 Dynamics on Branch III

Now, we analyze the dynamics on the other attracting branch III. Like branch I, if  $A > 0$  this branch can have up to two equilibria  $(u_0^*, v_0^*) = (0, 0)$  and  $(u_3^*, v_3^*) = (A, 0)$ . This branch always has the  $(u_0^*, v_0^*)$  equilibrium. We see this in Figure 2.2 (a), where the pink curve denotes the case when only  $(u_0^*, v_0^*) = (0, 0)$  is on branch III and the blue curve denotes the case when both equilibria are present on branch III. Notice that in the case that  $(u_3^*, v_3^*)$  is present,  $A < k_-$ .

We summarize the stabilities in a lemma.

**Lemma 2.2.3.** *(Equilibria Stability on Branch III, Strong Allee Effect  $A > 0$ ) Suppose  $(u_0^*, v_0^*) = (0, 0)$  and  $(u_3^*, v_3^*) = (A, 0)$  are not non hyperbolic points. If  $A > 0$ ,  $(u_0^*, v_0^*) = (0, 0)$  always exists on branch III, and is stable on  $M$ . If  $A < k_-$ , the equilibrium,  $(u_3^*, v_3^*) = (A, 0)$  exists and is unstable on branch III.*

*Proof.* Substituting  $(u_0^*, v_0^*) = (0, 0)$  into (2.30) we obtain

$$\left. \frac{\partial g}{\partial u} \right|_{(0,0)} = A.$$

Hence,  $(u_0^*, v_0^*)$  is stable when  $A > 0$ .

The equilibrium  $(u_3^*, v_3^*) = (A, 0)$  can only exist on branch III when  $A < k_-$ . This is because branch III contains all points on  $M$  which satisfy  $u + v < k_-$  by definition in (2.20). Hence, it also contains  $(u_3^*, v_3^*) = (A, 0)$  since  $(u_3^*, v_3^*) \in M$ . Note that if  $A \geq k_-$ , branch III, cannot contain  $(u_3^*, v_3^*) = (A, 0)$ .

Substituting in  $(u_3^*, v_3^*) = (A, 0)$  into (2.30) gives

$$\begin{aligned} \left. \frac{\partial g}{\partial u} \right|_{(A,0)} &= (-2A(1 + v'(u)) + (1 + A)(1 + v'(u))A) + 0, \\ &= (1 + v'(u))(1 - A)A. \end{aligned} \tag{2.35}$$

By Lemma 2.2.1 item *ii*),  $1 + v'(u) > 0$  at  $(u, v) = (A, 0)$ . So if  $A > 0$ , then  $(u_3^*, v_3^*)$  is unstable on branch III.

□

For the case when  $A < 0$ , branch III can also have up to two equilibria where  $(u_3^*, u_3^*) = (A, 0)$  always exists. The equilibrium  $(u_4^*, v_4^*) = (0, v_-)$  can also exist on this branch given that (2.27) is satisfied where

$$v_- = \frac{1 + A - \sqrt{(1 + A)^2 - 4(A + a)}}{2}. \quad (2.36)$$

The equilibrium  $(u_0^*, v_0^*) = (0, 0)$  may be present on this branch instead of  $(u_4^*, v_4^*)$ . These cases are shown in Figure 2.2 (b). The pink manifold shows the case when  $(u_3^*, u_3^*) = (A, 0)$  and  $(u_4^*, v_4^*) = (0, v_-)$  exist on branch III. In that case  $k_- < 0$ . The blue manifold shows the case when  $(u_3^*, u_3^*)$  and  $(u_0^*, v_0^*) = (0, 0)$  exist on branch III and this occurs when  $k_- > 0$ . We summarize the dynamics in a lemma.

**Lemma 2.2.4.** (*Equilibria Stability on Branch III, Weak Allee Effect  $A < 0$* ) Suppose that  $A < 0$ . Then,  $(u_3^*, u_3^*) = (A, 0)$  always exists on branch III and is stable on  $M$ . If (2.27) holds, then  $(u_4^*, v_4^*) = (0, v_-)$  where  $v_-$  is defined by (2.36) can exist on branch III and is unstable on  $M$ . If the equilibrium  $(u_0^*, v_0^*) = (0, 0)$  exists on branch III, it is unstable on  $M$ .

*Proof.* From the calculations in the proof of Lemma 2.2.3, we see from the equation (2.35), that  $(u_3^*, u_3^*) = (A, 0)$  is stable on  $M$  if  $A < 0$  (which also used Lemma 2.2.1 item *ii*)).

Using (2.30), we compute

$$\left. \frac{\partial g}{\partial u} \right|_{(0, v_-)} = a > 0$$

which was obtained by substituting in (2.29) into (2.30). We see that  $(u_4^*, v_4^*)$  is always unstable on  $M$ .

From the calculation in the proof of Lemma (2.2.3), we see that  $(u_0^*, v_0^*) = (0, 0)$  is unstable on  $M$  since  $A < 0$ . □

### 2.2.3 Dynamics on Branch II

Finally, we analyze the unstable branch II. If  $A > 0$ , this branch can also have at most two equilibria, and it is possible to have no equilibria as well. The equilibrium  $(u_3^*, v_3^*) = (A, 0)$  can exist on this branch. If (2.27) holds, then  $(u_4^*, v_4^*) = (0, v_-)$  can exist on this branch where  $v_-$  is defined in (2.36). It is possible to have these equilibria exist simultaneously on branch II, or have one or neither. In Figure 2.2 (a), we see that on the pink manifold  $M$ , branch II has two equilibria. Notice that in this case  $k_- < A$ . Now, as  $k_-$  shifts to the right, the equilibria gradually disappear from branch II, and the blue manifold  $M$  shows a case when branch II has no equilibria. We summarize the equilibria stability in a lemma.

**Lemma 2.2.5.** (*Equilibria Stability on Branch II, Strong Allee Effect,  $A > 0$* ) Suppose that  $A > 0$  and that  $(u_4^*, v_4^*) = (0, v_-)$  where  $v_-$  is defined by (2.36) and  $(u_3^*, v_3^*) = (A, 0)$  are not non hyperbolic points. On branch II, if (2.27) holds, then  $(u_4^*, v_4^*) = (0, v_-)$  can exist on branch II and is always unstable on  $M$ . If  $k_- < A < k_+$  then  $(u_3^*, v_3^*) = (A, 0)$  exists and is stable on branch II.

*Proof.* By the same calculation as in Lemma 2.2.4 we see that  $(u_4^*, v_4^*)$  is always unstable on branch II. It also follows that  $(u_3^*, v_3^*) = (A, 0)$  exists on branch II if  $k_- < A < k_+$ , by definition of  $M$  in (2.20). Further,  $(u_3^*, v_3^*)$  is always stable on this branch which follows from (2.35) in the proof of Lemma 2.2.3 because of the condition  $k_- < A$  making  $v'(u) - 1 < 0$  by Lemma 2.2.1 item *ii*).  $\square$

Now, we discuss the case when  $A < 0$ . In this case, the possible equilibria on branch II are  $(u_4^*, v_4^*) = (0, v_-)$  with  $v_-$  defined by (2.36) and  $(u_0^*, v_0^*) = (0, 0)$ . In Figure 2.2, we see that on the pink manifold, branch II has  $(u_0^*, v_0^*) = (0, 0)$ . Notice that for this case  $k_- < 0$ . Now as  $k_-$  gets shifted, branch II in the blue manifold has one equilibrium now at  $(u_4^*, v_4^*) = (0, v_-)$ , and in this case  $k_- > 0$ . It is also possible to have no equilibria on the branch II, like in Figure 2.2 (a). We summarize the stabilities of these equilibria in a lemma.

**Lemma 2.2.6.** (*Equilibria Stability on Branch II, Weak Allee Effect,  $A < 0$* ) Suppose that  $A < 0$  and that  $(u_4^*, v_4^*) = (0, v_-)$  where  $v_-$  is defined by (2.36) and  $(u_0^*, v_0^*) = (0, 0)$  are not non hyperbolic points. On branch II, if (2.27) holds, then  $(u_4^*, v_4^*) = (0, v_-)$  can exist on branch II and is always unstable. If  $(u_0^*, v_0^*) = (0, 0)$  exists on branch II, it is unstable.

*Proof.* By the same calculation as in Lemma 2.2.4 we see that  $(u_4^*, v_4^*)$  is always unstable on  $M$ . It also follows that  $(u_0^*, v_0^*) = (0, 0)$  is always unstable on branch II from the a calculation in Lemma 2.2.3.  $\square$

## 2.2.4 Summary of Dynamics on $M$

The full dynamics when  $A > 0$  and  $M$  has three branches ( $d > 0$ ) is summarized in Figure 2.3. Figure 2.3 combines the fast dynamics we have seen before, and the dynamics on the slow manifold. The non hyperbolic points are denoted with the open white circles and the equilibria are denoted by the black circles. The manifold is in pink and some trajectories are shown in blue. The arrows in black help show the direction of flow. The plots (a), (b), (c) in Figure 2.3 show the cases when  $k_- < A$ ,  $k_- = A$ , and  $k_- > A$ , respectively. Notice that in case (a), the equilibrium  $(u_3^*, v_3^*) = (A, 0)$  is stable but in case (c) it is unstable as shown in the above analysis. Case (b) shows a special case when all the non hyperbolic points coincide with equilibria. That is, the equilibria  $(u_3^*, v_3^*) = (A, 0)$  and  $(u_2^*, v_2^*) = (u_4^*, v_4^*)$  are the non hyperbolic points. We note that it is possible to have  $(u_3^*, v_3^*)$  coincide with a non hyperbolic point and have the two equilibria  $(u_2^*, v_2^*) = (0, v_+)$  and  $(u_4^*, v_4^*) = (0, v_-)$  exist.

Figure 2.4 summarizes the cases when there are 3 branches and  $A \leq 0$ . In (a) and (b) the case when  $k_- < 0$  and  $k_- > 0$  are shown, respectively. In (c), the case when  $(u_2^*, v_2^*) = (u, v_+)$  and  $(u_4^*, v_4^*) = (u, v_-)$  coincide with the non hyperbolic point is shown.

The other case we have when  $A > 0$  is where there are two attractive branches I, III and the repelling branch II degenerates into a single non hyperbolic point, that is  $d = 0$ . This case occurs when  $k_+ = k_-$  and we only have 3 equilibrium points since  $M$  in (2.20)

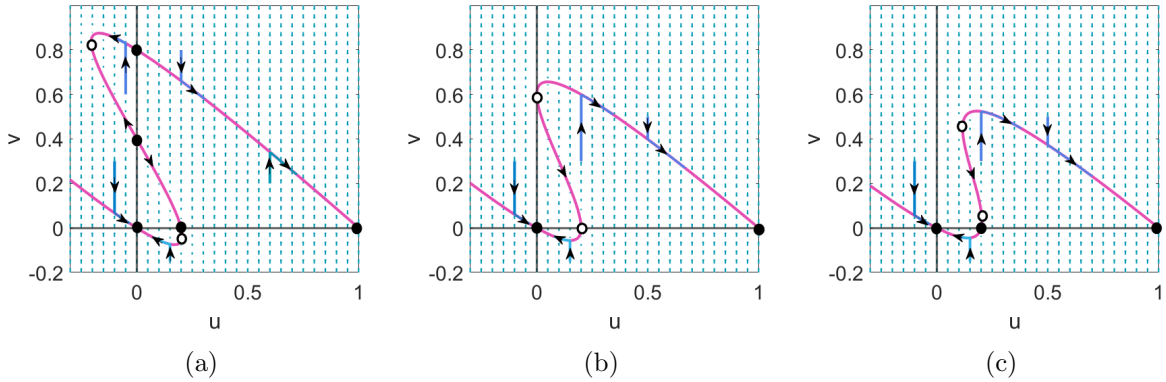


Figure 2.3: Phase portraits of (2.1) when  $A > 0$  with  $\delta = 0.001$ . The curve in pink is the manifold comprised on branches separated by a non hyperbolic point(s) (white circle). The equilibria are denoted by black circles. The lines in blue illustrate the flow of the solutions at various initial conditions. In (a)  $a = 0.12$  and  $A = 0.2$ , in (b)  $a = 0.16$  and  $A = 0.2$ , and in (c)  $a = 0.20$  and  $A = 0.2$ .

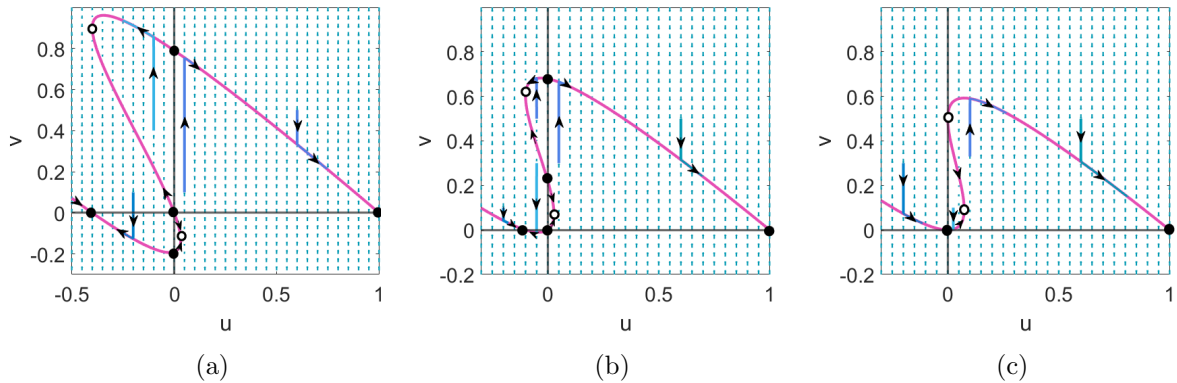


Figure 2.4: Phase portraits of (2.1) with  $A \leq 0$  and  $\delta = 0.001$ . The curve in pink is the manifold comprised on branches separated by a non hyperbolic point(s) (white circle). The equilibria are denoted by black circles. The lines in blue illustrate the flow of the solutions at various initial conditions. In (a)  $a = 0.25$  and  $A = -0.4$ , in (b)  $a = 0.25$  and  $A = -0.1$  and in (c)  $a = 0.25$  and  $A = 0$ . In (c),  $(0, v_{\pm})$  degenerate into a non hyperbolic point and  $(A, 0)$  and  $(0, 0)$  are the same equilibrium.

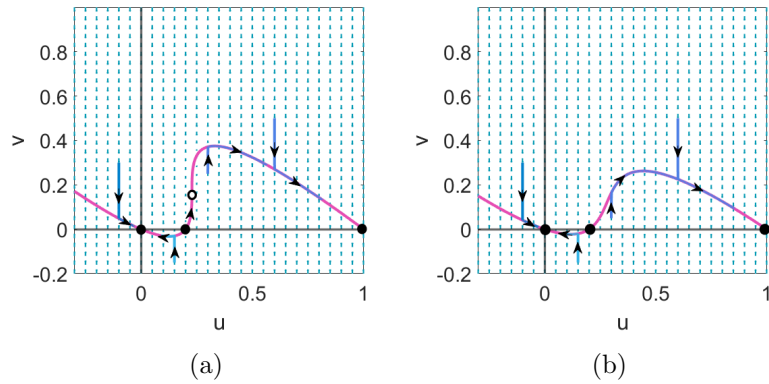


Figure 2.5: Phase portrait of (2.1) with  $A > 0$  and  $\delta = 0.001$ . The curve in pink is the manifold comprised on branches separated by a non hyperbolic point(s) (white circle). The equilibria are denoted by black circles. The lines in blue illustrate the flow of the solutions at various initial conditions. In (a)  $a = 0.28$  and  $A = 0.2$  yielding one non hyperbolic point. In (b)  $a = 0.4$  and  $A = 0.2$  yielding only one attractive branch.

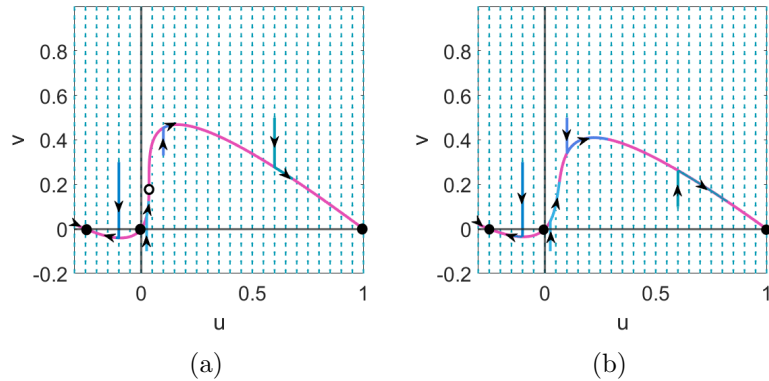


Figure 2.6: Phase portrait of (2.1) with  $A \leq 0$  and  $\delta = 0.001$ . The curve in pink is the manifold comprised on branches separated by a non hyperbolic point(s) (white circle). The equilibria are denoted by black circles. The lines in blue illustrate the flow of the solutions at various initial conditions. In (a)  $a = 0.4375$  and  $A = -0.25$  yielding two branches. In (b)  $a = 0.5$  and  $A = -0.25$  yielding one branch.

can intersect the  $v$ -axis at most once. The dynamics for this case are summarized in Figure 2.5 (a).

In the case of the weak Allee effect,  $A \leq 0$ , it is also possible to have the repelling branch II degenerate into a non hyperbolic point, with two attracting branches I, III remaining. There are also only three equilibria in this case and the dynamics are summarized in Figure 2.6 (a).

Finally, we analyze the case for when there is only one normally hyperbolic attractive branch, that is  $d < 0$ . This is a special case when branch I and III “merge” and become one normally hyperbolic branch, which we call branch I. The dynamics are very similar to the above cases with 2 attractive branches and one non hyperbolic point. The dynamics of this case when  $A > 0$  are summarized in Figure 2.5 (b) and what occurs for a similar case when  $A < 0$  is shown in Figure 2.6 (b).

Now we consider the case when  $A = 0$ . The general dynamics for the weak Allee effect hold as outlined above. The key difference is that  $(u_0^*, v_0^*) = (0, 0)$  and  $(u_3^*, v_3^*) = (A, 0)$  degenerate into one equilibrium at  $(u_0^*, v_0^*) = (0, 0)$ , and we cannot comment on its stability from the analytical calculations. We can illustrate the dynamics numerically as shown in Figure 2.4 (c). Numerically, it appears that in this case the equilibrium at  $(u_0^*, v_0^*) = (0, 0)$  has one sided stability.

Notice that from the numerical examples shown in Figures 2.3 and 2.5,  $A$  remains fixed and  $a$  varies. We see that with increasing  $a$  the manifold  $M$  eventually becomes normally hyperbolic everywhere, for sufficiently large  $a$ . Similarly, if  $a$  is fixed and  $A$  increases, then manifold  $M$  becomes normally hyperbolic for sufficiently large  $A$  as shown Figure 2.4.

## 2.2.5 Behaviour at Non Hyperbolic Points

We discuss now about what occurs at the non hyperbolic points. The behaviour is summarized in Figure 2.7. In (a), if we follow the dark blue trajectory, we see it quickly converges to the unstable branch I, and then flows to the left towards the non

hyperbolic point. As it reaches it, the trajectory “falls off” or jumps down converging to the stable branch III. From there it flows toward the stable equilibrium. Likewise, in the light blue trajectory in (a), the solution converges to the stable branch III, and flows toward the other non hyperbolic point. Once the trajectory reaches the non hyperbolic point it jumps up to the stable branch I, converging toward the stable equilibrium at  $(u, v) = (1, 0)$ . The jump in (b) of the light blue trajectory is more subtle, yet still occurs. This shows that when the trajectory reaches the non hyperbolic point, it will quickly jump towards the other stable branch. During the jump, the trajectory will have dynamics of the fast system (2.2), and once the trajectory has settled onto the slow manifold, it will exhibit the dynamics of the slow system (2.25).

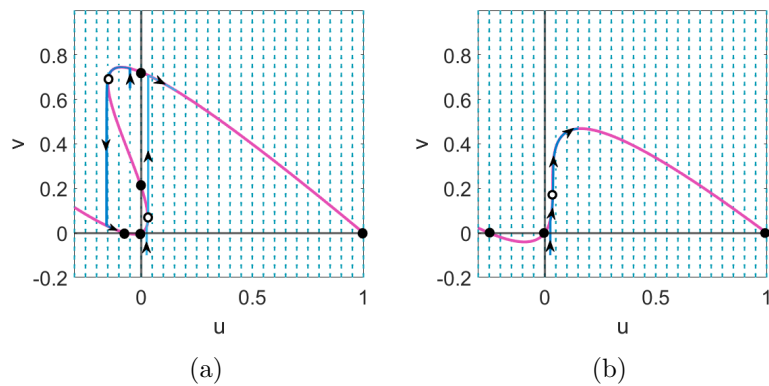


Figure 2.7: Phase portrait of (2.1) with  $A < 0$  and  $\delta = 0.001$  illustrating the behaviour at the non hyperbolic points. The curve in pink is the manifold comprised on branches separated by a non hyperbolic point(s) (white circle). The equilibria are denoted by black circles. The lines in blue illustrate the flow of the solutions at various initial conditions. In (a)  $a = 0.22$  and  $A = -0.07$  and in (b)  $a = 0.4375$  and  $A = -0.25$ .

## 2.3 Allee Region

We have now fully analyzed model (2.1) which incorporates the Allee effect. Recall that  $u$  denoted the CSC density and  $v$  the TC density. Since the densities are normalized in (2.1), the carrying capacity  $K = 1$ . Hence, the biologically relevant domain is given

by the triangle

$$\Delta = \{(u, v) : 0 \leq u \leq 1, 0 \leq v \leq 1, u + v \leq 1\} \quad (2.37)$$

since by assumption tumors start growth below carrying capacity, that is  $u + v = n \leq 1$ .

In Figure 2.3, we notice an interesting region within  $\Delta$  where tumors naturally decay. This region is highlighted in green for case (b) of Figure 2.3, in Figure 2.8 where the black diagonal and the positive parts of  $u$  and  $v$  axes enclose  $\Delta$ . We call the green region the *Allee region*.

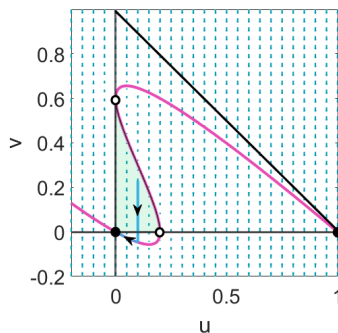


Figure 2.8: Phase portrait of (2.1) with  $A > 0.2$ ,  $a = 0.16$ , and  $\delta = 0.001$ . The curve in pink is the manifold comprised on branches separated by a non hyperbolic point(s) (white circle). The equilibria are denoted by black circles and the black diagonal marks when  $n = 1$ . The line in blue illustrates an example trajectory. Trajectories within the highlighted green region converge to the origin.

**Definition 2.3.1.** (*Allee region*  $\Lambda$ ) A region  $\Lambda \subset \Delta$  where TC or CSC densities decrease naturally, is called the *Allee region*. A key characteristic of this region is at least one density dies out completely.

For the cases illustrated in Figures 2.3 and 2.5, the Allee region can also be characterized by the intersection of the basin of attraction of  $(u_0^*, v_0^*) = (0, 0)$  and quadrant I. We provide a more general definition above to incorporate more general cases, which do not require the existence of a stable steady state at the origin. We also want to quantify the size of the Allee region, which we do by calculating the relative area to  $\Delta$  and we call the resulting value the *Allee index*.

**Definition 2.3.2.** (*Allee index  $\sigma$* ) The *Allee index*,  $\sigma$ , is the measure of the relative area of the Allee region  $\Lambda$  to the area of the biologically relevant region  $\Delta$ . To calculate the Allee index, let  $\omega$  be the area of  $\Lambda$ , and  $T$  be the area of the domain  $\Delta$ , then

$$\text{Allee index} = \sigma = \frac{\omega}{T} = 2\omega. \quad (2.38)$$

since  $T = 1/2$ . If  $\sigma = 1$ , then the whole domain is the Allee region.

Figure 2.8 illustrates a flaw of model (2.1), which is that the trajectories escape the Allee region and the TC density becomes negative. In a biologically realistic model, densities should not become negative, if they begin within the biologically relevant domain  $\Delta$ . We address this issue in Chapter 3, by modifying the model (2.1) and study how to increase the Allee region.

## Chapter 3

# Biologically Relevant Cancer Stem Cell Model with an Allee Effect

In the previous chapter, we analyzed the model (2.1) in detail. As remarked before, that model is not biologically realistic as some trajectories may flow below the  $u$ -axis even when the initial condition is contained within the biologically relevant region  $\Delta$  defined by (2.37). This can give negative densities which should not happen in a biologically relevant model. In this section, we fix this issue and propose a closely related model to (2.1) that is biologically relevant. We will then analyze the modified model, where we benefit greatly from the detailed analysis in Chapter 2.

We propose the following modified model

$$\begin{aligned} \dot{u} &= \delta F^+(n)u, \\ \dot{v} &= (1 - \delta)F^+(n)u + F(n)v - av, \end{aligned} \tag{3.1}$$

where

$$F^+(n) = \max(F(n), 0) = \begin{cases} F(n) & \text{if } F(n) > 0, \\ 0 & \text{otherwise.} \end{cases} \tag{3.2}$$

Notice that the only difference between the previously studied model (2.1) and the current one (3.1) is the introduction of  $F^+(n)$  which is done so that the CSC growth

term remains non-negative. Hence, the interpretation of the terms and the dynamics in the phase space are almost the same as before. Here, we highlight the differences. Like before,  $F(n) = (1 - n)(n - A)$  where  $A$  is the Allee constant,  $|A| < 1$  and  $n = u + v$ . Recall the biological interpretation of  $F(n)$ , which is that it is a function describing the cells fitness to reproduce in a certain location. Hence, if  $F(n)$  is positive this corresponds to a favourable region and cells grow, and if  $F(n)$  is negative cells decay due to a limitation of space and nutrients. For  $F^+(n)$ , we take the positive parts of  $F(n)$  and connect them with a constant zero function, as defined in (3.2). Notice, that the terms describing contributions from the CSCs have  $F^+(n)$  whereas the terms describing contributions from the TCs have  $F(n)$ . Let's examine the term  $F(n)v$  first in the second equation of (3.1). When  $F(n)$  is positive,  $F(n)v$  contributes positively to the overall TC density, meaning that the environment is favourable and TCs are able to replicate. When  $F(n)$  is negative,  $F(n)v$  contributes negatively to the overall TC density, meaning that TCs die due to being in an unfavourable environment. Now, CSCs can only contribute positively and they do not kill TCs. Hence, the term  $(1 - \delta)F^+(n)u$  is either positive or zero, fixing the issue that model (2.1) had.

Next, we show that (3.1) is a dynamical system.

**Lemma 3.0.1.** *Together with an initial condition  $(u(0), v(0)) = (\bar{u}, \bar{v})$ ,  $\bar{u}, \bar{v} \in \mathbb{R}$ , (3.1) forms a dynamical system in  $\mathbb{R}^2$ .*

*Proof.* It is enough to show that  $F^+(n)$  in (3.2) is locally Lipschitz continuous. The rest follows from the Picard–Lindelöf Theorem 2.0.1 like in the proof of Lemma 2.0.2.

Because  $F(n) = (1 - n)(n - A)$  and constant functions are Lipschitz continuous (follows from Mean Value Theorem), it is enough to show that for arbitrary functions  $n(x), m(x)$ ,  $x \in \mathbb{R}^2$  which are both locally Lipschitz,  $h(x) = \max(n(x), m(x))$  is also locally Lipschitz.

Since  $n(x)$  is locally Lipschitz,  $|n(x) - n(y)| \leq L_1|x - y|$  where  $y \in \mathbb{R}^2$  and  $L_1$

depends on  $x$  and  $y$ . So the right inequality of

$$-L_1|x - y| \leq n(x) - n(y) \leq L_1|x - y| \quad (3.3)$$

implies

$$n(x) \leq n(y) + L_1|x - y| \leq h(y) + L_1|x - y|. \quad (3.4)$$

Similarly,

$$m(x) \leq m(y) + L_2|x - y| \leq h(y) + L_2|x - y|. \quad (3.5)$$

where  $L_2$  depends on  $x, y$ . From (3.4) and (3.5) it follows that

$$h(x) \leq h(y) + L|x - y| \quad (3.6)$$

where  $L = \max(L_1, L_2)$ .

The left inequality of (3.3) implies

$$n(y) \leq n(x) + L_1|x - y| \leq h(x) + L_1|x - y|. \quad (3.7)$$

Similarly,

$$m(y) \leq m(x) + L_1|x - y| \leq h(x) + L_1|x - y|. \quad (3.8)$$

Together, (3.7) and (3.8) imply that

$$h(y) \leq h(x) + L|x - y| \quad (3.9)$$

where  $L = \max(L_1, L_2)$ . Combining (3.6) and (3.9) yields that

$$|h(x) - h(y)| \leq L|x - y|. \quad (3.10)$$

Hence,  $h(x)$  is locally Lipschitz continuous.  $\square$

We also find that the biologically relevant domain  $\Delta$  given by (2.37) in system (3.1)

is positively invariant.

**Lemma 3.0.2.** *(Positively Invariant Region  $\Delta$ ) System (3.1) has a positively invariant region  $\Delta$  defined in (2.37).*

*Proof.* To show  $\Delta$  is positively invariant, it is enough to look at the vector field on the boundaries:  $u = 0$ ,  $v \in [0, 1]$ ,  $u + v = 1$ , and  $v = 0$ ,  $u \in [0, 1]$ . When  $u = 0$  we see from (3.1) that the vectors only flow up or down. Hence, when  $u = 0$ ,  $v = 1$  the flow is downward and when  $u = 0$ ,  $v = 0$  there is a steady state. When  $u + v = 1$ , all vectors flow down, where there is a steady state at  $u = 1$ ,  $v = 0$ . Now when  $v = 0$ , if  $u > A$  then  $\dot{u}, \dot{v} \geq 0$  and when  $u \leq A$  then  $\dot{u}, \dot{v} = 0$ . This shows that the triangle is positively invariant, since no vectors leave  $\Delta$ .  $\square$

It is enough to analyze (3.1) in  $\Delta$  since on the boundary  $u + v = 1$  the tumor is at its carrying capacity density. By assumption, no tumor starts off at a density larger than the carrying capacity density, so our biologically relevant domain is now  $\Delta$ .

### 3.1 Fast System

We analyze (3.1) in a similar manner as (2.1) in Chapter 2 by first looking at the fast system. Again, taking  $\delta \rightarrow 0$  yields

$$\begin{aligned}\dot{u} &= 0, \\ \dot{v} &= F^+(n)u + F(n)v - av.\end{aligned}\tag{3.11}$$

The nullcline from the second equation of (3.11) gives the manifold

$$\bar{M} := \{(u, v) : 0 = F^+(n)u + F(n)v - av, n = u + v\}.\tag{3.12}$$

which can be rewritten as

$$\bar{M} = \begin{cases} 0 = F(n)v - av & \text{if } n < A, \\ 0 = F^+(n)u + F(n)v - av & \text{if } n \geq A. \end{cases} \quad (3.13)$$

Notice that for  $n \geq A$   $\bar{M} = M$  with  $M$  defined by (2.20). Hence, all of the previous results from model (2.1) hold under this constraint. Further, if  $A < 0$  then  $F(n) \geq 0$  in  $\Delta$ . Hence, we only need to examine what occurs when  $0 < n < A$ ,  $A > 0$ .

When  $n < A$  and  $A > 0$

$$\dot{v} = (F(n) - a)v := s(u, v). \quad (3.14)$$

Using (3.14), we show that  $\bar{M}$  is normally hyperbolic and attracting when  $n < A$ . Calculating the derivative of  $s(u, v)$  with respect to  $v$ , we obtain

$$\left. \frac{\partial s}{\partial v} \right|_M = F'(n)v + F(n) - a. \quad (3.15)$$

Notice that  $s(u, v) = 0$  implies that  $v = 0$  when  $n < A$ , since  $F(n) < 0$ . So (3.15) reduces to

$$\left. \frac{\partial s}{\partial v} \right|_M = F(n) - a, \quad (3.16)$$

which shows that  $\left. \frac{\partial s}{\partial v} \right|_M < 0$ , when  $n < A$ . This proves that  $\bar{M}$  is normally hyperbolic and attracting when  $n < A$ ,  $A > 0$ .

We can express  $\bar{M}$  into branches as follows

$$\bar{M} := \begin{cases} \text{I: } 0 = F^+(n)u + F(n)v - av, n > k_+ \\ \text{II: } 0 = F^+(n)u + F(n)v - av, k_- < n < k_+, n \geq A \\ \text{III: } 0 = F^+(n)u + F(n)v - av, A \leq n < k_- \cup 0 = F(n)v - av, n \leq A \end{cases} \cup N_+ \quad (3.17)$$

where  $k_{\pm}$  is defined in (2.10) and

$$N_+ = \{(u_{nh}, v_{nh}) : v_{nh^+}, v_{nh^-} \geq 0\}, \quad (3.18)$$

that is  $N_+$  is the set of non hyperbolic points with non negative  $v$ -coordinate. Essentially, the difference between  $M$  and  $\bar{M}$  is that in the regions when  $M$  falls into quadrants III and IV of the  $uv$ -plane,  $\bar{M}$  has a horizontal interval at  $v = 0$  connecting continuously to the other positive branches. Moreover, we are only interested in the parts of  $\bar{M}$  that fall within  $\Delta$ .

To summarize, we show some possible cases in Figure 3.1. We focus on when  $A > 0$  since when  $A \leq 0$ , the behaviour of system (3.1) is the same as system (2.1) in  $\Delta$ . Like before, the manifold  $\bar{M}$  is in pink in each case, the trajectories are in blue, and the non hyperbolic points are the open white circles. The black diagonal line shows the boundary of  $\Delta$ . In (a), the case where there are three branches is shown. We see that the unstable branch II meets the stable branch III at  $A$  and branches II and I are not connected in  $\Delta$ . In (b), the case when branch II degenerates into a non hyperbolic point is shown. This case shows how the positive part of  $F(n)$  meets  $s(u, v) = 0$  at  $A$ , creating the attracting branch III. Finally, we have the case where  $\bar{M}$  is a single branch in (c) where again we have the connection of the positive part of  $F(n)$  with  $s(u, v) = 0$  forming a single attracting branch.

We highlight the Allee region  $\Lambda$  in green in Figure 3.1. We see that if a trajectory starts in the Allee region  $\Lambda$ , the flow is downward until the  $u$ -axis is reached. So if

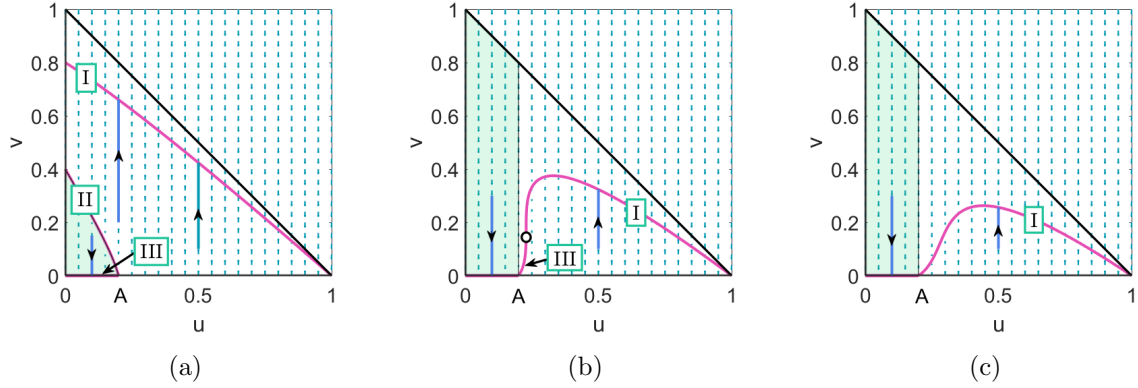


Figure 3.1: Phase portraits of (3.11). In each figure, the curve in pink is the manifold  $\bar{M}$  where the non hyperbolic points are denoted by open white circles. The lines in blue are the flows of the solutions which either flow up or down. The branches are labeled by their respective numbers. The position of the parameter  $A$  is also labelled, where  $A = 0.2$  for each case. The Allee region,  $\Lambda$ , is highlighted in green. In (a)  $a = 0.12$  yielding three branches and the Allee index  $\sigma = 0.0866$ . In (b)  $a = 0.28$  yielding two attracting branches and  $\sigma = 0.36$ . In (c),  $a = 0.4$  yielding one attracting branch and  $\sigma = 0.36$ .

the cancer starts out with CSC and TC densities contained within  $\Lambda$ , the TCs die out naturally, decreasing the overall size of the tumor. Hence, in  $\Lambda$  it is possible to achieve tumor control, as no tumor growth occurs.

In Figure 3.1, the Allee Indices in (a), (b) and (c) are  $\sigma = 0.0866$ ,  $\sigma = 0.36$ , and  $\sigma = 0.36$ , respectively. So we see that as  $a$  increases and  $A$  remains fixed, the Allee index,  $\sigma$ , increases up to a point and remains fixed regardless of how large  $a$  is. Hence,  $\sigma$  is limited by the value of  $A$ . If  $A$  increases then  $\sigma$  also increases, and the increase in the  $\sigma$  is much more drastic.

## 3.2 Slow System

We now examine the slow system of (3.1) which is obtained by rescaling time using  $\tau = \delta t$  and taking  $\delta \rightarrow 0$  giving

$$\begin{aligned} u' &= F^+(n)u, \\ 0 &= F^+(n)u + F(n)v - av. \end{aligned} \tag{3.19}$$

All five equilibria discussed for the model (2.1) are present in the above model. If the equilibria fall on the positive part of  $F(n)$ , then the dynamics discussed for (2.1) remain the same as well. The key difference is that when  $A > 0$ , we have a continuum of steady states on the segment  $v = 0$  and  $u \in [0, A)$  because  $u' = 0$ . This means that if the flow converges to the piece of  $\bar{M}$  defined by  $s(u, v)$  (3.14), it stays at that point for all time unable to increase or decrease in  $u$ .

The examples shown in Figures 2.3, 2.4, 2.5, 2.6, 2.7 summarize the dynamics of (3.1) if restricted to  $\Delta$ . Notice that the Allee region,  $\Lambda$ , is the region enclosed by branch II, branch III and  $u = 0$ . From these examples, we see that if a tumor starts growing in the Allee region, the TC density decreases but the CSC density remains constant. That means the CSCs go quiescent unable to cause the tumor to grow. If the tumor starts growing outside of  $\Lambda$ , then the tumor will select for CSCs, until a tumor comprised of only CSCs is obtained. This is because the trajectories outside of  $\Lambda$  converge to the steady state  $(u_1^*, v_1^*) = (1, 0)$ .

To finish this section, we remark that when  $A \leq 0$ , there is no Allee region  $\Lambda$ . This is because if the trajectory starts anywhere within  $\Delta$ , it will converge to the manifold and eventually reach the equilibrium  $(u_1^*, v_1^*) = (1, 0)$ , as shown in Figures 2.4, 2.6, 2.7. Hence, no matter what size the tumor is, if  $A \leq 0$  the tumor grows and eventually becomes comprised of only CSCs.

### 3.2.1 Remarks

Before moving on to study what happens if we include treatment to (3.1), we would like to mention what would occur if  $F(n)$  was used in the first equation of system (3.1) instead of  $F^+(n)$ . In that case, the CSCs can die due to the Allee effect, since when  $n < A$  the first equation of (3.1) is negative. This yields dynamics on branch III in the region of  $n < A$ , instead of a continuum of steady states. Hence, the flows that converged to branch III, in the region  $n < A$ , would flow towards the steady state at the origin since it is stable. Everything else outside of the region  $n < A$  remains the

same. Thus, if CSCs are affected by the Allee effect, the tumor becomes extinct if it is in the Allee region.

### 3.3 Cancer Stem Cell Model with Allee Effect and Treatment

Now that we have established that (3.1) is biologically relevant, we incorporate treatment into this model. As before,  $u(t)$  and  $v(t)$  denote the CSC and TC densities, respectively. To incorporate treatment into the model, we need to include a function that will model the kill rate which will depend on the type of treatment. We also need account for the latency time effect which occurs because cancer cells take time to die and get cleared from the tissue [49, 66]. This can be accounted for mathematically by having a damaged cell compartment  $w(t)$ . In this damaged compartment all cells eventually die, as we assume that the damaged cells are focused on repair and cannot produce offspring. Further, we assume that the damaged cells are focused on repair and thus do not produce offspring. By adding treatment and the latency time effect into (3.1), we obtain the modified model

$$\begin{aligned}\dot{u} &= \delta F^+(n)u - \eta\delta H(t)u \\ \dot{v} &= (1 - \delta)F^+(n)u + F(n)v - av - H(t)v, \\ \dot{w} &= \eta\delta H(t)u + H(t)v - \gamma w,\end{aligned}\tag{3.20}$$

where  $n(t) = u(t) + v(t) + w(t)$ . The parameter  $\delta$  is the fraction of symmetric divisions,  $a$  is the death rate of TCs, and  $A$  is Allee constant as before. Here,  $H(t)$  is a function modelling the kill rate from treatment which depends on time. Hence, when treatment is applied  $H(t) \neq 0$  but when treatment stops  $H(t) = 0$ . Since  $H(t)$  models the kill rate from treatment, it can represent a generic cytotoxic treatment. We assume for simplicity that because CSCs have low treatment sensitivity, the kill rate of CSCs from treatment is on the same scale as  $\delta$ . Therefore, the treatment function in the CSC

compartment is multiplied by  $\delta$ . We also multiply the function by  $0 \leq \eta \leq 1$  which is a parameter accounting for various treatment resistances that CSCs have. The cells affected by treatment become damaged and join the damaged volume compartment. The first two terms in the third equation of (3.20) model the amount of damaged volume resulting from treatment. Since damaged cells can only die, the third term describes the clearance of the damaged volume with clearance rate  $\gamma$ .

System (3.20) is much more difficult to analyze analytically. Here, we write down the fast reduced system to get an idea of what the slow manifolds look like, and plot them numerically. The fast reduced system of (3.20) is

$$\begin{aligned} \dot{u} &= 0, \\ \dot{v} &= F^+(n)u + F(n)v - av - H(t)v, \\ \dot{w} &= H(t)v - \gamma w. \end{aligned} \tag{3.21}$$

To analyze the fast system, we assume for now that the treatment term  $H(t)$  is constant. If  $H > 0$  then the treatment is on and if  $H = 0$  then the treatment is off. We see that (3.21) has two manifolds which are given by

$$M_1 = \{(u, v, w) : F^+(n)u + F(n)v - av - Hv = 0, u + v + w \leq 1\}, \tag{3.22}$$

and

$$M_2 = \{(u, v, w) : Hv - \gamma w, u + v + w \leq 1\}. \tag{3.23}$$

We represent the intersection of the two manifolds by

$$M_1 \cap M_2 = M_T, \tag{3.24}$$

where for all  $H > 0$  we call  $M_T$  the treatment manifold. An example as to how these manifolds can look like is given in Figure 3.2 (a). The manifold  $M_1$  is shown by the blue surface and  $M_2$  is given by the pink surface. The two manifolds intersect giving

the pink curve  $M_T$ . The blue curve in the  $uv$ -plane is the no treatment manifold  $\bar{M}$  defined in (3.12) which is from the two dimensional system (3.1). This blue curve is shown for comparison.

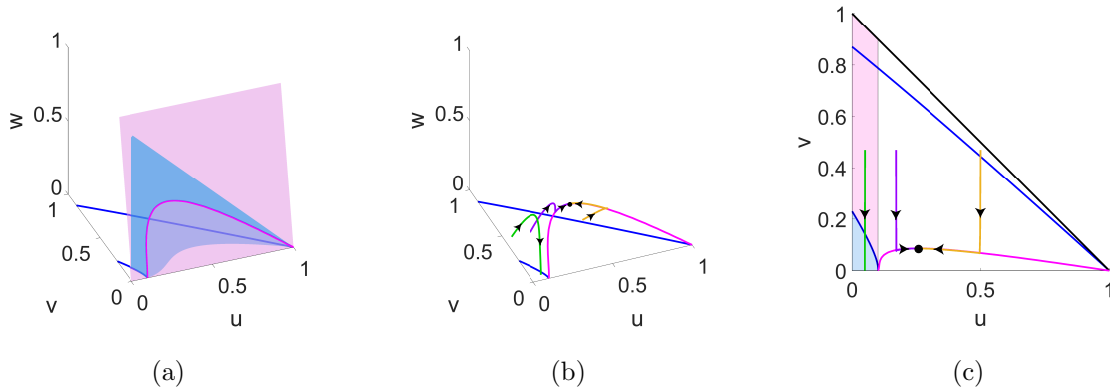


Figure 3.2: In all cases  $H(t) = 0.5$ ,  $\eta = 0.3$ ,  $\delta = 0.01$ , and  $a, A, \gamma = 0.1$ . In (a), the blue surface is  $M_1$ , the pink surface is  $M_2$ , and the pink curve is the treatment manifold  $M_T$ . The blue curve is the no treatment manifold  $\bar{M}$  defined in (3.12). In (b), the blue and pink curves are still  $\bar{M}$  and  $M_T$ , respectively. The curves in green, purple and yellow are example trajectories of (3.20). The equilibrium is denoted by a black circle. The plot in (c) shows the top view of (b) where the black diagonal line represents  $u + v = 1$ . The shaded area in blue is the Allee region of (3.1) and the shaded area in pink plus the shaded area in blue is the Allee region for (3.20).

Now, the slow reduced system of (3.20) is given by

$$\begin{aligned}
 u' &= F^+(n)u - \eta Hu, \\
 0 &= F^+(n)u + F(n)v - av - Hv, \\
 0 &= \eta\delta Hu + Hv - \gamma w.
 \end{aligned}
 \tag{3.25}$$

It is difficult to solve for equilibria explicitly, so we show what occurs numerically in Figure 3.2 (b). In (b), the pink curve is still  $M_T$ , and the blue curve is still  $\bar{M}$  defined in (3.12). In green, purple, and yellow are some example trajectories and  $H(t)$  is constant. We see that for the green trajectory  $v$  always decreases,  $u$  remains constant, and  $w$  increases at first but then decreases. The purple and yellow trajectories converge to  $M_T$  and then grow along it. For the example parameters we chose, there is a stable

steady state to which the two trajectories converge to. This is seen more clearly in Figure (3.2) (c) which shows the top view of (b). The area shaded with blue is the Allee region of (3.1) which is what it would be without treatment. In pink is the additional region that becomes part of the Allee region during treatment. Hence, the areas shaded in blue and pink is the Allee region of (3.20) for the example parameters listed in Figure 3.2. Since the green trajectory falls within the new Allee region, the TC density decreases, but CSC density remains fixed. This is the case when tumor control is obtained. Without treatment, the green trajectory would have converged to the no treatment manifold  $\bar{M}$  (the blue curve) and the cancer would have progressed. However, with the same treatment but different initial starting densities, the trajectories in purple and yellow converge to a steady state on the treatment manifold  $M_T$  defined by (3.24). In this case, the growth of the tumor was halted since the trajectories converged to a steady state. However, once treatment stops ( $H = 0$ ), the cancer is expected to start growing since the purple and yellow trajectories will begin to converge to towards the no treatment manifold  $\bar{M}$ .

Notice that treatment does not influence the Allee constant  $A$ . This means that the maximum Allee region is preset and it can be predicted which trajectories are expected to attain tumor control given that  $A$  is known. In particular, this shows that cancers starting out with few CSCs and many TCs are more likely to end up in the extended Allee region during treatment, whereas cancers with many CSCs and few TCs are expected to persist.

### 3.3.1 Fractionated Treatment

Now we look at what occurs during a fractionated cytotoxic treatment. A fractionated treatment is when treatment is applied for a period of time followed by a break where there is no treatment given. The treatment is then applied again, followed by a break. This repeats until the required dose to a patient is given. An example of this type of treatment is radiotherapy [7, 23]. To illustrate the dynamics, we consider a very

prolonged treatment with long break periods in order to clearly see the behaviour. In particular, we study what a treatment is applied for 100 time units followed by a break of 100 time units. Further, we assume that during treatment application, the kill rate  $H$  is constant which is the typical assumption for fractionated treatments [23]. We see the response during fractionated treatment in Figure 3.3. For each plot in Figure 3.3 the green is the computed solution using Matlab ODE45, the pink curve is the treatment manifold  $M_T$  defined by (3.24), and the blue curve is the no treatment manifold  $\bar{M}$  defined in (3.12) like before. In Figure 3.3 (a), we see that the treatment successfully decreases the TC density and that during treatment the trajectory converges to  $M_T$  where CSC density begins to decrease. Once treatment is lifted, the TCs begin to repopulate and the trajectory converges to the blue curve  $\bar{M}$ . Once treatment is applied again, the trajectory converges to  $M_T$  again. In this case, due to the treatment, the equilibrium on  $M_T$  is towards the left of the initial condition, and the treatment generally decreases the CSC and TC densities. Note that in Figure 3.3 (a), the treatment has increased the Allee region and we get a similar situation as in Figure 3.2 (c). In Figure 3.3 (b), we see a worse treatment case where the treatment was also to push the equilibrium on  $M_T$  to the left. In this case, the treatment is able to lower the TC density but the CSC density increases with or without treatment. The Allee region also did not increase since the unstable branch of the treatment manifold  $M_T$  almost matches the unstable branch of the no treatment manifold  $\bar{M}$  meaning that the Allee regions are similar for both cases.

We conclude this section by summarizing the three cases that occur during treatment in system (3.20). The best case is when the tumor falls within the new Allee region during treatment. In this case, tumor control is guaranteed if the treatment is long enough. The second case is when the tumor does not fall within the Allee region, but the treatment is able to decrease the CSC and TC densities like was seen in Figure 3.3 (a). Tumor control in this case can only be achieved if the CSC and TC densities are pushed towards  $(u, v) = (A, 0)$  (a steady state of system (3.1)). The final case is when treatment is unsuccessful, and the CSC density increases during treatment as was seen

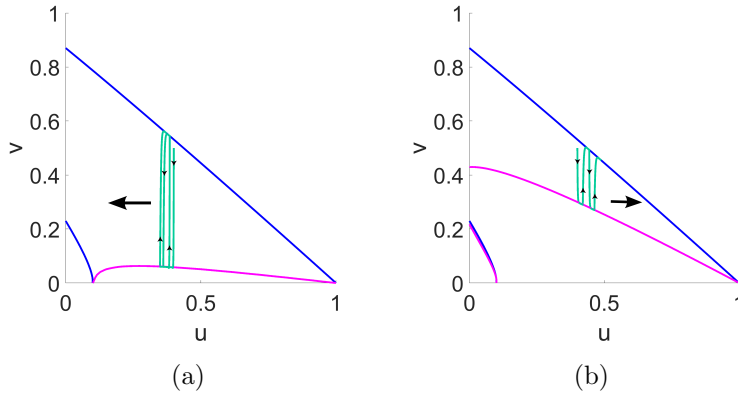


Figure 3.3: Examples of fractionated treatments 100 time units on, 100 time units off, for a total treatment period of 200 time units. In each figure, the green curve is the computed solution using Matlab ODE45, in pink the treatment manifold  $M_T$ , and in blue is the no treatment manifold  $\bar{M}$  defined in (3.12). In each figure  $\eta = 0.3$ ,  $\delta = 0.01$ , and  $a, A, \gamma = 0.1$ . In (a)  $H(t) = 0.7$  during the treatment period and the trajectory moves to the left. In (b)  $H = 0.07$  during the treatment period and the trajectory moves to the right. The initial condition is the same for both where  $u(0) = 0.4$  and  $v(0) = 0.5$

in Figure 3.3 (b).

Now that we understand the dynamics of (3.20) under a cytotoxic treatment, we move on to see if there are other ways to increase the Allee region and if a better treatment exists. In the next chapter, we find that by accounting for the feedback mechanisms present in cancer, there is a way to significantly increase the Allee region.

# Chapter 4

## Feedback Mechanisms and the Allee Effect

### 4.1 Introduction

Deregulation of signalling pathways plays a central role in cancer development [47]. There are a number of pathways that have been linked to influence CSC renewal such as the Wnt, Notch, and Sonic Hedgehog signalling pathways [2, 6, 47]. For example, upregulated Wnt signaling has been shown to increase the CSC population in colorectal cancer [47]. In the Wnt signalling pathway, stem cells maintain their population by secreting Wnt proteins, which stimulate self-renewal in stem cells [11, 47]. Stem cells can also release an inhibitor such as Dkk molecules, that suppress the Wnt proteins [11]. Additionally, differentiation promoters can be produced by differentiated cells [55]. In colorectal cancer, bone morphogenetic proteins (BMPs), which belong to the transforming growth factor- $\beta$  (TGF- $\beta$ ) family have been linked to stimulate CSCs to differentiate [47, 55]. Other members of the TGF- $\beta$  family, can also increase tumor invasiveness [50]. It has also been shown that as cancer progresses, more self-renewal promoters are released and sensitivity to growth inhibitors is lowered [29, 41, 38].

Previously, Konstorum et al. [38] showed that an Allee effect exists for a modified

system related to the model (1.4). Recall that model (1.4) was derived based on the probability of self-renewal,  $p$ . To show the Allee effect, Konstorum et al. [38] incorporated the feedback mechanism from the self-renewal promoters such as Wnts and from differentiation promoters such as BMPs. The self-renewal probability was modified to incorporate the concentration of self-renewal promoter  $c$  and the concentration of the differentiation promoter  $T$ . The amount of self-renewal inhibitors was assumed constant in [38]. However, competition between CSCs and TCs was not accounted for in [38]. In this section, we build upon (1.4) by introducing a competition function  $F(n)$  and TC dynamics and add a positive feedback mechanism relating to self-renewal activators. Our goal in this chapter is to study under which conditions on the self renewal probability,  $p$ , in the extended model (1.4), an Allee effect exists, if any.

## 4.2 Cancer Stem Cell Model Incorporating Feedback Mechanisms

We begin by adding a birth term from TCs, a death term for TCs, and a competition function  $F(n)$  to (1.4) where we set the growth rate  $k = 1$  for simplicity. This yields

$$\begin{aligned}\dot{u} &= (2p(c, T) - 1)F(n)u, \\ \dot{v} &= 2(1 - p(c, T))F(n)u + F(n)v - av,\end{aligned}\tag{4.1}$$

where the self-renewal probability  $p(c, T)$  depends on the self-renewal promoter concentration  $c$  and on the differentiation promoter  $T$ . The competition function  $F(n)$  satisfies assumptions F1 and F2 which were outlined in Section 1.1. In our analysis, we choose  $F(n) = 1 - n$ , which is the simplest function satisfying F1 and F2. Recall that if  $2p - 1 = \delta$  then (4.1) is fully equivalent to (1.7) by Lemma 1.1.1, hence the interpretation of the terms in (4.1) is the same as in (1.7) where  $u$  is the CSC density,  $v$  is the TC density,  $a$  is the TC death rate,  $n = u + v$ . The case for when  $p(c, T)$  is

fixed has been studied in [31] where they showed that

$$M_s = \{(u, v) : (1 - n)n - av, n = u + v\} \quad (4.2)$$

is an attracting slow manifold of (4.1) given that  $2p - 1 = \delta$  and  $p$  is fixed.

The explicit function for the self-renewal probability  $p(c, T)$  used in Konstorum et al. [38] was been proposed by Youssefpour et al. [70]. The probability function is given by

$$p(c, T) = p_{min} + (p_{max} - p_{min}) \left( \frac{\psi_1 c}{1 + \psi_1 c} \right) \left( \frac{1}{1 + \psi_2 T} \right) \quad (4.3)$$

where  $c$  is the concentration of CSC self-renewal promoters such as Wnts,  $T$  is the concentration of differentiation promoters such a BMPs. The parameters  $\psi_1$  and  $\psi_2$  are the feedback strengths on  $p$ . Notice that  $p$  in (4.3) generally increases when self-renewal activators,  $c$ , increase and decreases when differentiation promoters,  $T$ , increase. So if  $T$  is fixed in (4.3), then (4.3) is a saturating monotonically increasing function in  $c$ . If  $c$  is fixed then (4.3) is a monotonically decreasing function of  $T$ .

Here, we want to study how the concentration of self-renewal activators,  $c$ , affects tumor growth. Hence, we assume that  $T$  is constant. We also simplify (4.3) further, where we assume that  $c$  is directly proportional to the total tumor density,  $n$ . Hence, we set  $p(c, T) = p(n)$  so that the self-renewal probability depends on the total tumor density directly. The probability functions we will examine satisfy the following assumptions

P1.  $p(n) \geq 0$  is monotonically increasing and  $p(n) \in [0, 1]$ .

P2. There exist  $p_{min}, p_{max} \in [0, 1]$  such that  $p(0) = p_{min}$  and  $p(1) = p_{max}$ .

P3. There exists  $n^* \in [0, 1]$  such that  $p(n^*) = 0.5$ .

P4. If  $n < 0$  or  $n > 1$ ,  $p(n) = 0$ .

Assuming that  $p(n)$  is a monotonically increasing function means that as the tumor increases in size (meaning that cancer progresses), the amount of self-renewal promoters,

$c$ , increases, falling in line with what is observed experimentally [29, 41]. Here,  $n^*$  is a critical point between differentiation and self renewal. At  $n^*$ , the CSCs are able to sustain their population and produce TCs. If  $n < n^*$ , then  $p(n) < 0.5$  and from (4.1) we see that the term in the first equation is negative, meaning that CSCs are solely producing TCs, sacrificing themselves in the process. If  $n > n^*$ , then  $p(n) > 0.5$  and CSCs are focused on self renewal, producing more CSCs. So if  $n^*$  is large, it is harder for CSCs to self renew, and differentiation is favoured. This situation can occur if the differentiation promoters  $T$  are outweighing the self-renewal promoters  $c$ , hence decreasing  $p(n)$ .

Now, we replace  $p(c, T)$  by  $p(n)$  in (4.1) and obtain

$$\begin{aligned} \dot{u} &= (2p(n) - 1)(1 - n)u, \\ \dot{v} &= 2(1 - p(n))(1 - n)u + (1 - n)v - av. \end{aligned} \tag{4.4}$$

Additionally, if  $|2p(n) - 1| \ll 1$  then  $M_s$  defined in (4.2) is also a slow manifold of (4.4).

### 4.3 Linear Stability Analysis

We now show that there exists a positively invariant region which is a triangle enclosed by  $u = 0, v = 0, u + v = 1$ . This is exactly the region  $\triangle$  that was defined earlier in (2.37).

**Lemma 4.3.1.** *(Positively Invariant Region  $\triangle$ ) System (4.4) has a positively invariant region in  $D = \{(u, v) : u \in [0, 1], v \in [0, 1]\}$  which is the triangular region given by (2.37).*

*Proof.* We first look at the boundary  $u = 0$  and  $v \in [0, 1]$  then we see from (4.4) that the flows are either up or down, where the flow is down if  $v = 1$  and at  $v = 0$  there is an equilibrium. Hence, the flows do not escape this boundary. On the boundary  $u + v = 1$ , the flow is always down. Finally, on the boundary  $v = 0$  and  $u \in [0, 1]$ ,

$v_t > 0$  based on the assumptions on  $p(n)$ . Hence, no flows escape  $\Delta$  therefore it is positively invariant.  $\square$

The positively invariant region  $\Delta$  contains all of the essential dynamics, since all the equilibria are contained within this region, as we will now see. We find the equilibria by looking at the first equation of (4.4). It follows that in order to have equilibria either  $u = 0$ , or  $n = 1$ , or  $p(n) = 1/2$ . If  $u = 0$ , then from the second equation of (4.4) either  $v = 0$  or  $v = 1 - a$ . Hence, we obtain two equilibria  $(u_0^*, v_0^*) = (0, 0)$ ,  $(u_1^*, v_1^*) = (0, 1 - a)$ . If  $n = 1$  or equivalently  $u = 1 - v$ , we obtain from the second equation in (4.4) that  $v = 0$ . Hence,  $(u_2^*, v_2^*) = (1, 0)$ . If  $p(n) = 1/2$  then the second equation in (4.4) gives

$$0 = (1 - n)u + (1 - n)v - av$$

which can be solved for  $v$

$$v = \frac{-(2u - 1 + a) + \sqrt{4au + a^2 - 2a + 1}}{2} \quad (4.5)$$

where we only consider the positive root, since  $v$  must be positive to be biologically relevant. The exact equilibrium can be found by taking the intersection of (4.5) and  $p(n) = 1/2$ . So the final equilibrium is given by

$$(u_3^*, v_3^*) = \left( \bar{u}, \frac{-(2\bar{u} - 1 + a) + \sqrt{4a\bar{u} + a^2 - 2a + 1}}{2} \right)$$

where  $\bar{u}$  is the  $u$ -coordinate of the intersection between (4.5) and  $p(n^*) = 1/2$ , if it exists. Note that  $u_3^*, v_3^* = n^*$ .

We now determine the stabilities of the equilibria, by using linear stability analysis. The Jacobian is given by

$$J(u, v) = \begin{bmatrix} \theta - \zeta u + \zeta(1 - n) & \theta - \zeta u \\ -\theta - 2\xi u + 2\xi(1 - n) - v & -\theta - 2\xi u - v + (1 - n) - a \end{bmatrix} \quad (4.6)$$

where  $\theta = 2p'(n)(1-n)u$ ,  $\zeta = 2p(n) - 1$ ,  $\xi = 1 - p(n)$ . For  $(u_0^*, v_0^*) = (0, 0)$  the Jacobian is given by

$$J(0, 0) = \begin{bmatrix} 2p(0) - 1 & 0 \\ 2(1 - p(0)) & 1 - a \end{bmatrix}. \quad (4.7)$$

Since  $p(0) < 1/2$ , it follows that  $2p(0) - 1 < 0$ . Hence,  $(u_0^*, v_0^*)$  is asymptotically stable if  $a > 1$  and unstable if  $a < 1$ . For  $(u_1^*, v_1^*) = (0, 1 - a)$  the Jacobian is given by

$$J(0, 1 - a) = \begin{bmatrix} a(2p(1 - a) - 1) & 0 \\ 2(1 - p(1 - a))a - 1 - a & a - 1 \end{bmatrix}. \quad (4.8)$$

So if  $a > 1$  then the  $(u_1^*, v_1^*)$  is unstable since  $p(1 - a) = 0$  and also not biologically relevant. If  $a < 1$  and  $p(1 - a) < 1/2$ , then  $(u_1^*, v_1^*)$  asymptotically stable. Finally, if  $a < 1$  and  $p(1 - a) > 1/2$  then  $(u_1^*, v_1^*)$  is unstable. For  $(u_2^*, v_2^*) = (1, 0)$  the Jacobian is given by

$$J(1, 0) = \begin{bmatrix} -(2p(1) - 1) & -(2p(1) - 1) \\ -2(1 - p(1)) & -2(1 - p(1)) - a \end{bmatrix}. \quad (4.9)$$

In this case, trace of  $J(1, 0)$  is

$$\text{tr}(J(1, 0)) = -2p(1) + 1 - 2 + 2p(1) - a = -a - 1 < 0$$

and the determinant of  $J(1, 0)$  is

$$\begin{aligned} \det(J(1, 0)) &= 2(2p(1) - 1)(1 - p(1)) + a(2p(1) - 1) - 2(1 - p(1))(2p(1) - 1) \\ &= a(2p(1) - 1) > 0 \end{aligned}$$

since  $p(1) > 0.5$ . Hence,  $(u_2^*, v_2^*)$  is asymptotically stable. Finally, we show that  $(u_3^*, v_3^*)$  is an unstable saddle point by calculating the determinant of  $J(u_3^*, v_3^*)$ . The determinant simplifies significantly by noting that  $p(n^*) = 0.5$  in this case. So

$$\det(J(u_3^*, v_3^*)) = -2p'(n^*)(1 - n^*)u_3^*a < 0 \quad (4.10)$$

since  $p'(n^*) > 0$ ,  $a, u_3^* > 0$ . Hence,  $(u_3^*, v_3^*)$  is a saddle point.

## 4.4 Existence of an Allee Region

Following the same approach as in [38], we show that (4.4) has an Allee region. In the proof, we make use of the Stable Manifold Theorem.

**Theorem 4.4.1.** *(The Stable Manifold Theorem [38]) Let  $E$  be an open subset of  $\mathbb{R}^n$  containing the origin, let  $f \in C^1(E)$ , and let  $\varphi_t$  be the flow of the nonlinear system  $\dot{x} = f(x)$ . Suppose that  $f(0) = 0$  and that  $Df(0)$  has  $k$  eigenvalues with negative real part and  $n - k$  eigenvalues with positive real part. Then there exists a  $k$ -dimensional differentiable manifold  $S$  tangent to the stable subspace  $E^s$  of the linear system  $\dot{x} = Ax$  at 0 where  $A = Df(0)$ , such that for all  $t \geq 0$ ,  $\varphi_t(S) \subset S$  for all  $x_0 \in S$  and*

$$\lim_{t \rightarrow +\infty} \varphi_t(x_0) = 0.$$

**Theorem 4.4.2.** *(Existence of Allee region)*

- i) If  $a > 1$  there exists a separatrix in system (4.4) that separates the basin of attraction of  $(u_0^*, v_0^*) = (0, 0)$  from  $(u_2^*, v_2^*) = (1, 0)$ . The basin of attraction of  $(u_0^*, v_0^*)$  contained within  $\Delta$  forms the Allee region, in which tumor extinction is achieved.*
- ii) if  $a < 1$  and  $p(1 - a) < \frac{1}{2}$  there exists a separatrix in system (4.4) that separates the basin of attraction of  $(u_1^*, v_1^*) = (0, 1 - a)$  from  $(u_2^*, v_2^*) = (1, 0)$ . The basin of attraction of  $(u_1^*, v_1^*)$  contained within  $\Delta$  forms the Allee region, in which tumor control is achieved, that is CSCs are eradicated and the remaining TCs go quiescent.*

*Proof.* We have already shown that  $\Delta$  is a positively invariant region. For case *i*), we have shown that  $(u_0^*, v_0^*) = (0, 0)$  and  $(u_2^*, v_2^*) = (1, 0)$  are asymptotically stable and that  $(u_3^*, v_3^*)$  is a saddle point. Thus, system (4.4) satisfies the assumptions of the Stable

Manifold Theorem guaranteeing the existence of a stable manifold  $S$  corresponding to  $(u_3^*, v_3^*)$ . This manifold  $S$ , hence forms the separatrix  $S$ , separating the basins of attraction of  $(u_0^*, v_0^*)$  and  $(u_2^*, v_2^*)$ .

Similarly, we have shown that  $(u_1^*, v_1^*) = (0, 1-a)$  and  $(u_2^*, v_2^*) = (1, 0)$  are asymptotically stable and that  $(u_3^*, v_3^*)$  is a saddle point under the constraints in case *ii*). Hence, in this case the assumptions of Stable Manifold Theorem are also satisfied, hence guaranteeing the existence of the separatrix  $S$ , which separates the basins of attraction of  $(u_1^*, v_1^*)$  and  $(u_2^*, v_2^*)$ . See Figure 4.1 (b).  $\square$

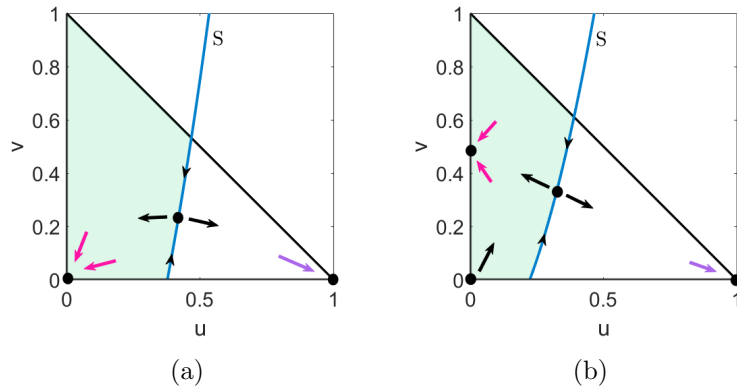


Figure 4.1: Illustration of the cases in Theorem 4.4.2. The area shaded in green is the Allee region  $\Lambda$ , the blue curve is the separatrix  $S$ , and the black triangle is  $\Delta$ . The case of item *i*) is shown in (a) where  $S$  separates the basins of attractions of  $(u_0^*, v_0^*) = (0, 0)$  and  $(u_2^*, v_2^*) = (0, 0)$ . In (b), the case of item *ii*) is shown where  $S$  separates the basins of attraction of  $(u_1^*, v_1^*) = (0, 1-a)$  and  $(u_2^*, v_2^*) = (1, 0)$ .

Now, we want to get an idea of how the Allee region looks like. Due to the assumptions on  $p(n)$ , the manifold  $M_s$  (4.2) is still present in system (4.4), and trajectories converge to it. Therefore, the  $u$ -coordinate of the saddle point  $(u_3^*, v_3^*)$  is a good approximation of the separatrix. We show this in the numerical examples.

## 4.5 Numerical Examples

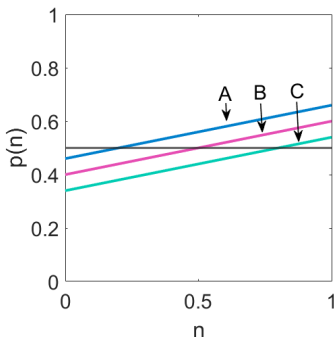
We choose to examine the functions  $p(n)$  shown in Figure 4.2. It turns out that any  $p(n)$  satisfying the assumptions P1-P4 which have the same  $n^*$  yield very similar behaviour, hence we choose to analyze linear functions as they are simple. The three functions we consider are

$$A : p(n) = 0.2(n + 0.3) + 0.4, \quad (4.11)$$

$$B : p(n) = 0.2n + 0.4, \quad (4.12)$$

$$C : p(n) = 0.2(n - 0.3) + 0.4. \quad (4.13)$$

In Figure 4.2, the linear functions A, B, and C. The blue line is the probability function A (4.11) which has the lowest  $n^*$ . The green line is the probability function C (4.13) and has the highest  $n^*$ . Since  $p(c, T)$  defined by (4.3) is monotonically decreasing in  $T$ , C (4.13) has the highest  $T$  concentration whereas A (4.11) has the lowest  $T$  concentration.



(a)

Figure 4.2: Probability functions  $p(n)$  satisfying the assumptions. The blue line is the probability function A defined by (4.11). The pink line is the probability function B defined by (4.12). The green line is the probability function C defined by (4.13).

In Figure 4.3, we summarize the general behaviour of system (4.4) given the probability functions in Figure 4.2. In each plot in Figure 4.3, the equilibria are denoted

by black circles, and some example trajectories are shown in blue. The black diagonal line as well as the  $u$ -axis and  $v$ -axis enclose  $\Delta$ . The approximate Allee region  $\Lambda$ , is highlighted in green and  $M_s$  is the dashed pink line. The death rate  $a$  is varied across columns and the probability function type is varied across rows. In the first column ((a)-(g))  $a = 0.3$ , in the second column ((b)-(h))  $a = 0.7$ , and in the third column ((c)-(i))  $a = 1.3$ . In the first row ((a)-(c)), second row ((d)-(f)) and third row ((g)-(h)), the probability functions are A defined by (4.11), B defined by (4.12), and C defined by (4.13), respectively. We see that  $\Lambda$  increases as  $a$  increases. The top row has the smallest  $n^*$  whereas the bottom row has the largest  $n^*$  and we see that as  $n^*$  increases  $\Lambda$  also increases.

Taking a closer look at the second row containing (d), (e), and (f), in Figure 4.3, we see an example of how a cytotoxic treatment affects the dynamics. For this example, we suppose that (d) is the no treatment case, where tumors have a natural TC death rate of  $a = 0.3$ . In (d), there is no Allee region  $\Lambda$ , so all tumors grow until a tumor comprised of only CSCs is obtained, that is trajectories converge to the steady state  $(u_2^*, v_2^*) = (1, 0)$ . Note that the trajectories in (d) first converge to  $M_s$  defined in (4.2) and then grow towards the full CSC steady state. If a cytotoxic treatment is given, which raises the TC death rate to  $a = 0.7$ , then we get case (e). In (e), due to an increased death rate, an Allee region  $\Lambda$  is present. Tumors falling within  $\Lambda$  converge to the steady state at  $(u_1^*, v_1^*) = (0, 1 - a) = (0, 0.3)$ . Note that in  $\Lambda$  in (e), some tumors decay and some grow, but the CSC density completely dies out. Tumors falling outside  $\Lambda$  in (e), converge to the full CSC density steady state. If the treatment is lifted, then we return to case (d), where tumors that converged to  $(u, v) = (0, 0.3)$ , converge to the new steady state at  $(u_1^*, v_1^*) = (0, 1 - a) = (0, 0.7)$  but the CSC density does not increase. In this case, the tumor remains controlled. The trajectories that did not converge to the steady state at  $(u, v) = (0, 0.3)$  will converge to the full CSC steady state. Case (f) shows a cytotoxic treatment with a high death rate  $a$ . In this case, the tumors falling within  $\Lambda$  in (f), converge to the steady state at  $(u_0^*, v_0^*) = (0, 0)$  hence the tumor can completely die out. Again, tumors that do not fall within  $\Lambda$  in (f) grow

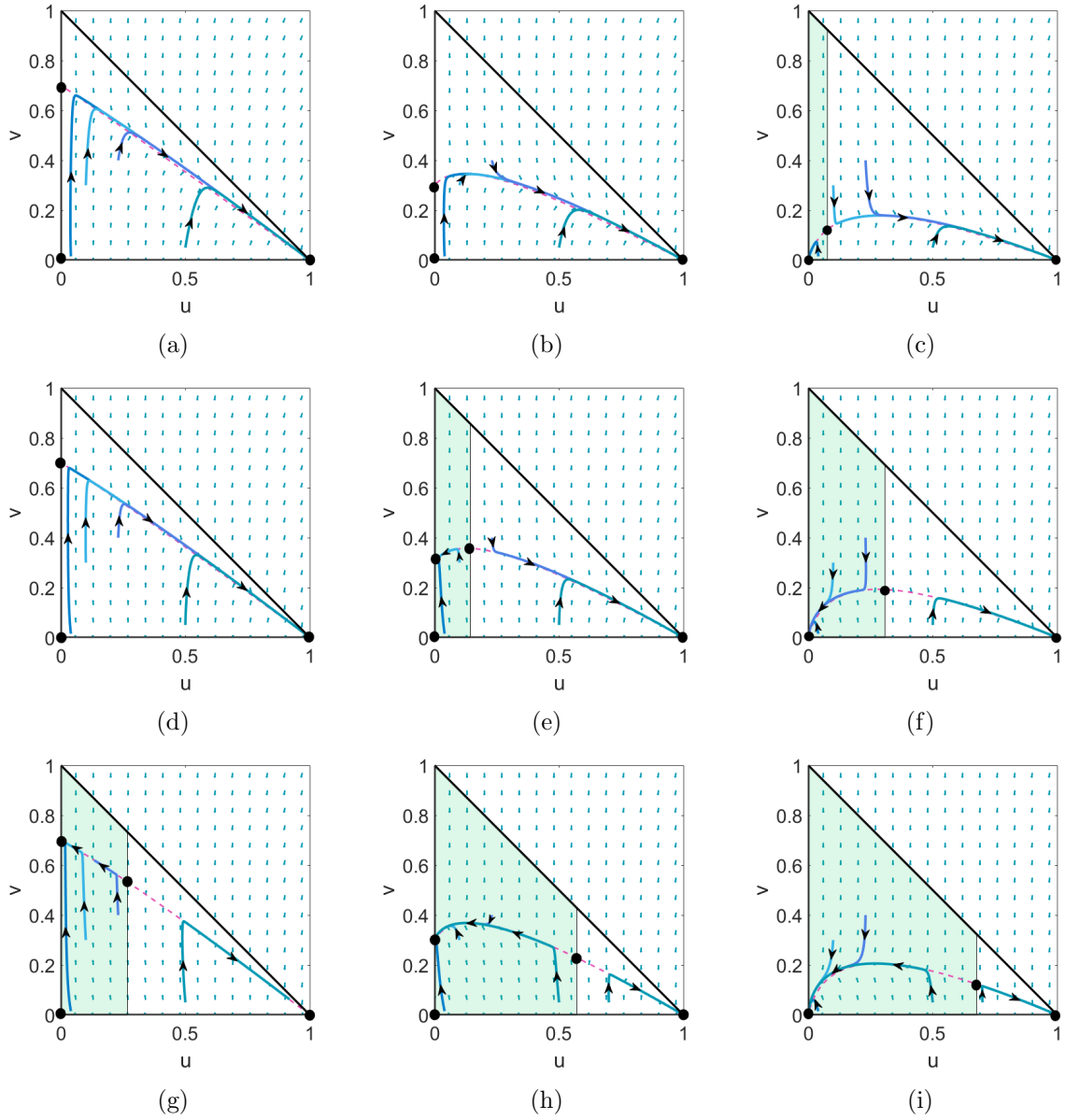


Figure 4.3: Phase portraits of system (4.4). In each figure, the region in green is approximate  $\Lambda$  and the black diagonal along with the axes enclose  $\Delta$ . In (a)-(c) the probability function  $A$  defined by (4.11) is used, in (d)-(f) the probability function  $B$  defined by (4.12) is used, and in (g)-(i) the probability function  $C$  defined by (4.13) is used. In (a),(d),(g)  $a = 0.3$ , in (b),(e),(h)  $a = 0.7$ , and in (b),(f),(i)  $a = 1.3$ . In (c)  $\sigma \approx 0.15$ , in (e)  $\sigma \approx 0.27$ , in (f)  $\sigma \approx 0.52$ , in (g)  $\sigma \approx 0.46$ , in (h)  $\sigma \approx 0.82$ , and in (i)  $\sigma \approx 0.90$ .

towards the full CSC density steady state. Now, the treatment in (f) may seem better than the one in (e), since in (f)  $\Lambda$  is larger and tumors can reach full extinction within it. However, notice that as the TC death rate increases,  $M_s$  defined by (4.2) compresses and with a high enough TC death rate  $a$ , connects to the origin. Recall that in Section 1.5.2, we discussed the tumor growth paradox. Here, the tumor growth paradox is also present, and the tumors in (f) not falling within  $\Lambda$  grow faster than tumors in (d) and (e) (see Figure 1.4 for an illustration of the tumor growth paradox). So case (f) illustrates a trade off of a cytotoxic treatment. On one hand, the Allee region  $\Lambda$  has increased allowing more tumors to fully decay. On the other hand, tumors that did not fall within  $\Lambda$ , grow at an accelerated rate by selecting for CSCs faster.

Now we examine a targeted therapy treatment, focused on increasing the concentration of differentiation promoter  $T$ . For example, we examine the cases (d), (g) in Figure 4.3. Again, we suppose that (d) illustrates the dynamics of the tumors that did not receive treatment where the self-renewal probability function  $p(n)$  is given by B (4.12). In (g), the self-renewal probability function  $p(n)$  is given by C (4.13), hence (g) has a higher concentration of  $T$ . We see that (g) gains an Allee region  $\Lambda$ , and within it the tumors can grow or decay, where the CSC density completely dies out. Notice that in (g),  $M_s$  defined by (4.2) remains unchanged as the TC death rate  $a$  is the same as in (d). Therefore, there is no tumor growth paradox, so the tumors that do not fall within the Allee region  $\Lambda$ , grow as they would without treatment. If we look at case (i), which has a high TC death rate  $a$  and high differentiation promoter  $T$  concentration, we see that the  $\Lambda$  is almost all of the domain  $\Delta$ . Case (i) can represent a combined targeted therapy and cytotoxic treatment, showing that two of these treatments together substantially increase the Allee region  $\Lambda$  hence improving the chances that the tumor will decay completely.

We summarize the trends as  $n^*$  and  $a$  vary in Figure 4.4, where (a) shows the effect of increasing  $a$  with fixed  $n^*$ . The blue curve has the smallest  $n^*$  whereas the green curve has the largest  $n^*$ . We see that the curves quickly saturate, where after a certain point increasing  $a$  gives negligible increase to  $\sigma$  (Allee index). In (b), the impact of

increasing  $n^*$  on  $\sigma$  is shown. The yellow curve has the lowest death rate  $a$  whereas the blue curve has the highest  $a$ . We see that as  $n^* \rightarrow 1$ ,  $\sigma \rightarrow 1$ . In (c), these trends are reiterated, where the value of Allee index is indicated by the color of the plot, where yellow indicates  $\sigma \approx 1$  and blue indicates  $\sigma \approx 0$ . We see that if  $a > 1$ , as  $n^*$  increases, then  $\sigma$  increases. If  $a \leq 1$ , then  $\sigma > 0$  only when  $n^*$  has surpassed a certain value. This shows that at a higher  $a$ , it is easier to increase  $\sigma$  with  $n^*$ .

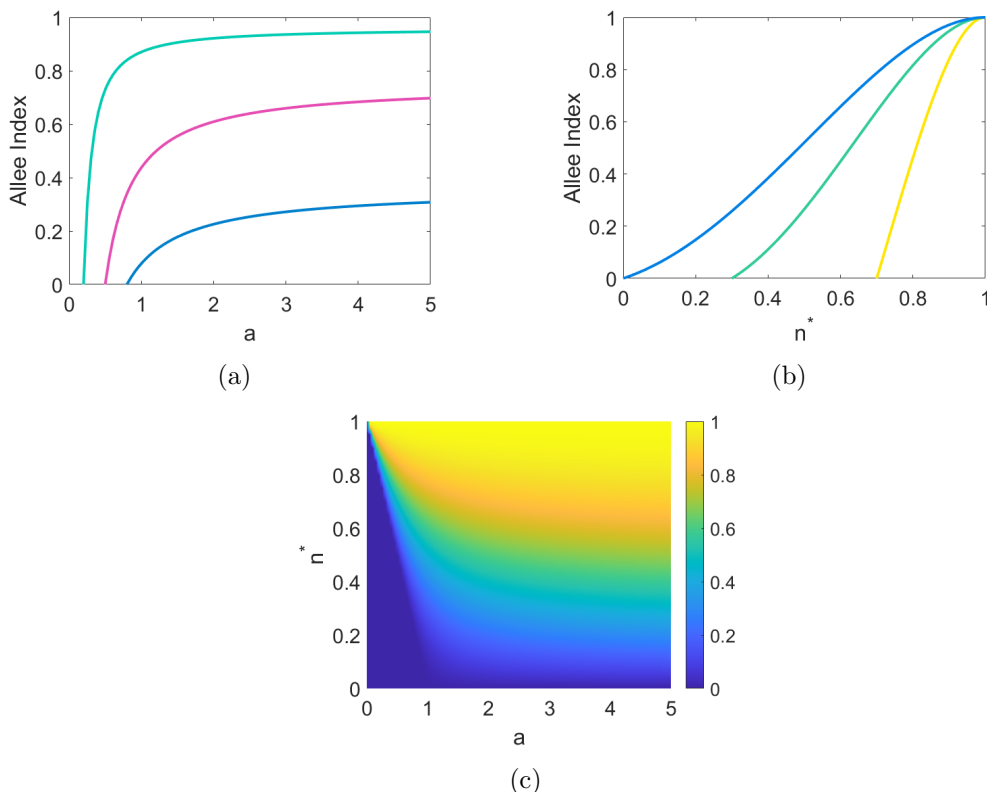


Figure 4.4: In (a) the changes of the Allee indices with respect to  $a$  is summarized. The blue curve uses the probability function A (4.11), the pink curve uses the probability function B (4.12), and the green curve uses the probability function C (4.13). In (b), the changes of the Allee indices with respect to  $n^*$  are summarized. The yellow curve corresponds to  $a = 0.3$ , the green curve corresponds to  $a = 0.7$ , and the blue curve corresponds to  $a = 1.3$ . To obtain (b),  $n^*$  was determined from  $0.5 = p(n) = 0.2(n + b) + 0.4$  by varying  $b$  between  $-0.5$  and  $0.5$ . In (c) a surface plot is shown which varies  $a$  on the x-axis and  $n^*$  on the y-axis, where the value of the Allee index  $\sigma$  is indicated by the colorbar. Plots (a) and (b) are cross sections of (c). In each figure,  $\sigma$  is approximated from  $\bar{u}$ , the u-coordinate of the intersection between (4.5) and  $p(n) = 1/2$ .

We have found that a combined cytotoxic treatment along with targeted therapy focused on increasing differentiation promoters such as BMPs, significantly increases the Allee region thereby greatly improving the chances of achieving tumor control from treatment. This falls in line with previous findings by Youssefpour et al. [70] and Bachman et al. [1], as they also found that a combined treatment consisting of radiotherapy and targeted therapy is more effective at eradicating the tumor. Interestingly, Youssefpour et al. [70] found that a cytotoxic treatment increases tumor aggressiveness post treatment whereas tumor aggressiveness was not impacted post targeted therapy focused on increasing the concentration of differentiation promoters. Our simulations can explain why this occurs. We have seen that increasing the death rate of TCs can lead to a tumor growth paradox. In particular, a tumor which did not fall within the Allee region during the cytotoxic treatment, selected CSCs more quickly. This tumor then has a higher CSC density post treatment, which leads to accelerated growth and invasion. Further, we observed that increasing the amount of differentiation promoters, did not accelerate the selection for CSCs. Hence, once treatment is lifted after targeted therapy, the tumor has similar growth dynamics which were prior to treatment.

Bachman et al. [1] used a similar model to (4.1) to assess which treatment succeeds by fixing the concentration of self-renewal promoters and varying the concentration of differentiation promoters. To assess treatment success they calculate the tumor control probability (TCP) based on the amount of CSCs that remain and find that a combined treatment consisting of radiotherapy and targeted therapy is more effective than applying only one of those treatments. Here, we fixed the concentration of differentiation promoters and varied the concentration of self-renewal activators, which resulted in the same conclusion. We do not evaluate TCP, as we know that if a tumor falls within the Allee region and that treatment is applied long enough, tumor control is achieved. Note that in some cases, we saw that when CSCs completely die out, a substantial TC density can remain. We still say that the tumor is controlled, as the TC density cannot sustain itself without CSCs and it will eventually die out. For tumors falling outside the Allee region, tumor control is not possible, and a different treatment is required.

Note that we did not examine a cytotoxic treatment that also effects CSCs which can improve the amount of tumor cases that reach tumor control.

Now that we have studied the impact of the Allee effect in cancer stem cell models, we move on to testing whether an Allee model can explain experimental data of tumor growth better than a model without it. Due to the limited data, we must significantly simplify our models. To do this, we return to the models in earlier chapters as there is not enough data to fit a full cancer stem cell model with feedback mechanisms.

# Chapter 5

## Model Fitting to Lung Cancer Data

### 5.1 Modelling of Non-Small Cell Lung Cancer

A number of mathematical models have been proposed to model the tumor volume dynamics of non small cell lung cancer (NSCLC) [23, 34, 40, 3, 64]. Geng et al. [23] proposed a fairly simple one dimensional ODE model, which incorporated radiotherapy and chemotherapy treatments. In [23], tumor growth was modelled using a Gompertz curve (which is similar to a logistic growth curve), radiotherapy was modelled by a standard linear quadratic model (details of this model are found in Section 5.3), and chemotherapy was modelled using the log-cell kill model. A log-cell kill model proposes that the kill rate from chemotherapy can be described by an exponentially decaying function that depends on the drug dosage given. By using available survival data in the literature, they were able to estimate the parameters for their one dimensional ODE model. Geng et al. [23] found that their model is able to explain the survival data well, and that concurrent chemo-radiotherapy is superior at extending survival time in comparison to sequential chemo-radiotherapy. The one dimensional model proposed by Geng et al. [23] lacks the latency time effect which was found to be crucial in explaining the gross tumor volume NSCLC data [64]. Tariq et al. [64] contrasted one dimensional and two dimensional models which model tumor growth and radiotherapy

treatment. The difference between the one dimensional models is that one assumes that the growth of the tumor is exponential whereas the other assumes that the tumor growth is logistic. The two dimensional models extended the one dimensional models by adding a damaged volume compartment to incorporate the latency time effect. The radiotherapy treatment was modelled by the linear quadratic model. The models were then fit to data obtained from 18 patients diagnosed with stage I NSCLC who had their gross tumor volume collected for about 16 days. An exponential growth model with a latency time was found to fit the gross tumor volume data the best.

Other differential equation models for NSCLC have been proposed that account for treatment resistant and treatment sensitive cells in chemotherapy [40], latency time effect [34], and metastasis [3]. In this chapter, we focus on developing the simplest mathematical model that is able to describe the long term gross tumor volume dynamics of NSCLC. Our resulting model will resemble a two dimensional logistic growth model proposed by Tariq et al. [64]. The difference will be in the way we implement the linear quadratic model and we also account for chemotherapy. Further, we will employ a similar method to the one used in [64] for choosing optimal parameters.

## 5.2 Patient Data

The data we use was provided from a study conducted in 2021 by OncoRay - National Center for Radiation Research in Oncology in Dresden, Germany. In this study, 39 patients diagnosed with stage III NSCLC had their gross tumor volume collected. The patients received either concurrent chemotherapy and intensity-modulated radiotherapy type I or concurrent chemotherapy and intensity-modulated radiotherapy type II. The difference between intensity-modulated radiotherapy type I and type II is the particle used to deliver the radiation. Each patient had a planning CT scan collected before treatment, and once the treatment started, a CT scan was collected every two weeks following the start date of treatment, where the final CT scan was collected on the sixth week after the treatment start date. Follow up CT scans were then collected 3, 6, 9,

and 12 months after the treatment end date.

The patients received intensity-modulated radiotherapy type I or type II 6 times per week with an approximate dosage of 2 Gy per day until a total dose of 66 Gy was reached. Further, patients received chemotherapy where 45 mg/m<sup>2</sup> of paclitaxel and 2 AUC (mg·min/mL) of carboplatin was given per week. The specific amount of the chemotherapy drugs given in milligrams depends on the patient, due to fluctuations in body mass during treatment. Further, the amount of weeks chemotherapy lasts is also patient dependent, due to different responses to treatment. There is also some delay between the planning CT scan and the start of treatment. The dates when the planning CT scan and the start date of chemotherapy are available. Further, the gender and age of the patients was recorded as well.

Although 39 patients were enrolled into the study, only 26 of them had 5 or more CT scans collected. So we focus on fitting the model to those 26 patients, where 11 out of the 26 patients received concurrent chemotherapy and intensity-modulated treatment type I whereas the other 15 patients received concurrent chemotherapy and intensity-modulated treatment type II. Further, 8 out of the 26 patients are female, and the rest are male. We reduce the data set to 26 patients, as each of them yields a reasonable amount of data points to estimate our model parameters using the Latin Hypercube Sampling Method, which will be explained in Section 5.4.

### 5.3 Model Derivation

Since only the gross tumor volume is available, the CSC and TC volumes are indistinguishable in the data. Hence, we derive a simplified model for tumor growth that is based on the gross tumor volume.

We derive a model that describes the gross tumor dynamics by simplifying model (1.7), which is the model that describes the CSC and TC dynamics while accounting for space limitations. From our previous analysis, we have seen that the long term dynamics of the tumor occurs on the slow manifold. We can therefore assume that the

tumors in the data have already settled onto the slow manifold  $M$  (given by (1.19)). Hence, we consider the slow system of (1.7) which is given by

$$\begin{aligned}\dot{u} &= kF(n)u, \\ 0 &= kF(n)u + k_2F(n)v - av,\end{aligned}\tag{5.1}$$

where  $n = u + v$  and  $F(n)$  satisfies assumptions F1 and F2. Now we assume that  $u \approx n$  since the tumors have been growing for a while and CSCs have naturally been selected for. With this assumption, we rewrite (1.7) as

$$\dot{n} = kF(n)n.\tag{5.2}$$

We choose  $F(n) = 1 - (n/K)$  which satisfies assumptions F1 and F2, and makes (5.2) exhibit logistic growth. Letting  $x$  denote the tumor volume, we rewrite (5.2) to obtain

$$\dot{x} = r \left(1 - \frac{x}{K}\right) x\tag{5.3}$$

where  $r$  is the growth rate of the tumor and  $K$  corresponds to the carrying capacity volume. Doing a similar reduction with the Allee model (2.1), we obtain a related equation to (5.3) with an Allee factor

$$\dot{x} = r \left(1 - \frac{x}{K}\right) (x - A) x.\tag{5.4}$$

The next step is to incorporate treatment and the latency time effect. Treatment can be incorporated using a general treatment function  $H(t)$  which will be specified shortly, and the latency time effect is accounted for with a damaged compartment  $y$ . With this, (5.3) becomes

$$\begin{aligned}\dot{x} &= r \left(1 - \frac{x + y}{K}\right) x - H(t)x, \\ \dot{y} &= H(t)x - \gamma y.\end{aligned}\tag{5.5}$$

where  $\gamma$  is the clearance rate. Here, as cancer cells get damaged, a volume  $y$  of damaged cells is formed. We assume that the damaged cells do not contribute new cancer cells and the damaged volume gets cleared with rate  $\gamma$  (either from death or the immune system). Further, since space is limited we modify the logistic term to account for the damaged volume as well.

Now we define an explicit treatment function  $H(t)$  which will incorporate radiotherapy and chemotherapy treatments. We employ the linear quadratic (LQ) model to model the effect from radiation therapies [25, 23]. When the fraction dose is less than 10 Gy, the LQ model describes the effect of radiation on a tumor well [23]. The LQ model is given by

$$\dot{x} = -(\alpha + \beta d)d(t)x \quad (5.6)$$

where  $\alpha$  and  $\beta$  are the radiosensitivity parameters,  $d$  is the dose, and  $d(t)$  is the dose rate.

To model chemotherapy, we use the model given below

$$\begin{aligned} \dot{x} &= -\mu(1 - e^{-C(t)})x \\ \dot{C} &= b(t) - \xi C(t) \end{aligned} \quad (5.7)$$

where  $\mu$  is the rate of fractional tumor cell kill by chemotherapy,  $C(t)$  is the concentration of the drug and  $\xi$  is the decay rate of the drug determined from  $\xi = \ln(2)/\text{HL}$  where HL is the half-life of the drug. The dose rate  $b(t)$  depends on the treatment schedule. During treatment time  $b(t) = D$  where  $D$  is the specified dose rate, otherwise  $b(t) = 0$ . This model is linear for low dose of chemotherapy but as the dose increases the concentration saturates to  $\mu$ . This model is typically used in modelling chemotherapy and has been shown to match experimental data well [52, 22]. With this, we get the

model which incorporates treatment

$$\begin{aligned}
\dot{x} &= rx \left(1 - \frac{x+y}{K}\right) - (\alpha + \beta d)d(t)x - \mu(1 - e^{-C_1(t)})x - \mu(1 - e^{-C_2(t)})x, \\
\dot{y} &= (\alpha + \beta d)d(t)x + \mu(1 - e^{-C_1(t)})x + \mu(1 - e^{-C_2(t)})x - \gamma y, \\
\dot{C}_1 &= b_1(t) - \xi_1 C_1(t), \\
\dot{C}_2 &= b_2(t) - \xi_2 C_2(t).
\end{aligned} \tag{5.8}$$

We call system (5.8) Model 1. Analogously, we obtain a second model which incorporates the Allee effect

$$\begin{aligned}
\dot{x} &= rx \left(1 - \frac{x+y}{K}\right) (x+y-A) - (\alpha + \beta d)d(t)x - \mu(1 - e^{-C_1(t)})x - \mu(1 - e^{-C_2(t)})x, \\
\dot{y} &= (\alpha + \beta d)d(t)x + \mu(1 - e^{-C_1(t)})x + \mu(1 - e^{-C_2(t)})x - \gamma y, \\
\dot{C}_1 &= b_1(t) - \xi_1 C_1(t), \\
\dot{C}_2 &= b_2(t) - \xi_2 C_2(t).
\end{aligned} \tag{5.9}$$

We call (5.9) Model 2. Model 2 is nearly identical to (5.8) except the growth term of the tumor takes the Allee effect into account. As the total volume  $x+y$  decreases below the threshold volume  $A$ , the growth rate is negative and the tumor decays. Here is a summary of the parameter meanings:

- $r$  is the growth rate (1/day)
- $K$  is the carrying capacity ( $\text{cm}^3$ )
- $\alpha, \beta$  are the radiosensitivity parameters ( $\text{Gy}^{-1}$ ), ( $\text{Gy}^{-2}$ )
- $d$  is the radiation dose per fraction (Gy)
- $d(t)$  is the radiation dose rate (Gy/day)
- $\mu$  is the rate of tumor cell kill by chemotherapy (1/day)
- $\gamma$  is the clearance rate (1/day)

- $A$  is the Allee constant ( $\text{cm}^3$ )
- $C_i$  is the concentration of the chemotherapy drug  $i = 1, 2$  ( $\text{mg/L}$ )
- $\xi_i$  is the decay rate of the drug  $i$  ( $1/\text{day}$ )
- $b_i$  is the dose rate of the drug  $i$  ( $\text{mg}/(\text{L}\cdot\text{day})$ )

## 5.4 Model Fitting

To fit the model, we use Latin Hypercube Sampling (LHS) to obtain random parameter sets to use for model simulations. LHS is a random sampling method which has been described in [46] and here we outline how the method works.

To understand LHS, it is best to consider a simple two dimensional example. Suppose we want to estimate two parameters,  $a$  and  $b$ , where the parameter ranges are  $a \in [\underline{a}, \bar{a}]$  and  $b \in [\underline{b}, \bar{b}]$ . Call the intervals  $I_a = [\underline{a}, \bar{a}]$  and  $I_b = [\underline{b}, \bar{b}]$ . Now, these intervals can be divided into  $N$  equidistant subintervals. If we choose  $N = 5$ , then for this example  $I_a$  yields 5 intervals of equal length:  $[a_0, a_1], [a_1, a_2], [a_2, a_3], [a_3, a_4], [a_4, a_5]$  where  $a_0 = \bar{a}$  and  $a_5 = \underline{a}$ . Similarly, we can obtain five equidistant intervals for  $I_b$ . Note that for general  $N$ , we obtain  $N$  equidistant intervals:  $[a_{i-1}, a_i], i = 1, 2, \dots, N$  where  $a_i$  is a parameter.

Now that we have  $N$  intervals, an interval is selected randomly for each parameter. Suppose,  $[a_1, a_2]$  and  $[b_4, b_5]$  were chosen. Now, a random number from each of these intervals is chosen uniformly from the interval. As an example,  $a_f$  is chosen from  $[a_1, a_2]$  and  $b_f$  is chosen from  $[b_4, b_5]$ . Hence,  $(a_f, b_f)$  defines the parameter set from this cycle. If  $[a_1, a_2] = [0.88, 1.66]$  and  $[b_4, b_5] = [12, 17.7]$  then  $(a_f, b_f) = (1.4, 16.1)$ , for example. This parameter set falls into the green square in Figure 5.1.

The method then repeats this process to choose more parameter sets where previously chosen intervals cannot be chosen again. This means that for the example in Figure 5.1 anything from the highlighted row in yellow, and the highlighted column in

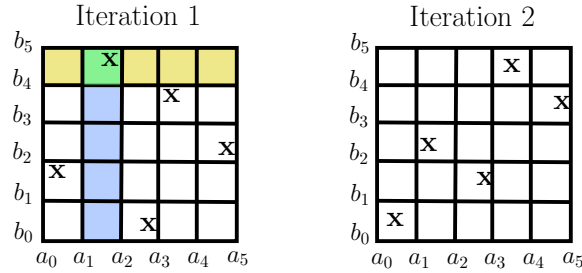


Figure 5.1: Illustration of the Latin Hypercube Sampling method. Here the parameter ranges for  $a$  and  $b$  are divided into 5 equidistant intervals. In Iteration 1, 5 parameter sets are semi randomly generated where each parameter set is denoted by X. In Iteration 2, 5 new parameter sets are generated.

blue in Figure 5.1 cannot be chosen. Hence, for this example we obtain 5 parameter sets as shown in Figure 5.1 in Iteration 1.

In general, we consider  $m$  parameters  $p^{(1)}, \dots, p^{(m)}$  within intervals  $p^{(j)} \in I^{(j)}$  where  $I^{(j)} = [\underline{p}^{(j)}, \bar{p}^{(j)}]$ ,  $j = 1, \dots, m$ . We divide each interval  $I^{(j)}$  into  $N$  equidistant subintervals and randomly choose subintervals for each parameter in a way that subintervals are only used once. Then, in each chosen subinterval we randomly choose a representative value of  $p^{(j)}$ .

The above outlines the Latin Hypercube Sampling method. The advantage to using this method is that the semi randomness allows us to sample the entire space, which is an advantage over the Monte Carlo method. In the Monte Carlo method there is a greater chance to underrepresent parameter values due to the chance of choosing a parameter set from only a particular region in the parameter space. The Latin Hypercube Sampling method takes care of this issue.

Now to generate parameter sets for the model (5.8), we set  $N = 7500$ . This value is chosen so that that the intervals are sufficiently fine for accuracy but not too large that it becomes computationally expensive. As our data is limited for each patient we choose to fix the radiosensitivity parameters in order to reduce the amount of parameters. We set  $\alpha = 0.0398Gy^{-1}$  which is the average value that Geng et al. estimated in [23]. We then set  $\alpha/\beta = 10Gy$  which is an approximation typically used in lung cancer [23, 64]. We use the following parameter ranges for parameter estimation in Model 1. These

intervals were chosen as they give sufficient fits to the data and do not deviate far from the reported values in the literature:

- The parameter range for growth rate  $r$  with units  $\text{day}^{-1}$  was set to be  $[0.00001, 0.2]$ . We choose to extend it below the lower bound in Tariq et al. [64] used in order to allow for slower growth. We use the upper bound of 0.2 which is approximately the upper bound of growth rates of cancer reported in the literature [9, 48, 57], and contains the computed growth rates of NSCLC [3, 23].
- The parameter range for the clearance rate  $\gamma$  with units  $\text{day}^{-1}$  was set to be  $[0.0001, 0.05]$ . The range falls into the range used by Tariq et al [64] where the lower bound is the same. In [10], half lives of cell disintegration post radiation are reported where the half life for squamous cell carcinoma is 28.2 days and the half life for adenocarcinoma is 72.4 days. Hence, an estimate for the clearance rates is given by  $0.0246 \text{ day}^{-1}$  and  $0.0096 \text{ day}^{-1}$  using the relationship  $\ln(2)/\text{half-life}$  for squamous cell carcinoma and adenocarcinoma, respectively. We choose to double  $0.0246 \text{ day}^{-1}$  and set that as our upper bound. This is done to account for faster clearance rates.
- The parameter range for the rate of fractional tumor cell kill by chemotherapy  $\mu$  with units  $\text{day}^{-1}$  was set to be  $[0, 1]$ . We set the lower bound to be 0 in order to represent no effect from chemotherapy and the upper bound is extended beyond the  $\mu = 0.9$  reported in [52] to account for a more sensitive chemotherapy response.
- The carrying capacity  $K$  with units  $\text{cm}^3$  depends on the planning CT tumor volume  $V_{CT}$  for each patient. If  $V_{CT} < 100$ , then the range was set to be  $[V_{CT}, 150]$ . If  $100 < V_{CT} < 200$  then the range was  $[V_{CT}, 200]$  and if  $V_{CT} > 200$  then the range was  $[V_{CT}, 550]$ . This is done so that the intervals are less broad and more focused.
- In addition to the above parameters we also set the initial volume of the tumor  $V_0$  as a parameter and set the range to be  $[V_{CT} - 0.25V_{CT}, V_{CT} + 0.25V_{CT}]$ .

- The parameter range for the Allee constant was set to be  $[-10, 10]$ . This interval is quite wide in order to find the appropriate constant for each patient. Further, the average of the initial data is  $119.76\text{cm}^{-3}$  so 10% of this is approximately 10 which forms the upper bound.

For Model 2, the same parameter ranges were used with the exception of the growth rate range. For Model 2  $r \in [0.00001, 0.02]$  where the upper bound is decreased by a factor of 10 to account for faster growth in Model 2. The growth term in Model 2 is cubic, which grows faster than quadratic growth in Model 1. We simulate Model 1 (5.8) and Model 2 (5.9) using parameter sets from the LHS procedure. Each model was simulated using Matlab ODE45 solver.

As patients usually did not receive treatment immediately after their planning CT scan, the time between the planning CT and treatment was estimated for each patient. We use the date of the planning CT scan and the start date of chemotherapy to estimate when treatment begins. As the start date of radiotherapy is unavailable, we assume that radiotherapy began three days prior to chemotherapy. For chemotherapy, we assume that it is applied weekly on the same day each week. The amount of milligrams the patient receives of each drug is estimated and then divided by 5L which is approximately the average blood volume in adults [61]. This yields the approximate drug concentration dose that the patient received per day. We set the half life of paclitaxel to be 9.5h which is the average of the reported range in [24] and the half life of carboplatin to be 4h which is the average in the reported range in [33] ( $\xi$  is estimated by  $\ln(2)/\text{HL}$ ). For intensity-modulated radiotherapy treatments, we assume that patients receive 2 Gy each day. Hence, on treatment days when radiation is applied the rate of radiation is 2 Gy/day.

Note that for some patients, data was missing. For patients who did not have the start date of chemotherapy available, we use the average amount of days it took to start treatment, which was computed from other patients. Two patients had chemotherapy applied, where some applications had the dose in mg available but other application

doses were unknown. In these cases, we take the average of the known doses, and use the resulting value as the estimated dose for the unavailable doses. One patient had all doses in mg unavailable. In that case, we estimate the dose given by taking average of all patient doses, for a particular drug.

After the models have been simulated, a modified residual sum of squares ( $RSS_{mod}$ ) is used to calculate the error. The  $RSS_{mod}$  formula is given by

$$RSS_{mod} = \sum_{i=1}^n (\ln(y_i) - \ln(f(t_i; \hat{p})))^2 \quad (5.10)$$

where  $y_i$  is the data points and  $f(t_i; \hat{p}) = x(t_i; \hat{p}) + y(t_i; \hat{p})$  which is the total tumor volume at  $t_i$ . We choose to take the logarithm of  $y_i$  and  $f(t_i; \hat{p})$  as the data for certain patients can vary several orders of magnitude. This decreases the emphasis on error from large measurements and increases emphasis on error from small measurements giving a more representative measure of error.

Finally, after simulating the model  $N$  times the parameter set with the minimum  $RSS_{mod}$  is chosen. This process is repeated 10 more times to choose the parameter set that gives the least error between the data and the curve. We note that due to the random selection of parameters each fit is slightly different with each simulation but the general shape of the curve is consistent for each run.

## 5.5 Results

Now, we show the resulting fits of the models to the data. Figures 5.2 and 5.4 summarize the resulting fits from Model 1. Figure 5.2 shows 11 out of 11 good fits from intensity-modulated radiotherapy treatment type I, and Figure 5.4 shows the 12 out of 15 good fits from intensity-modulated radiotherapy treatment type II. The 3 poor fits from Model 1 are summarized in Figure 5.6. In each figure, the blue curve shows the simulation from the model, the black curve is the predicted tumor volume without treatment and the pink dots are the data. The light blue bar marks the duration of the radiation

treatment. Similarly, the 23 good fits from intensity-modulated radiotherapy treatment type I and II for Model 2 are shown in Figure 5.3 and Figure 5.5. The 3 poor fits are summarized in Figure 5.7 for Model 2. Note that Patient 33 did not have the start date of the chemotherapy treatment available, Patients 8 and 9 had some chemotherapy doses available, and Patient 10 had no chemotherapy doses available. We see that Model 1 and Model 2 yield similar fits, and both fail to explain the data for Patient 19, 30 and 36. We also see that there appears to be no significant difference in patient outcomes for the intensity-modulated radiotherapy treatments type I and II, since both have about the same amount of cases of tumor decay and tumor regrowth.

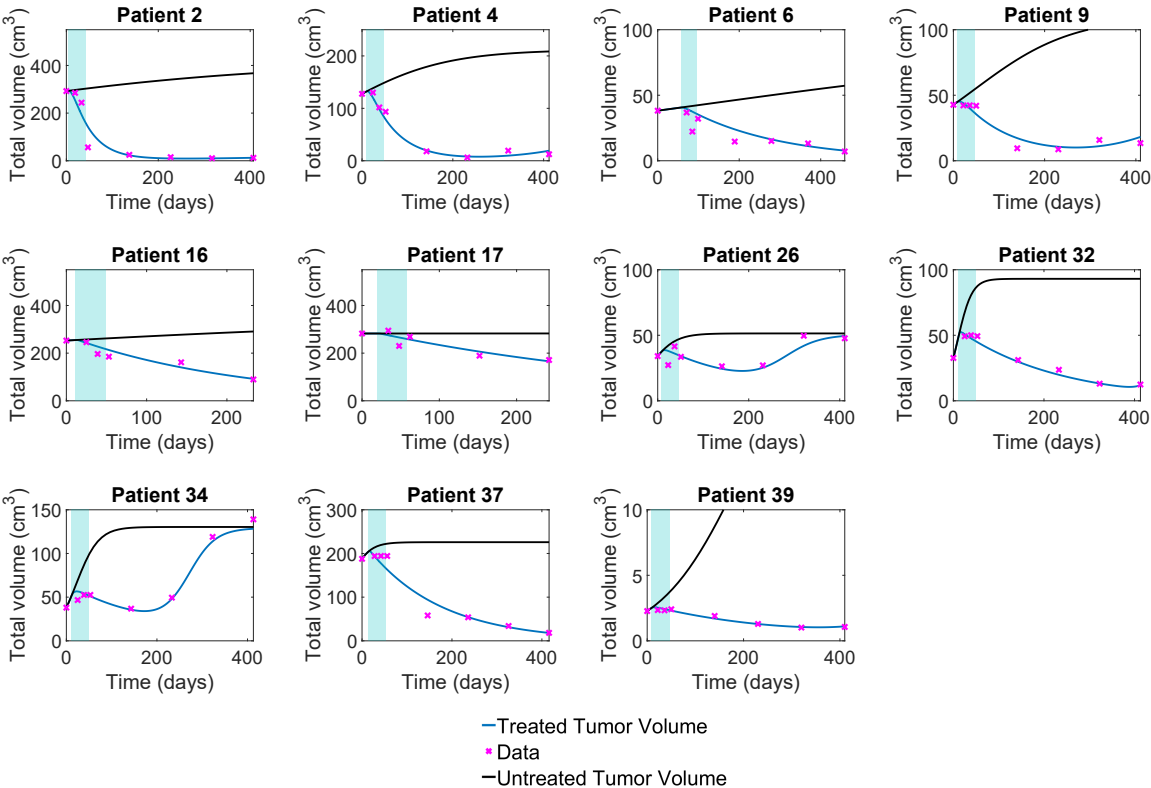


Figure 5.2: Model 1 (5.8) fits to patients who received intensity-modulated radiotherapy treatment type I. For each figure, the  $y$  axis denotes the total volume in  $\text{cm}^3$  and the  $x$  axis denotes the time measured in days. The blue curve shows the simulated tumor volume with treatment and the black curve shows the simulated tumor volume without treatment. The pink dots denote the data corresponding to each patient and the blue highlight marks the duration of the radiation treatment.

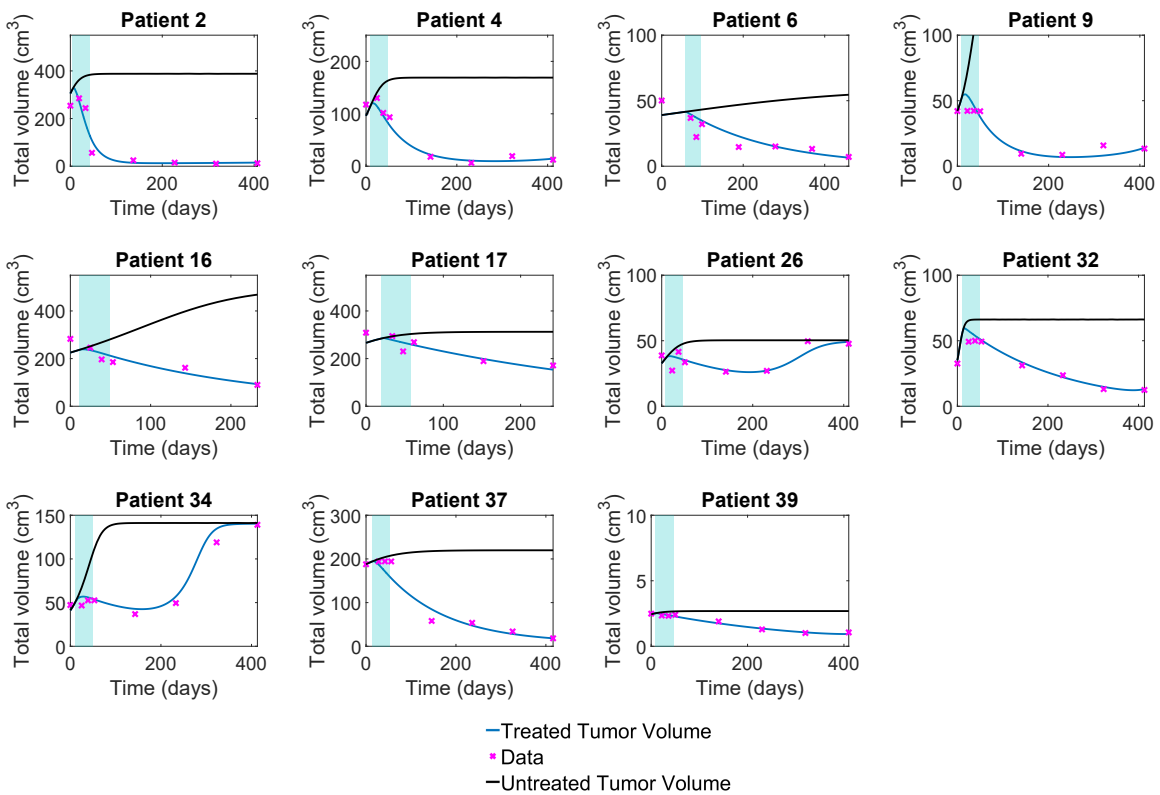


Figure 5.3: Model 2 (5.9) fits to patients who received intensity-modulated radiotherapy treatment type I. For each figure, the  $y$  axis denotes the total volume in  $\text{cm}^3$  and the  $x$  axis denotes the time measured in days. The blue curve shows the simulated tumor volume with treatment and the black curve shows the simulated tumor volume without treatment. The pink dots denote the data corresponding to each patient and the blue highlight marks the duration of the radiation treatment.

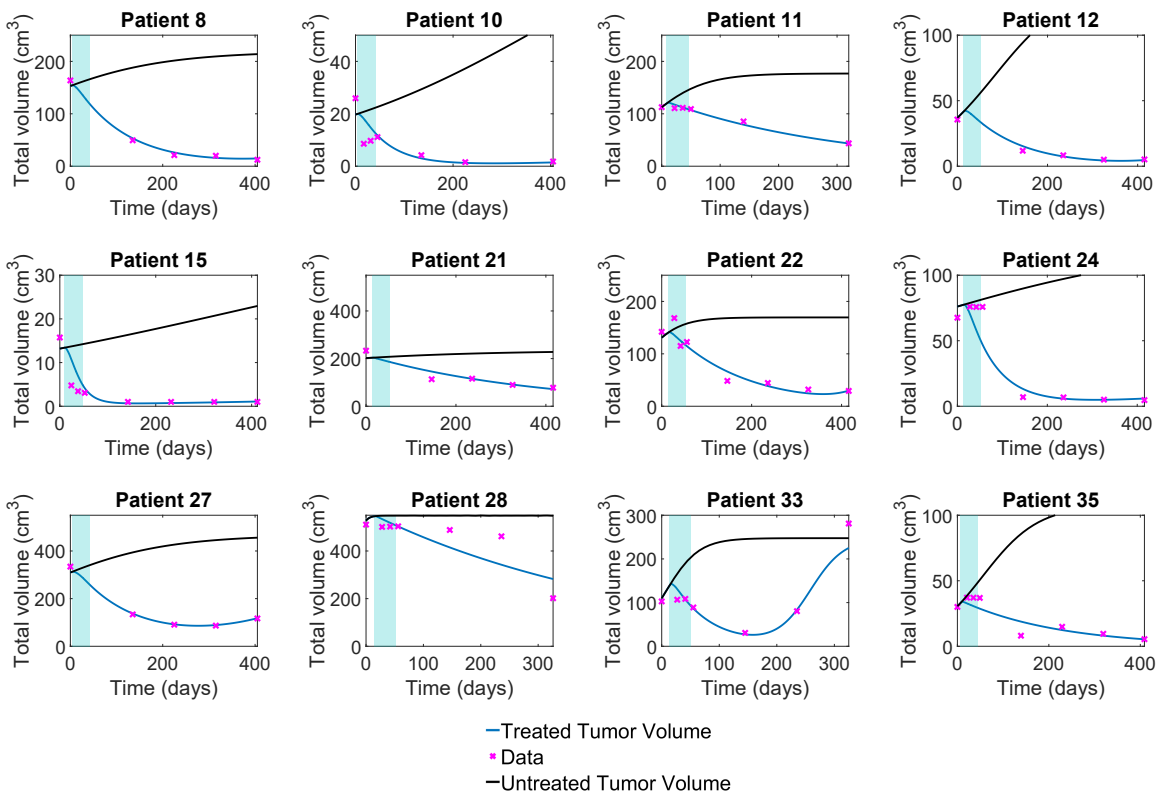


Figure 5.4: Model 1 (5.8) fits to patients who received intensity-modulated radiotherapy treatment type II. For each figure, the  $y$  axis denotes the total volume in  $\text{cm}^3$  and the  $x$  axis denotes the time measured in days. The blue curve shows the simulated tumor volume with treatment and the black curve shows the simulated tumor volume without treatment. The pink dots denote the data corresponding to each patient and the blue highlight marks the duration of the radiation treatment.

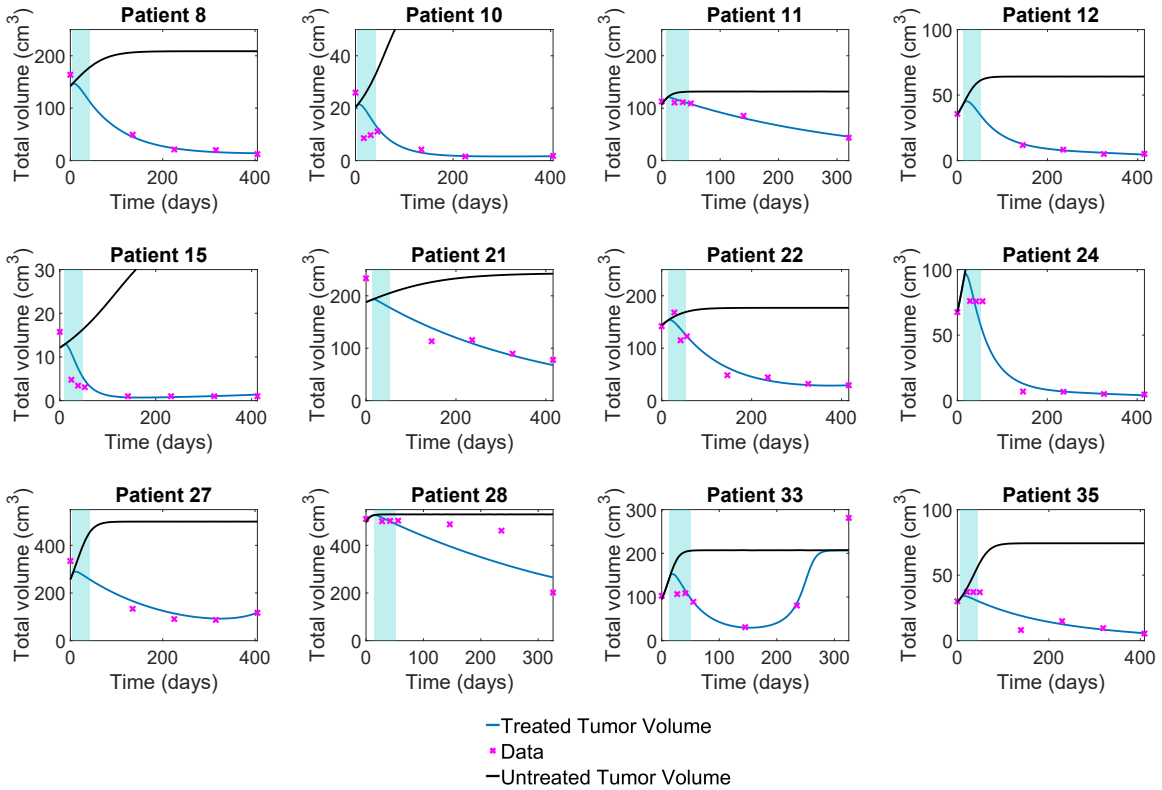


Figure 5.5: Model 2 (5.9) fits to patients who received intensity-modulated radiotherapy treatment type II. For each figure, the  $y$  axis denotes the total volume in  $\text{cm}^3$  and the  $x$  axis denotes the time measured in days. The blue curve shows the simulated tumor volume with treatment and the black curve shows the simulated tumor volume without treatment. The pink dots denote the data corresponding to each patient and the blue highlight marks the duration of the radiation treatment.

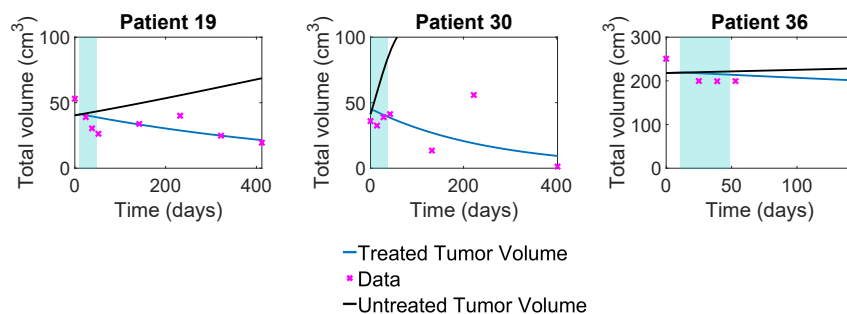


Figure 5.6: Poor fits from Model 1 (5.8). All patients in this figure received intensity-modulated radiotherapy treatment type II. For each figure, the  $y$  axis denotes the total volume in  $\text{cm}^3$  and the  $x$  axis denotes the time measured in days. The blue curve shows the simulated tumor volume with treatment and the black curve shows the simulated tumor volume without treatment. The pink dots denote the data corresponding to each patient and the blue highlight marks the duration of the radiation treatment.

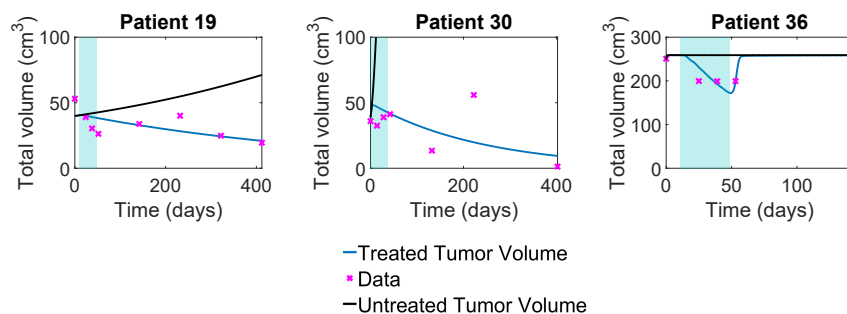


Figure 5.7: Poor fits from Model 2 (5.9). All patients in this figure received intensity-modulated radiotherapy treatment type II. For each figure, the  $y$  axis denotes the total volume in  $\text{cm}^3$  and the  $x$  axis denotes the time measured in days. The blue curve shows the simulated tumor volume with treatment and the black curve shows the simulated tumor volume without treatment. The pink dots denote the data corresponding to each patient and the blue highlight marks the duration of the radiation treatment.

To assess which model fits the data better, we use the corrected Akaike Information Criterion (AICc) since we have few data points. The AICc formula is given by

$$\text{AICc} = 2LL(\hat{p}) - 2n_p \frac{N}{N - n_p - 1} \quad (5.11)$$

where  $LL$  represents the log-likelihood,  $\hat{p}$  represents the parameters,  $n_p$  is the number of parameters, and  $N$  is the number of data points [15]. Since maximizing the log-likelihood is equivalent to minimizing the sum of squares, we can write (5.11) as

$$\text{AICc} = -\frac{1}{\sigma^2}SS(\hat{p}) - 2n_p \frac{N}{N - n_p - 1} \quad (5.12)$$

where

$$SS = \min \sum_{i=1}^n (y_i - f(t_i; \hat{p}))^2 \quad (5.13)$$

and  $\sigma^2$  is the variance of the data [15]. This test suggests that the value with the highest AICc is the better model. Since each patient has a different set of data, we compute the AICc for each patient. We ignore the patients that have  $N - n_p - 1 = 0$  for at least one of the models and choose the best model based on which has the highest AICc for the greatest amount of patients. Since there are no replicate data points, we assume that  $\sigma = 10$  as that seems appropriate for the data set. The AICc values for both models are summarized in Table 5.1. From Table 5.1, it is evident that Model 1 (5.8) has higher AICc values for most of the patients, hence it is predicted to be the better model. This shows that the Allee effect is not necessary to explain the NSCLC data, even though it appears to also fit the data. From here, we focus on studying Model 1.

To assess how well Model 1 is able to explain the data we calculate the  $R^2$  values. The  $R^2$  value is called the coefficient of determination and is a typical statistical measure used to assess how well a given model is able to explain the data in linear regression [12]. The coefficient is calculated by

$$R^2 = 1 - \frac{\text{RSS}}{\text{TSS}} \quad (5.14)$$

Patient	Model 1 AICc	Model 2 AICc	Patient	Model 1 AICc	Model 2 AICc
2	-145.77	-137.31	22	-38.85	-50.78
4	-27.04	-51.01	24	-34.18	-47.64
6	-26.18	-44.35	26	-23.70	-62.34
8	*	*	27	*	*
9	-22.93	-42.34	28	-305.23	-394.31
10	-29.57	-72.11	30	-132.71	-151.58
11	*	*	32	-21.79	-41.00
12	*	*	33	-65.96	-139.95
15	-21.89	-40.68	34	-24.66	-44.89
16	*	*	35	-23.90	-42.21
17	*	*	36	*	*
19	-26.65	-45.35	37	-47.72	-70.01
21	*	*	39	-21.33	-40.00

Table 5.1: Table of AICc values. Patients who have  $N - n_p - 1 = 0$  are denoted by \*.

where RSS is the residual sum of squares given by

$$\text{RSS} = \sum_{i=1}^n (y_i - f(t_i; \hat{p}))^2, \quad (5.15)$$

Here  $y_i$  are the data points and  $f(t_i; \hat{p}) = x(t_i; \hat{p}) + y(t_i; \hat{p})$  which is the total tumor volume at  $t_i$ . The total sum of squares is given by

$$\text{TSS} = \sum_{i=1}^n (y_i - \bar{y})^2 \quad (5.16)$$

where  $\bar{y}$  is the average of the data points calculated by

$$\bar{y} = \frac{1}{n} \sum_{i=1}^n y_i. \quad (5.17)$$

If  $R^2 = 1$  then the model is able to explain the observed data for a linear regression model [12]. Here, since we have a nonlinear model, the  $R^2$  values must be interpreted with caution. We compute the  $R^2$  in order to identify patients with low  $R^2$  values, as this suggests that the model fits poorly to these patients. The  $R^2$  values are summarized

in Table 5.2 and the patients with the lowest  $R^2$  values are indeed the ones that had poor fits in Figures 5.6 and 5.6.

Patient	$R^2$	Patient	$R^2$
2	0.87	22	0.89
4	0.97	24	0.81
6	0.61	26	0.51
8	0.98	27	0.98
9	0.89	28	0.55
10	0.59	30	-3.47
11	0.98	32	0.97
12	0.98	33	0.82
15	0.69	34	0.96
16	0.85	35	0.72
17	0.74	36	-9.30
19	-0.33	37	0.93
21	0.80	39	0.95

Table 5.2: Table of  $R^2$  values. Patients with poor  $R^2$  values are highlighted in red.

In the poor fit cases shown in Figures 5.6 and 5.7, Patients 19 and 30 have data that does not behave like the ones in the good fit cases (Figures 5.2, 5.3, 5.4, 5.5). We see that for patients 19 and 30, the gross tumor volume peaks around 200 days, and then the gross tumor volume data decreases in the following data points. This behaviour in the data is only present for these two patients suggesting that there is a potential measurement error or that these patients received another treatment that was not documented. In the case of patient 36, the data is limited and the fit may improve if more data for that patient is provided.

Now that we have determined for which patients the model is able to fit the data, we remove the poor fits from our study. That is, we remove the cases with poor  $R^2$  values and focus on analyzing the rest. Hence, we focus on the remaining 23 patients.

We first analyze the parameter ranges by plotting the box plots of them which are seen in Figure 5.8. We see that for the growth rate,  $r$ , and the clearance rate,  $\gamma$ , the parameter ranges are fairly narrow whereas the parameter ranges for the initial volume  $V_0$  and carrying capacity  $K$  are wide due to the way we sampled these parameters.

Further, the chemotherapy kill rate  $\mu$  is fairly spread out through the chosen interval  $[0, 1]$  however the median of  $\mu$  is fairly low.

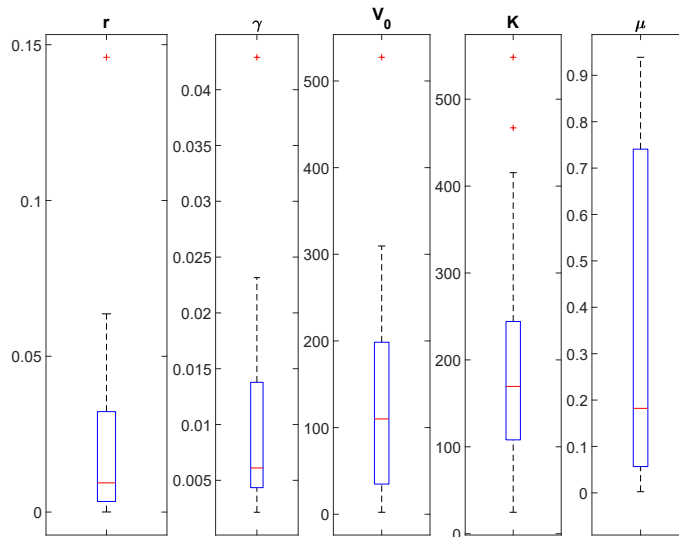


Figure 5.8: Box plots of the parameter ranges obtained from the data fits. Here  $r$  is the growth rate,  $\gamma$  is the clearance rate,  $V_0$  is the initial volume,  $K$  is the carrying capacity and  $\mu$  is the effectiveness of chemotherapy.

Using these parameters, we observed that a certain parameter ratio seems to indicate patient outcome

$$\rho = \frac{r}{\gamma\mu} = \frac{\text{growth rate}}{\text{death rate} \times \text{kill rate}}. \tag{5.18}$$

This ratio arises intuitively by noting that the lower the growth rate the slower the tumor grows. Further, the tumor dies more if the tumor death rate and the kill rate from treatment are high. Here, the kill rate from treatment is assessed by  $\mu$  (the kill rate from chemotherapy) since the kill rate from intensity-modulated radiotherapy treatments is fixed for all cases. Hence, we expect that the lower the  $\rho$  the better the outcome from treatment, and if  $\rho$  is high then the treatment is likely to fail, and tumor recurrence is expected. Indeed, this pattern is verified by computing the ratios from the fitted parameters which are summarized in Table 5.3.

In Table 5.3, the patients who do not respond well to treatment are highlighted

in blue which were determined from the fits based on how quickly the tumor regrew. Specifically, if the fitted curve shows tumor regrowth within the observed time period, then we say that the patients had a poor treatment response. We see a clear trend where the patients who do not respond well to treatment generally have a significantly higher  $\rho$  ratio in comparison to the patients who do respond to treatment. This suggests that focusing on lowering the tumor growth rate, and raising the clearance rate and improving treatment effectiveness will decrease  $\rho$  hence increasing the chances of successful treatment. We also find that 1 female patient out of 8 has a poor treatment response whereas 7 out of 15 males have a poor treatment response. So for this study, females tended to respond better to treatment.

Patient	Gender	$\rho$	Patient	Gender	$\rho$
2	f	5.53	22	m	18.29
4	f	9.48	24	m	4.65
6	m	7.44	26	f	46.27
8	f	9.13	27	m	373.1
9	m	55.89	28	m	72.87
10	f	3.96	32	m	20.19
11	m	7.42	33	m	11.46
12	f	11.31	34	m	71.66
15	m	9.74	35	m	5.67
16	m	0.67	37	f	8.26
17	m	0.01	39	f	15.32
21	m	2.11			

Table 5.3: Table of  $\rho$  ratios. Highlighted in blue are are patients who do not respond well to treatment. Here, m stands for male and f stands for female.

## 5.6 Conclusion

In this chapter, we derived a simple model called Model 1 (5.8) which was able to fit to 23 patient cases out of 26. The damaged volume compartment in Model 1 describes the gross tumor volume decrease post treatment well, showing that it is important to account for the damaged volume in order to accurately describe the long term tu-

mor volume dynamics. As Model 1 is fairly simple, it may be possible to determine the parameters clinically for each patient, which will be useful in tailoring the cancer treatment in order to attain the target tumor volume.

From the Latin Hypercube Sampling fitting method, we found that there is significant variation in parameter values between each patient. The variation in parameter values highlights that each patient is different with a unique response to treatment. Hence, it is difficult to assign a general set of parameter values that will pertain to each patient. Nevertheless, we found a pattern in parameter ranges, that could indicate patient outcome. In particular, the ratio  $\rho$  comprised from the tumor growth rate  $r$ , tumor clearance rate  $\gamma$ , and tumor cell kill rate by chemotherapy  $\mu$ , suggests that patients with a low  $r$  and high  $\gamma, \mu$  will respond to treatment better based on the data. Validating this ratio against more data is future work.

Our findings support some of the conclusions in Tariq et al. [64]. Like in [64], we find that accounting for the latency time effect through a damaged volume compartment explains the tumor volume dynamics well. This also means that a one dimensional ODE model proposed in [23] is insufficient to explain our gross tumor volume data. Further, we find that logistic tumor growth, is more accurate at modelling the long term dynamics of NSCLC unlike the exponential growth model that was argued for in [64]. This is because Tariq et al. [64] had only short term gross tumor volume data available, for which an exponential growth model was found to be sufficient.

As our model is able to explain the long term gross tumor volume dynamics well, it could be used to find an optimal treatment regimen. Based on the patient parameters obtained from LHS, we have modified the treatment schedule. We found that a treatment applying both radiotherapy and chemotherapy is superior to a treatment that applies only radiotherapy at delaying tumor regrowth. Further, we found that sequential radio-chemotherapy delays tumor regrowth more than concurrent chemo-radiotherapy. This is interesting as in the findings of Geng et al. [23], they found that concurrent chemo-radiotherapy improves survival time. Because of the limited data, we assumed that all patients have the same radiosensitivity parameters meaning that

all patients have the same radiation sensitivity. With more data, this parameter should also be ideally estimated for as well. Once the radiosensitivity parameters are fine tuned to each patient, the treatment regimen which delays tumor regrowth may change accordingly, and perhaps be in more favour of concurrent chemo-radiotherapy. Nevertheless, a combined treatment comprised of both chemotherapy and radiotherapy is still expected to outperform a treatment comprised of solely chemotherapy or radiotherapy.

We have compared Model 1 to a model accounting for the Allee effect (Model 2). We found that both models yield fairly similar fits to the available NSCLC data. The models were derived from full models incorporating CSC and TC dynamics, and the resulting models, Model 1 and 2, did not distinguish between the CSC and TC populations. Hence, the distinction between CSCs and TCs is not necessary to explain the gross tumor volume data. Further, we found that Model 1 fits the data better than Model 2, based on the AICc values. Therefore, an Allee effect is also not necessary to explain the gross tumor volume dynamics.

Proposing a model that explains the gross tumor volume data, is the first step in modelling NSCLC. Modern medical imaging can provide more information, such as the spatial resolution of the tumor area as well as the identification of physiological features such as organs, major bronchi, and blood vessels. Inclusion of such features is outside of the scope of this thesis. By including spatial components to Model 1, some of these features can be accounted for, which could help identify the ideal locations for treatment application in order to cause tumor remission.

# Chapter 6

## Discussion

Spontaneous tumor remission is poorly understood to this day, and it is still an open question as to how to make it occur more frequently [54, 39]. By accounting for various feedback mechanisms in our mathematical models for tumor growth, we showed that an Allee effect may be present. The presence of the Allee effect means that certain sizes of tumors are unable to establish themselves or grow in an environment, serving as a possible explanation as to why spontaneous tumor remission occurs [38, 39]. In Chapter 2, 3, and 4, we studied the Allee effect by building upon existing cancer stem cell models. In Chapter 2, we extended the Hillen et al. [31] model by modifying the feedback mechanism arising from spatial limitations. Specifically, this mechanism is a negative feedback mechanism, where due to limited space, cell proliferation decreases. We extended this feedback mechanism to also account for the cell fitness to reproduce in an environment. We found that the model proposed in Chapter 2 has its dynamics organized by a slow manifold, which is comprised of attracting and repelling branches separated by non hyperbolic points. The existence and position of the repelling branch dictates the shape of the Allee region, which captures the densities at which tumors experience spontaneous decay. Moreover, the size of the Allee region generally increases as the TC death rate and Allee threshold parameters increase. The existence of an Allee region shows that it is enough for a treatment to push the tumor density to a size

contained within the Allee region in order to attain tumor control. Hence, treatments do not need to fully eradicate the tumor.

In Chapter 3, we modify the negative feedback mechanism in the model proposed in Chapter 2, to ensure that the tumor densities within the Allee region do not become negative, so that all solutions are biologically realistic. The analysis from Chapter 2, carries over to the modified model with minimal changes. When we add treatment to the modified model, we also incorporate a damaged cell compartment. We saw that a cytotoxic treatment focused on killing both cell types, without a particular target, can increase the Allee region, but this increase is limited by predetermined parameters, which vary depending on the tumor. From a cytotoxic treatment, we saw that there are three possible outcomes. The first outcome is that if a tumor falls within the enlarged Allee region, then tumor control is attained. The second outcome is when the treatment fully eradicates the TCs, which corresponds to the treatment pushing the tumor to the Allee region. The last outcome is when the treatment fails to shrink the tumor to a size that is contained in the Allee region. In this case, if treatment stops the tumor regrows. Moreover, if the treatment is poor at killing CSCs, it may instead promote the tumor to select for CSCs. We generally find that the less CSCs the initial tumor has, the more likely the treatment can force tumor control. Therefore, a pure cytotoxic treatment may not be the best treatment for all tumors reiterating the conclusions found by Youssefpour et al. [70] and Bachman et al. [1], where it was found that a cytotoxic treatment alone, like radiotherapy, is unlikely to fully control the tumor.

In Chapter 4, we extended the work of Konstorum et al. [38] by incorporating feedback mechanisms into a base CSC model derived by using the self-renewal probability  $p$  and accounting for the CSC and TC dynamics. Specifically, we accounted for the positive and negative feedback mechanisms stimulated by the self-renewal and differentiation promoters onto CSC ability to self renew, as well as the negative feedback mechanism onto cell proliferation arising from spatial limitations. We showed that an Allee region still exists, and increases as the TC death rate and the amount of differentiation promoters increase. Falling in line with the results from Chapter 2, we find

that a cytotoxic treatment focused on solely targeting the TCs can increase the Allee region, but also promote the tumor to select for CSCs hence causing a tumor growth paradox. This means that if the treatment fails to control the tumor, the tumor regrows more aggressively post treatment, which was also observed in the tumor growth simulations post cytotoxic therapy by Youssefpour et al. [70]. Targeted therapy focused on increasing the amount of differentiation promoters, can increase the Allee region much more, without any drawback from the tumor growth paradox, meaning that if the treatment fails, there is no significant change in tumor aggressiveness, falling in line with what was observed in [70]. We find that targeted therapy combined with a cytotoxic treatment like radiotherapy, increase the Allee region significantly more than the respective treatments by themselves. Hence, a combined treatment has a greater chance at attaining tumor control which was also concluded by Youssefpour et al. [70] and Bachman et al. [1]. Targeted therapies are currently being tested, some of which are precisely designed to decrease the amount of self-renewal activators, for example suppressing the Wnt pathways [69]. These therapies have shown some promising results, and one of the current directions in cancer treatment is to find the best way to combine targeted therapy along with typical cytotoxic treatments [71]. We note that specific behaviours of the signaling pathways such as Wnt are cancer specific due to varying gene mutations between cancers and are also currently being researched [26]. Hence, when applying the models to a specific cancer, appropriate modifications to the feedback mechanisms in the mathematical models may be required.

We have accounted for different processes present in the tumors in the mathematical models in Chapters 2, 3, 4 but there are many more processes occurring in cancer outlined by the hallmarks [28, 29, 27]. For example, we accounted for the cancer tissue's ability to divide uncontrollably, death resistance, and replicative immortality by incorporating CSC dynamics. A natural extension would be to incorporate cancer's ability to evade immune response into the model. By incorporating a full immune cell response into our models, we can study if an Allee effect is still present and gain insight on how to make treatments which boost the immune response (immunotherapy) more

successful. Incorporating the immune response could be done by combining our models with the cancer model incorporating the immune response proposed by Kuznetsov et al. [42], which has been recently validated against cancer data [18]. Moreover, tumor growth dynamics also depend on the tumor microenvironment and nutrient uptake [28, 29, 27], which are processes we neglect for model simplicity. Another open question that remains is whether the slow manifolds we have seen in Chapters 2 and 3 forms a dynamical system in itself. As the slow manifolds are the organizing center for the dynamics of our models, understanding all properties of the slow manifolds is important. Other questions arise regarding the optimization of treatment. It is important to optimize treatment application time as well as the location of treatment, in order to improve the chances of tumor remission [72]. One specific question is how long should the treatment last, before it can be lifted and the tumor cannot regrow. For the models presented in Chapters 2, 3, and 4, this question is relevant, if the tumor does indeed fall within the increased Allee region formed from treatment. Like in [38], the answer we find is that the treatment should be applied until the total tumor density falls within the naturally occurring Allee region, but knowing the size of the original Allee region will depend on the parameters of a specific cancer, which may be difficult to estimate.

In Chapter 5, we proposed a simple model accounting for radiotherapy and chemotherapy treatments which is able to fit to the available NSCLC data well. We found that accounting for the Allee effect is not necessary to explain the data nor is the distinction between CSCs and TCs. However, the damaged cell compartment is necessary to incorporate in order to accurately model the tumor shrinkage seen post treatment in the data. This falls in line with findings by Tariq et al. [64], as they also concluded that a damaged cell compartment is necessary to explain NSCLC data. By fitting the model to each patient, we found that there is a fair spread in the resulting parameters. This is because patients have varying ages, weights, diets, etc., which showcases that a one fits all approach does not work. Nevertheless, we find a ratio that can indicate treatment outcome, which is comprised of the growth rate, clearance rate, as well how well the patient responds to chemotherapy. Moreover, it may be possible to determine

some of these parameters prior to the start of treatment. Modern imaging techniques can provide information about the structure and location of the tumor. By using this data and extending the simple model we proposed in Chapter 5 to account for spatial aspects, tumor shape and spread can be modelled. Through this, it may be possible to identify which regions in a tumor to target in order to cause tumor remission. This would be another approach to study the Allee effect, which inherently depends on which environments or locations the tumor has grown and spread to.

Here, we performed a systematic study of the Allee effect in cancer stem cell models with an application to NSCLC. We found that an Allee effect is present under different assumptions for feedback mechanisms, suggesting that it is an underlying phenomenon in cancer dynamics. The ODE models presented here are capturing the essential dynamics between cancer stem cells and cancer cells lacking stemness. By gaining an understanding of these essential dynamics through mathematics, we are one step closer to understanding tumor growth, cancer treatment responses, and spontaneous tumor remission.

# Bibliography

- [1] BACHMAN, J. W., AND HILLEN, T. Mathematical optimization of the combination of radiation and differentiation therapies for cancer. *Frontiers in oncology* 3 (2013), 52.
- [2] BAILEY, J. M., SINGH, P. K., AND HOLLINGSWORTH, M. A. Cancer metastasis facilitated by developmental pathways: Sonic hedgehog, notch, and bone morphogenic proteins. *Journal of cellular biochemistry* 102, 4 (2007), 829–839.
- [3] BILOUS, M., SERDJEBI, C., BOYER, A., TOMASINI, P., POUYPOUDAT, C., BARBOLOSI, D., BARLESI, F., CHOMY, F., AND BENZEKRY, S. Quantitative mathematical modeling of clinical brain metastasis dynamics in non-small cell lung cancer. *Scientific Reports* 9, 1 (2019), 13018.
- [4] BONNET, D., AND DICK, J. E. Human acute myeloid leukemia is organized as a hierarchy that originates from a primitive hematopoietic cell. *Nature medicine* 3, 7 (1997), 730–737.
- [5] BORSI, I., FASANO, A., PRIMICERIO, M., AND HILLEN, T. A non-local model for cancer stem cells and the tumour growth paradox. *Mathematical Medicine and Biology: A Journal of the IMA* 34, 1 (2017), 59–75.
- [6] CARBALLO, G. B., HONORATO, J. R., DE LOPES, G. P. F., AND SPOHR, T. C. L. D. S. E. A highlight on sonic hedgehog pathway. *Cell Communication and Signaling* 16 (2018), 1–15.

- [7] CHAN, C., LANG, S., ROWBOTTOM, C., GUCKENBERGER, M., FAIVRE-FINN, C., COMMITTEE, I. A. R. T., ET AL. Intensity-modulated radiotherapy for lung cancer: current status and future developments. *Journal of Thoracic Oncology* 9, 11 (2014), 1598–1608.
- [8] CHEN, Z., FILLMORE, C. M., HAMMERMAN, P. S., KIM, C. F., AND WONG, K.-K. Non-small-cell lung cancers: a heterogeneous set of diseases. *Nature Reviews Cancer* 14, 8 (2014), 535–546.
- [9] CHVETSOV, A. V., DONG, L., PALTA, J. R., AND AMDUR, R. J. Tumor-volume simulation during radiotherapy for head-and-neck cancer using a four-level cell population model. *International Journal of Radiation Oncology\* Biology\* Physics* 75, 2 (2009), 595–602.
- [10] CHVETSOV, A. V., PALTA, J. J., AND NAGATA, Y. Time-dependent cell disintegration kinetics in lung tumors after irradiation. *Physics in Medicine & Biology* 53, 9 (2008), 2413.
- [11] CLEVERS, H., LOH, K. M., AND NUSSE, R. An integral program for tissue renewal and regeneration: Wnt signaling and stem cell control. *science* 346, 6205 (2014), 1248012.
- [12] CORNELL, J., AND BERGER, R. Factors that influence the value of the coefficient of determination in simple linear and nonlinear regression models. *Phytopathology* 77, 1 (1987), 63–70.
- [13] COURCHAMP, F., BEREC, L., AND GASCOIGNE, J. *Allee effects in ecology and conservation*. OUP Oxford, 2008.
- [14] DAHAN, P., MARTINEZ GALA, J., DELMAS, C., MONFERRAN, S., MALRIC, L., ZENTKOWSKI, D., LUBRANO, V., TOULAS, C., COHEN-JONATHAN MOYAL, E., AND LEMARIE, A. Ionizing radiations sustain glioblastoma cell dedifferentiation

- to a stem-like phenotype through survivin: possible involvement in radioresistance. *Cell death & disease* 5, 11 (2014), e1543–e1543.
- [15] DE VRIES, G., HILLEN, T., LEWIS, M., MÜLLER, J., AND SCHÖNFISCH, B. *A course in mathematical biology: quantitative modeling with mathematical and computational methods*. SIAM, 2006.
- [16] DINGLI, D., AND MICHOR, F. Successful therapy must eradicate cancer stem cells. *Stem cells* 24, 12 (2006), 2603–2610.
- [17] DITTMAR, T., AND ZÄNKER, K. S. *Role of cancer stem cells in cancer biology and therapy*. CRC Press, 2013.
- [18] EL WAJEH, M., JUNG, F., BONGARTZ, D., KAPPATOU, C. D., GHAFARI LALEH, N., MITSOS, A., AND KATHER, J. N. Can the kuznetsov model replicate and predict cancer growth in humans? *Bulletin of Mathematical Biology* 84, 11 (2022), 130.
- [19] ENDERLING, H., ANDERSON, A. R., CHAPLAIN, M. A., BEHESHTI, A., HLATKY, L., AND HAHNFELDT, P. Paradoxical dependencies of tumor dormancy and progression on basic cell kineticstumor dormancy and progression. *Cancer research* 69, 22 (2009), 8814–8821.
- [20] FASANO, A., MANCINI, A., AND PRIMICERIO, M. Tumours with cancer stem cells: A pde model. *Mathematical biosciences* 272 (2016), 76–80.
- [21] GANGULY, R., AND PURI, I. Mathematical model for the cancer stem cell hypothesis. *Cell proliferation* 39, 1 (2006), 3–14.
- [22] GARDNER, S. N. A mechanistic, predictive model of dose-response curves for cell cycle phase-specific and-nonspecific drugs. *Cancer research* 60, 5 (2000), 1417–1425.

- [23] GENG, C., PAGANETTI, H., AND GRASSBERGER, C. Prediction of treatment response for combined chemo-and radiation therapy for non-small cell lung cancer patients using a bio-mathematical model. *Scientific reports* 7, 1 (2017), 1–12.
- [24] GERSON, S. L., CAIMI, P. F., WILLIAM, B. M., AND CREGER, R. J. Chapter 57 - pharmacology and molecular mechanisms of antineoplastic agents for hematologic malignancies. In *Hematology (Seventh Edition)*, R. Hoffman, E. J. Benz, L. E. Silberstein, H. E. Heslop, J. I. Weitz, J. Anastasi, M. E. Salama, and S. A. Abutalib, Eds., seventh edition ed. Elsevier, 2018, pp. 849–912.
- [25] GONG, J., DOS SANTOS, M. M., FINLAY, C., AND HILLEN, T. Are more complicated tumour control probability models better? *Mathematical medicine and biology: a journal of the IMA* 30, 1 (2013), 1–19.
- [26] GROENEWALD, W., LUND, A. H., AND GAY, D. M. The role of wnt pathway mutations in cancer development and an overview of therapeutic options. *Cells* 12, 7 (2023), 990.
- [27] HANAHAN, D. Hallmarks of cancer: new dimensions. *Cancer discovery* 12, 1 (2022), 31–46.
- [28] HANAHAN, D., AND WEINBERG, R. A. The hallmarks of cancer. *cell* 100, 1 (2000), 57–70.
- [29] HANAHAN, D., AND WEINBERG, R. A. Hallmarks of cancer: the next generation. *cell* 144, 5 (2011), 646–674.
- [30] HEK, G. Geometric singular perturbation theory in biological practice. *Journal of mathematical biology* 60, 3 (2010), 347–386.
- [31] HILLEN, T., ENDERLING, H., AND HAHNFELDT, P. The tumor growth paradox and immune system-mediated selection for cancer stem cells. *Bulletin of mathematical biology* 75, 1 (2013), 161–184.

- [32] HILLEN, T., AND SHYNTAR, A. Modelling of cancer stem cell driven solid tumors. In *Problems in Mathematical Biophysics - a volume in memory of Alberto Gandolfi* (2023), Springer, pp. 1–23.
- [33] HOFFMAN, R., BENZ, E. J., SILBERSTEIN, L. E., HESLOP, H. E., WEITZ, J. I., ANASTASI, J., SALAMA, M. E., AND ABUTALIB, S. *Hematology: basic principles and practice*. Elsevier Inc., 2017.
- [34] IMBS, D.-C., EL CHEIKH, R., BOYER, A., CICCOLINI, J., MASCAUX, C., LACARELLE, B., BARLESI, F., BARBOLOSI, D., AND BENZEKRY, S. Revisiting bevacizumab+ cytotoxics scheduling using mathematical modeling: proof of concept study in experimental non-small cell lung carcinoma. *CPT: Pharmacometrics & Systems Pharmacology* 7, 1 (2018), 42–50.
- [35] IWASA, T., OKAMOTO, I., SUZUKI, M., NAKAHARA, T., YAMANAKA, K., HATASHITA, E., YAMADA, Y., FUKUOKA, M., ONO, K., AND NAKAGAWA, K. Radiosensitizing effect of ym155, a novel small-molecule survivin suppressant, in non-small cell lung cancer cell lines. *Clinical Cancer Research* 14, 20 (2008), 6496–6504.
- [36] KATAYAMA, E. S., HUE, J. J., BAJOR, D. L., OCUIN, L. M., AMMORI, J. B., HARDACRE, J. M., AND WINTER, J. M. A comprehensive analysis of clinical trials in pancreatic cancer: what is coming down the pike? *Oncotarget* 11, 38 (2020), 3489.
- [37] KIM, J. J., AND TANNOCK, I. F. Repopulation of cancer cells during therapy: an important cause of treatment failure. *Nature Reviews Cancer* 5, 7 (2005), 516–525.
- [38] KONSTORUM, A., HILLEN, T., AND LOWENGRUB, J. Feedback regulation in a cancer stem cell model can cause an allee effect. *Bulletin of mathematical biology* 78, 4 (2016), 754–785.

- [39] KOROLEV, K. S., XAVIER, J. B., AND GORE, J. Turning ecology and evolution against cancer. *Nature Reviews Cancer* 14, 5 (2014), 371–380.
- [40] KOZŁOWSKA, E., SUWIŃSKI, R., GIGLOK, M., ŚWIERNIAK, A., AND KIMMEL, M. Mathematical model predicts response to chemotherapy in advanced non-resectable non-small cell lung cancer patients treated with platinum-based doublet. *PLoS Computational Biology* 16, 10 (2020), e1008234.
- [41] KRAUSOVA, M., AND KORINEK, V. Wnt signaling in adult intestinal stem cells and cancer. *Cellular signalling* 26, 3 (2014), 570–579.
- [42] KUZNETSOV, V. A., MAKALKIN, I. A., TAYLOR, M. A., AND PERELSON, A. S. Nonlinear dynamics of immunogenic tumors: Parameter estimation and global bifurcation analysis. *Bulletin of Mathematical Biology* 56, 2 (1994), 295 – 321.
- [43] LAPIDOT, T., SIRARD, C., VORMOOR, J., MURDOCH, B., HOANG, T., CACERES-CORTES, J., MINDEN, M., PATERSON, B., CALIGIURI, M. A., AND DICK, J. E. A cell initiating human acute myeloid leukaemia after transplantation into scid mice. *Nature* 367, 6464 (1994), 645–648.
- [44] MADDALENA, L. Analysis of an integro-differential system modeling tumor growth. *Applied Mathematics and Computation* 245 (2014), 152–157.
- [45] MARCINIAK-CZOCHRA, A., STIEHL, T., HO, A. D., JÄGER, W., AND WAGNER, W. Modeling of asymmetric cell division in hematopoietic stem cells—regulation of self-renewal is essential for efficient repopulation. *Stem cells and development* 18, 3 (2009), 377–386.
- [46] MCKAY, M. D., BECKMAN, R. J., AND CONOVER, W. J. A comparison of three methods for selecting values of input variables in the analysis of output from a computer code. *Technometrics* 21, 2 (1979), 239–245.

- [47] MEDEMA, J. P., AND VERMEULEN, L. Microenvironmental regulation of stem cells in intestinal homeostasis and cancer. *Nature* 474, 7351 (2011), 318–326.
- [48] MEHTA, M., SCRIMGER, R., MACKIE, R., PALIWAL, B., CHAPPELL, R., AND FOWLER, J. A new approach to dose escalation in non-small-cell lung cancer. *International Journal of Radiation Oncology\* Biology\* Physics* 49, 1 (2001), 23–33.
- [49] MENDES, F., ANTUNES, C., ABRANTES, A., GONÇALVES, A., NOBRE-GOIS, I., SARMENTO, A., BOTELHO, M., AND ROSA, M. Lung cancer: the immune system and radiation. *British Journal of Biomedical Science* 72, 2 (2015), 78–84.
- [50] MEULMEESTER, E., AND TEN DIJKE, P. The dynamic roles of  $\text{tgf-}\beta$  in cancer. *The Journal of pathology* 223, 2 (2011), 206–219.
- [51] O’ROURKE, N., I FIGULS, M. R., BERNADÓ, N. F., AND MACBETH, F. Concurrent chemoradiotherapy in non-small cell lung cancer. *Cochrane Database of Systematic Reviews*, 6 (2010).
- [52] OWENS, K., AND BOZIC, I. Modeling car t-cell therapy with patient preconditioning. *Bulletin of Mathematical Biology* 83, 5 (2021), 1–36.
- [53] PERKO, L. *Differential equations and dynamical systems*, vol. 7. Springer Science & Business Media, 2013.
- [54] RADHA, G., AND LOPUS, M. The spontaneous remission of cancer: Current insights and therapeutic significance. *Translational Oncology* 14, 9 (2021), 101166.
- [55] RADTKE, F., AND CLEVERS, H. Self-renewal and cancer of the gut: Two sides of a coin. *Science* 307, 5717 (2005), 1904 – 1909.
- [56] RHODES, A., AND HILLEN, T. Mathematical modeling of the role of survivin on dedifferentiation and radioresistance in cancer. *Bulletin of mathematical biology* 78, 6 (2016), 1162–1188.

- [57] ROCKNE, R., ROCKHILL, J., MRUGALA, M., SPENCE, A., KALET, I., HENDRICKSON, K., LAI, A., CLOUGHESY, T., ALVORD, E., AND SWANSON, K. Predicting the efficacy of radiotherapy in individual glioblastoma patients in vivo: a mathematical modeling approach. *Physics in Medicine & Biology* 55, 12 (2010), 3271.
- [58] RODRIGUEZ-BRENES, I. A., KOMAROVA, N. L., AND WODARZ, D. Evolutionary dynamics of feedback escape and the development of stem-cell-driven cancers. *Proceedings of the National Academy of Sciences* 108, 47 (2011), 18983–18988.
- [59] SCHABATH, M. B., AND COTE, M. L. Cancer progress and priorities: lung cancer. *Cancer epidemiology, biomarkers & prevention* 28, 10 (2019), 1563–1579.
- [60] SELL, S. Stem cell origin of cancer and differentiation therapy. *Critical reviews in oncology/hematology* 51, 1 (2004), 1–28.
- [61] SHARMA, R., AND SHARMA, S. *Physiology, Blood Volume*. StatPearls Publishing, Treasure Island (FL), 2018.
- [62] SHYNTAR, A., PATEL, A., RHODES, M., ENDERLING, H., AND HILLEN, T. The tumor invasion paradox in cancer stem cell-driven solid tumors. *Bulletin of Mathematical Biology* 84, 12 (2022), 139.
- [63] TAKAHASHI, K., AND YAMANAKA, S. Induction of pluripotent stem cells from mouse embryonic and adult fibroblast cultures by defined factors. *cell* 126, 4 (2006), 663–676.
- [64] TARIQ, I., HUMBERT-VIDAN, L., CHEN, T., SOUTH, C. P., EZHIL, V., KIRKBY, N. F., JENA, R., AND NISBET, A. Mathematical modelling of tumour volume dynamics in response to stereotactic ablative radiotherapy for non-small cell lung cancer. *Physics in Medicine & Biology* 60, 9 (2015), 3695.
- [65] TESCHL, G. *Ordinary differential equations and dynamical systems*, vol. 140. American Mathematical Soc., 2012.

- [66] THAM, L.-S., WANG, L., SOO, R. A., LEE, S.-C., LEE, H.-S., YONG, W.-P., GOH, B.-C., AND HOLFORD, N. H. A pharmacodynamic model for the time course of tumor shrinkage by gemcitabine+ carboplatin in non-small cell lung cancer patients. *Clinical Cancer Research* 14, 13 (2008), 4213–4218.
- [67] THEWS, O., AND RIEMANN, A. Tumor ph and metastasis: a malignant process beyond hypoxia. *Cancer and Metastasis Reviews* 38 (2019), 113–129.
- [68] WALTER, R. J., SONNENTAG, S. J., ORIAN-ROUSSEAU, V., AND MUNOZ-SAGREDO, L. Plasticity in colorectal cancer: Why cancer cells differentiate. *Cancers* 13, 4 (2021), 918.
- [69] YANG, L., SHI, P., ZHAO, G., XU, J., PENG, W., ZHANG, J., ZHANG, G., WANG, X., DONG, Z., CHEN, F., ET AL. Targeting cancer stem cell pathways for cancer therapy. *Signal transduction and targeted therapy* 5, 1 (2020), 8.
- [70] YOUSSEFPOUR, H., LI, X., LANDER, A., AND LOWENGRUB, J. Multispecies model of cell lineages and feedback control in solid tumors. *Journal of theoretical biology* 304 (2012), 39–59.
- [71] YUAN, M., HUANG, L.-L., CHEN, J.-H., WU, J., AND XU, Q. The emerging treatment landscape of targeted therapy in non-small-cell lung cancer. *Signal transduction and targeted therapy* 4, 1 (2019), 61.
- [72] ZHOU, H.-M., ZHANG, J.-G., ZHANG, X., AND LI, Q. Targeting cancer stem cells for reversing therapy resistance: Mechanism, signaling, and prospective agents. *Signal Transduction and Targeted Therapy* 6, 1 (2021), 62.